2016-01-01

# Modeling And Testing Of Functional Materials For Energy System Applications

Hasanul Karim
*University of Texas at El Paso*, hasanulkarim.utep@gmail.com

# MODELING AND TESTING OF FUNCTIONAL MATERIALS FOR ENERGY SYSTEM APPLICATIONS

HASANUL KARIM

Doctoral Program in Mechanical Engineering

APPROVED:

Yirong Lin, Ph.D., Chair

Raymond C. Rumpf, Ph.D., Co-Chair

Norman Love, Ph.D.

David Roberson, Ph.D.

Charles Ambler, Ph.D.
Dean of the Graduate School

# Dedication

To my parents, my brother, my wife and my son

# MODELING AND TESTING OF FUNCTIONAL MATERIALS FOR ENERGY SYSTEM APPLICATIONS

by

HASANUL KARIM, MS

DISSERTATION

Presented to the Faculty of the Graduate School of

The University of Texas at El Paso

in Partial Fulfillment

of the Requirements

for the Degree of

DOCTOR OF PHILOSOPHY

Department of Mechanical Engineering

THE UNIVERSITY OF TEXAS AT EL PASO

August 2016

## Acknowledgements

There are several people I am indebted for this achievement. First of all, I would like to thank my supervisor Dr. Yirong Lin for his support, patience and guidance on the projects and also on every important aspect of my life. I would like to thank Dr. Raymond Rumpf for all the help, support and guidance and insightful discussions and for being so patient the entire time. I cannot thank enough the students of emlab, especially Mr. Jose Avila and Mr. Carlos Rodriguez for their help and support on testing and simulations. I want to thank all the students from FEMS lab, especially Mr. Diego Delfin, Mr. Luis Chavez, Mr. Ricardo Martinez, Mr. Luis Delfin and Mr. Mohammad Arif Ishtiaque Shuvo, I could not have done without their amazing support. Finally, I would like to thank my family and especially my dear wife Naznin Jahan Afrose for always being there for me and for her unbelievable patience and inspiration.

## Abstract

Energy efficiency is one of the key concerns addressing the problem of global warming. Numerous research has been going on in order to improve the efficiency of energy conversion systems to reduce the polluted emission in the atmosphere. One of the approach is monitoring and maintaining the critical parameters of operation such as temperature to ensure the desired reactions, however, the harsh environment present in these systems makes the use of current temperature sensing solutions such very challenging to implement. Wireless temperature sensors are getting increasing attention as a potential solution, however, the need of energy storage devices such as battery, capacitors limit their range of operation significantly. In this dissertation a passive wireless sensor based on the concept of metamaterials is proposed. The sensor consists of an array of metal circular ring resonators embedded in a ceramic dielectric matrix. Ansys Ansoft HFSS was used to conduct a feasibility study and design the sensor. To avoid complicated manufacturing technique, commercially available Cu washers were used as the metal structure and it was embedded inside a matrix containing 70% Boron Nitride and 30% Barium Titanate. The sensor performance is investigated as a function of temperature up to 200 °C and the effect of misalignment in the test setup, change in humidity in the environment and compressive strain on the sensor performance was also investigated. Another approach of increasing the efficiency of the energy system is to reduce the waste energy by harvesting and implementing that waste energy into producing electricity and significant amount of research is being carried out on energy harvesting using piezoelectric and pyroelectric effect. The most widely investigated material for this purpose is PZT (Lead Zirconate Titanate), which contains Lead, which has detrimental effect on human health and environment. Also, the low curie point of PZT and other common piezoelectric and pyroelectric materials makes them unsuitable for operation at high temperature environments such as energy conversion systems. In this dissertation a new material $LiNbO_3$ is investigated as an alternative source of PZT for pyroelectric energy harvesting. It was demonstrated that a single wafer of $LiNbO_3$ can generate

437.72 $nW/cm^3$ of power and can charge a supercapacitor of 0.2F capacitance. A newly developed supercapacitor containing Porous carbon-$CeO_2$ (PC-CON) hybrid electrode was charged using the material and the performance was compared to a commercial supercapacitor of similar capacitance. The newly developed PC-CON supercapacitor displayed faster charging rate than the commercial supercapacitor. It was also found that the amount of energy harvested can be increased by connecting several $LiNbO_3$ wafers in parallel and also by choosing a diode that has low leakage current and faster switching capability.

# Table of Contents

# List of Tables

# List of Figures

# Chapter 1: Introduction

## 1.1 Motivation

Arguably, the single most critical scientific and technological challenge for humanity in this century is to properly shape the future of global energy [1-3]. There is an ever increasing awareness of the importance of functional materials for energy systems in sensing [4, 5], energy harvesting [6, 7] and storage [8-13]. With Fossil fuels still dominating the world energy sector, it is of utmost importance to make the energy systems more efficient in order to reduce the emissions of $CO_2$ and other pollutant gases. Precise temperature sensing is one of the most critical parameters to safeguard better combustion, achieve higher efficiency and lower contaminant emissions to the environment. However, the energy conversion systems such as power plants [14], combustion engines [15], oil/gas extraction [16] and refineries [17] contains either high temperature or corrosive environments or a combination of both and hence, it is imperative that the sensors are made to survive this environment and at the same time is reliable. Wireless sensors [18] are considered to be the ideal solution for these systems as wired sensing is limited by complicated installation, difficult and costly maintenance, and susceptibility to corrosive atmosphere. However, the current generation of wireless sensors is mostly limited by the use of electronic components and energy storage devices such as batteries or capacitors, which cannot endure high temperatures or harsh environments. The desire for wireless temperature sensors for high temperatures has augmented numerous investigations using different technologies such as Optical sensors including remote pyrometers [19], fluorescence thermometers [20], fiber bragg gratings [21] and SAW sensors [22]. However, they are still limited by low temperature capability of optical fibers [23], cross-sensitivity issue of fiber bragg gratings, or by the variation of material properties in harsh environments that affect the response in SAW sensors [23].

The concept of wireless sensor networks (WSN) is getting increased attention [24-26] as it allows monitoring a larger area more conveniently and accurately. However, as the individual

wireless sensor nodes in the network require active power such as batteries and capacitors to energize them, the life is limited by the life of the energy storage devices. This complicates the maintenance of the sensor network and causes interruptions in the operation. Energy harvesting from the environment near the sensors are considered to be a probable solution to this problem and a myriad of investigations has been carried out in developing energy harvesting materials and systems [27-29]. The most widely investigate materials for mechanical and thermal energy harvesting are piezoelectric and pyroelectric materials respectively. Lead Zirconate Titanate (PZT) is the most investigated material to date owing to its excellent piezoelectric and pyroelectric properties compared to other materials in this class. However, Lead has detrimental effects on the environment and health. Also, PZT and other alternatives of PZT such as PVDF, PVDF-TrFE suffers from the very low curie temperature (below 500 °C) [30, 31] limitation beyond which the material loses its piezoelectric and pyroelectric properties. $LiTaO_3$ and ZnO have been investigated as potential high temperature pyroelectric materials since they have a higher curie temperature of 600 °C and 1400 °C respectively. However, the pyroelectric coefficient of ZnO is significantly low, which makes it difficult to generate sufficient energy [32]. There are energy systems that often operate at near or above 1000 °C. The materials investigated so far cannot be used to power up the wireless sensors or energy storage devices used in these systems. Hence, it is important to investigate for new materials with higher curie temperature.

This dissertation will address these two very significant problems of the energy systems. The first approach will be to develop a passive, wireless temperature sensor that is capable of enduring high temperatures and harsh environments. The sensor concept is inspired from the concept of metamaterials. The sensor will have a repeated pattern of Closed Ring Resonator (CRR) embedded inside a high temperature ceramic material. The ceramic material is robust in harsh environments and will protect the metal embedded inside it. The composite structure has a temperature dependent resonance frequency in the microwave frequency range owing to the dielectric property of the ceramic material. The second approach is to investigate a new lead free

material for pyroelectric energy harvesting. The proposed material is $LiNbO_3$ which has a very high curie temperature (1142 °C) [33]. The pyroelectric current generation capacity of the LNB will be investigated and the ability to do energy harvesting will be demonstrated by charging a supercapacitor.

## 1.2 Metamaterial based passive wireless temperature sensor

### 1.2.1 Introduction

Meta is a Greek word, which means "beyond", hence the word "metamaterials" used to refer to materials that can display properties that are beyond the properties of natural materials. However, metamaterial has obtained a much broad definition since its introduction. They are generally denoted as engineered periodic composite structures that are designed to obtain specific electromagnetic properties. This broad definition of metamaterials can cover many different branches of engineered material such as double negative (DNG) materials, negative refractive index (NIR) materials, Electromagnetic band gap (EBG) structured materials, and complex surfaces such as high-impedance ground planes [21] .

Metamaterials can be classified into two categories from the unit cell point of view; the first category corresponds to the metamaterials whose unit cells are much smaller than the guided wavelength and to the incident electromagnetic waves they appear as a homogeneous media. The electromagnetic properties of these materials are essentially obtained from a homogenization procedure, and they display effective electromagnetic property. As a result they are called the effective media [34] . The other category metamaterials have period in the order of the guided wavelength, including the structures known as electromagnetic bandgaps (EBGs). The effective media theory is not applicable for these metamaterials as the electromagnetic properties are characterized by their periodic nature instead [35]. The interference effects between scattered fields from the unit cells contributes to the electromagnetic properties and generally it gives rise to a band stop or band pass effect. The key application of these metamaterials is in planar circuits owing to their small electrical size compared to the working wavelength. As a consequence,

typical metamaterial unit cell components such as Split Ring Resonators (SRRs) [36], Complementary Split Ring Resonators (CSRRs) [37], and CRRs (Closed Ring Resonators)[38] have created new windows of application in miniaturization of planar microwave structures and circuits such as filters [37, 39], couplers [40], and antennas [41], or to improve the performance of these components [42]. In addition, the subwavelength dimensions, the ability to tune the response by modifying the unit cell dimensions and the high quality factor resonance has also made them ideal structures for applications as sensors [43, 44] or for improving the sensitivity of conventional sensors [45-47].

### 1.2.2 Theory

Meta is a Greek word, which means "beyond", hence the word "metamaterials" refers to materials that can display properties that are beyond the properties of natural materials. Usually the structure of these materials plays a significant role deciding its properties rather than the material properties of its components. When an electromagnetic wave passes through a material, the otherwise nonhomogeneous medium can be considered as a homogeneous medium if the atoms of that material are very small compared to the wavelength of the incident electromagnetic wave. So, from the electromagnetic point of view, it is the wavelength $\lambda$ that determines whether a collection of objects can be considered as a material or not. The block of objects might not be considered as a material by the conventional definition of materials but to the incident electromagnetic wave there is no difference and hence this can be considered as an artificial material or metamaterial [48]. Such homogeneous medium can be characterized by only two parameters: electric permittivity ($\varepsilon$) and magnetic permeability ($\mu$). These two parameters are very important and determine the propagation characteristic of an electromagnetic wave through a medium, which can be shown by the dispersion equation. The dispersion relation for an isotropic medium is defined as:

$$k^2 - \frac{\omega^2}{c^2} n^2 = 0 \tag{1.1}$$

Where, $k$ is the wavenumber, $\omega$ is the angular frequency, $c$ is the velocity of light in vacuum and $n$ is the refractive index of the substance, which is given by,

$$n = \sqrt{\mu_r \epsilon_r} \tag{1.2}$$

Where, $\mu_r$ is the relative permeability and $\varepsilon_r$ is the relative permittivity of the medium. For most of the natural materials both relative permeability and permittivity are positive and hence $n$ is also a positive number. As long as both $\mu_r$ and $\varepsilon_r$ have the same sign, $n$ is a real number and wave will propagate through the medium but, if one of them is negative then $n$ becomes imaginary and there will be no transmission for a thick substance. Now, the significance of both negative $\varepsilon_r$ and $\mu_r$ can be further investigated by examining Faraday's and Ampere's law. For a monochromatic plane wave that uses $e^{j\omega t}$convention, Ampere's and Faraday's law are expressed in equation 1.3 and 1.4 respectively:

$$\vec{k} \times \vec{H} = -\omega\varepsilon\vec{E} \tag{1.3}$$

$$\vec{k} \times \vec{E} = \omega\mu\vec{H} \tag{1.4}$$

Where, $\vec{k}$ is the wave vector, $\vec{H}$ and $\vec{E}$ are magnetic and electric field intensity vectors respectively. When both $\varepsilon$ and $\mu$ are positive, from equation (1.3) and (1.4) it can be seen that $\vec{k}$, $\vec{H}$ and $\vec{E}$ form a right-handed co-ordinate system whereas when they are both negative, the vectors form a left-handed co-ordinate system. A comparison between left-handed and right-handed co-ordinates systems is shown in Figure 1.1. Veselago's proposal of an artificial medium that can have simultaneously negative values of permittivity ($\varepsilon$) and permeability ($\mu$) in 1968 was actually the starting point of the research on left-handed metamaterials [49].

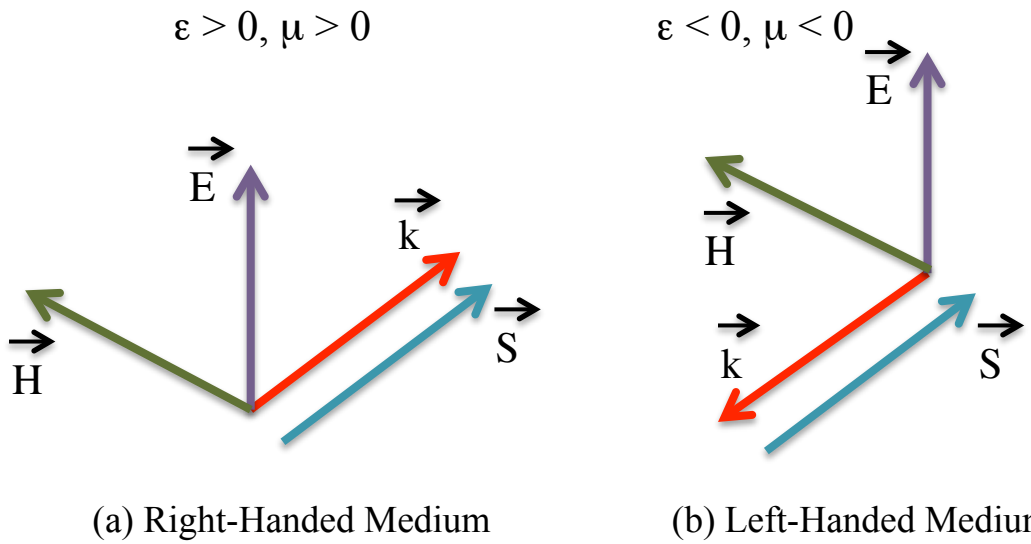


(a) Right-Handed Medium (b) Left-Handed Medium

Figure 1.1: Directions of the Electric (E) and Magnetic (H) vector fields, wave vector (k) and the power flow density (S) vector in (a) Right Handed Medium and (b) Left Handed Medium

It was expected that a left-handed medium would display some nonconventional behaviors such as backward propagation, reverse Doppler effect, reverse Vavilov-Cerenkov effect, and negative index of refraction [50]. The phenomenon of negative index of refraction can be explained with a modified Snell's law. When a ray of light passes from one medium to another medium the refraction of the light follows the general Snell's law (equation 1.5) if both media are right handed. As shown in Figure 1.2, the incident light ray is reflected along path 2 and refracted through path 3. However, if one of the media is left handed then a more accurate form of the Snell's law is used (equation 1.6). In that case, the refracted light goes along path 4.

$$\frac{\sin\theta}{\sin\phi} = \frac{n_2}{n_1} = \sqrt{\frac{\mu_2\varepsilon_2}{\mu_1\varepsilon_1}} \tag{1.5}$$

$$\frac{\sin\theta}{\sin\phi} = \frac{n_2}{n_1} = \frac{p_2}{p_1}\left|\sqrt{\frac{\mu_2\varepsilon_2}{\mu_1\varepsilon_1}}\right| \tag{1.6}$$

Where $p_1$ and $p_2$ are the rightness of the first and second medium respectively. p is +1 for a right handed medium and it is -1 for a left handed medium.

Negative values of permeability and permittivity can be obtained by combining special resonator structures with appropriate excitation techniques. There are three types of excitations

that can be used for metamaterial resonator structures. They are: magnetic excitation, electric excitation and both magnetic and electrical excitation [50-52]. The choice of the excitation depends on the desired application. If ENG regions are required, the structure has to be excited electrically and it has to be excited

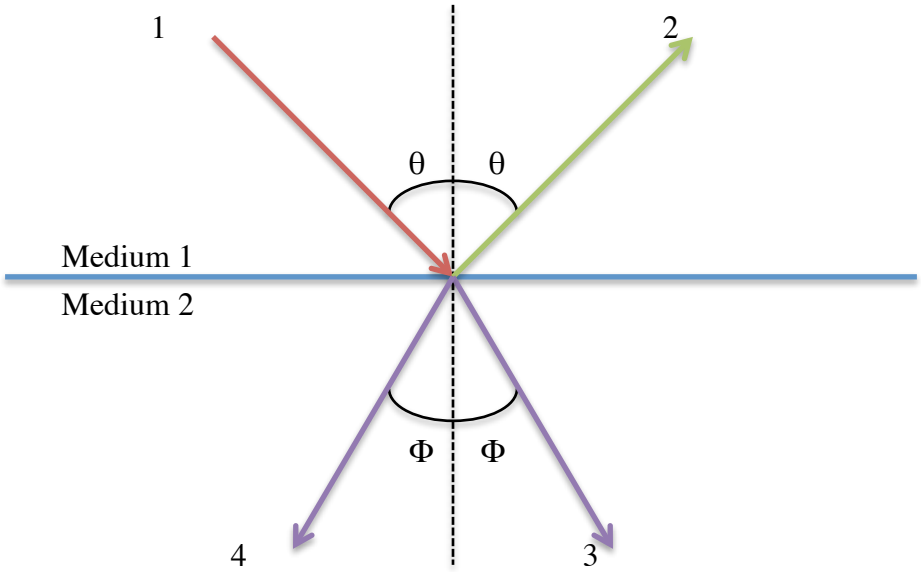


Figure 1.2: Light ray passing from medium 1 to medium 2. 1) incident ray, 2) Reflected ray, 3) refracted ray in a right handed medium and 4) refracted ray in a left handed medium

magnetically in order to obtain MNG regions [52]. Figure 1.3 summarizes the excitation techniques for a SRR structure. In figures 1.3(a) and 1.3(b), the magnetic field is perpendicular to the SRR plane. Hence, according to the Faraday's law of induction it can excite the magnetic resonances of the SRR. On the other hand, when the magnetic field is parallel to the SRR plane it cannot excite a magnetic resonance. In figures 1.3(b) and 1.3(c), the electric field is perpendicular to the gap of the rings. This configuration can excite the electrical resonances of the structure. Hence, the structure in figure 1.3(b) is excited both electrically and magnetically and the structure at 1.3(d) is not excited at all from the sense of an LC circuit.

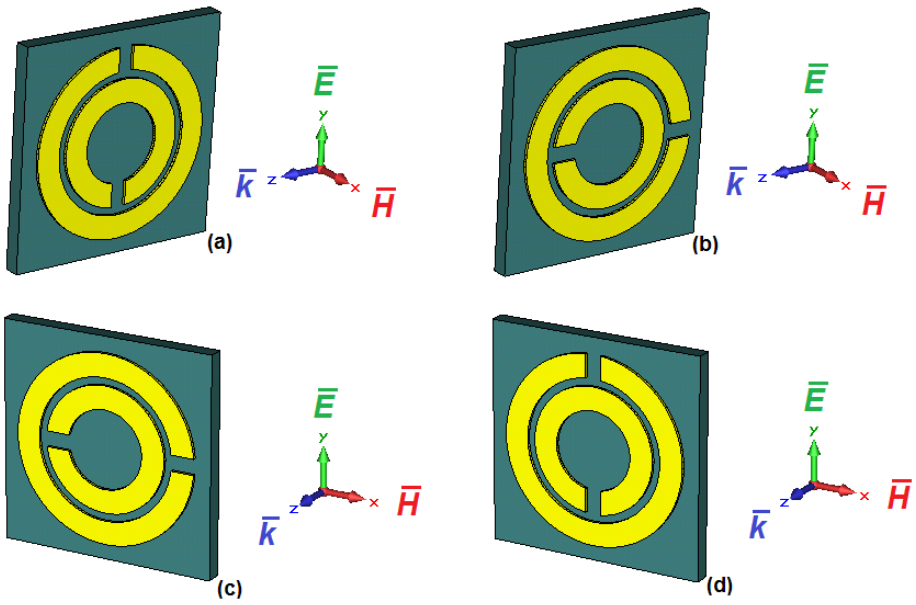


Figure 1.3: Different excitation techniques for SRR structure (a) only magnetic excitation (b) electric and magnetic excitation (c) only electric excitation and (d) no excitation. [53]

Prior to the development of metamaterials, materials with single negative index were found in nature, which were either Epsilon Negative media (ENG) or Mu Negative media (MNG). The concept of a Double Negative media (DNG) or Left Handed Media (LHM) was exciting, but it was not realized in reality until in 1999 when J.B. Pendry et al. [54] proposed the use of periodical arrays of SRRs (Split Ring Resonators) and thin-wires together where the negative values of effective permeability are obtained from the SRR structure and the negative values of permittivity are obtained from the thin wire array. It has been demonstrated that metamaterials need to appear as an effectively homogeneous media, which means that their lattice constants have to be smaller than the wavelength of the incident radiation [55].

Although SRR is not the only structure suggested in literature for obtaining the negative permeability value, it is the most studied structure so far. A single unit of SRR consists of two concentric thin sheets with splits on opposite sides. When excited, most of the electromagnetic energy is stored in the tiny gap between the rings, which results in an immense increase of the energy density. Figure 1.4 shows the SRR structure proposed by Pendry et al. Since then,

metamaterials have become a mainstream research area and a numerous amount of publications has been observed over the past decade. Different structures based on the original SRR structure were proposed and evaluated for different applications. Some SRR structures studied in literature are shown in Figure1.5.

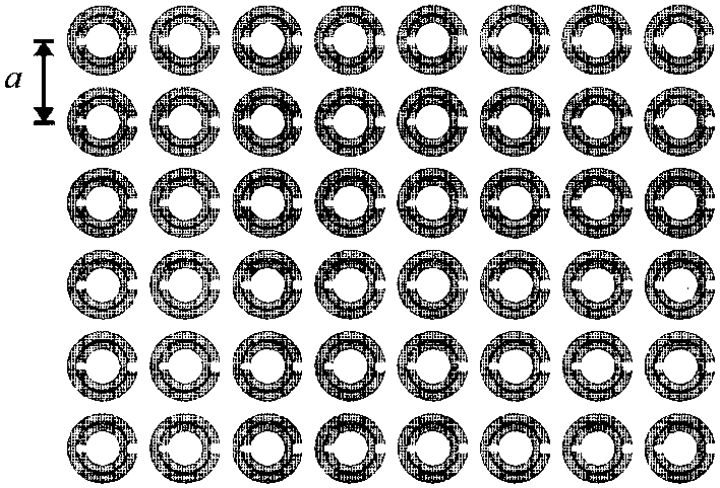


Figure 1.4: A square array of the first SRR structure proposed by Pendry et al. with lattice spacing *a* [54].

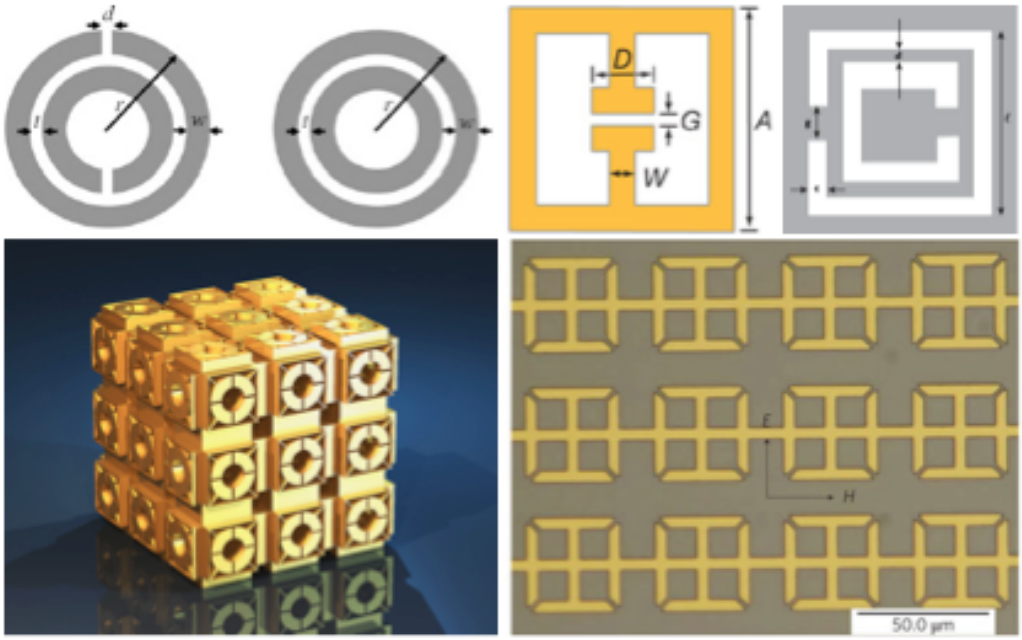


Figure 1.5: Some SRR structures studied in literature [56-59]

Another significant characteristic of the SRR structure is that it shows a resonant behavior. The structure can be represented as an LC circuit and the resonance frequency can be obtained by the following equation:

$$f_0 = {}^{1}/_{2\pi\sqrt{LC}} \tag{1.7}$$

Where, $f_0$ is the resonance frequency, L is the inductance and C is the capacitance of the SRR structure. Several approaches were made to analyze different types of SRR structures and to develop mathematical models and equivalent circuits for them, which will be discussed in greater details in the literature review section.

### 1.2.3 Application of Metamaterials

Metamaterials have shown a promising future in different fields such as optics and photonics due to their extraordinary properties. Their unique interaction with electromagnetic waves has focused research efforts on developing metamaterial-based applications that couldn't be achieved with regular materials, such as perfect lenses, sensing technologies, cloaking devices and antennas [60]. In order to achieve the aforementioned applications, different types of metamaterials have been developed including split ring resonators (SRRs), Swiss rolls, conical Swiss rolls and metal plasmons [60].

In Magnetic Resonance Imaging (MRI) obtaining magnetism without using any inherently magnetic materials is of great interest since natural magnetic materials will disturb the quasi-static magnetic field pattern of the system. Magnetic metamaterials that respond only to the time-varying magnetic fields can be used in this type of systems without interfering the field [48]. For example, Freire et al. studied a metamaterial lens for MRI, which improved its coil sensitivity and spatial localization [61].

In the optics area, Pendry proposed a perfect lens based on a negative refractive index material to overcome the limitations of current optical lens solutions [62]. This novel approach was focused on surpassing wavelength limitations imposed by classic alternatives and achieving subwavelength precision. Manipulation of light through metamaterials has also opened the

possibility for the development of cloaking devices. Partial cloaking can be achieved by absorbing or scattering incident light away from the detectors [63]. In this field, Shurig et al. studied the possibility of electromagnetic

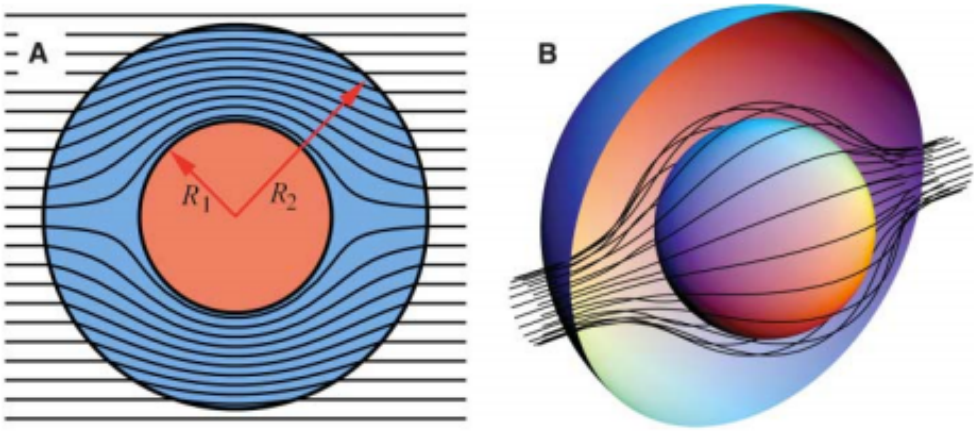


Figure 1.6: (A) 2D and (B) 3D paths that a light will follow theoretically through a cloaking device. [64]

cloaking in the microwave frequency through the fabrication of radial split ring resonators [65]. Their findings support the possibility of achieving cloaking mechanism through the transformation optics method and metamaterial structures. Moreover, researchers have also studied acoustic cloaking. Chen et al. developed a method for 3D mapping of acoustic cloaking supposing the existence of acoustic metamaterials, which can be achieved through local resonances [66].

Aside of these metamaterial applications, there exist others that could make materials behave like liquids under certain frequency ranges or hide entire buildings from earthquakes. Such metamaterials are called elastic (or mechanical) and seismic metamaterials, respectively. Elastic metamaterials have the ability of transfer only pressure waves at high frequencies; while at low frequencies they transmit pressure waves and shear waves (incompressible solid behavior) in specific directions [67]. Lai et al. studied the use of silicon rubber and steel rods to build a two-dimensional elastic metamaterial to achieve better control of the elastic waves in solid materials [67]. On the seismic front, Torres-Silva et al. analyzed the use of acoustic

metamaterials in the form of Swiss rolls to reduce the amplitude of seismic waves [68]. This structure can be placed around the building to act as an earthquake barrier, cloaking the building from the most destructive earthquake waves.

### 1.2.4 Metamaterials in sensing technology

Sensor development has also been benefited from the continuous advancement in metamaterials. Different designs have been proposed under the working mechanism of metamaterials for temperature, pressure, humidity and bio sensing. Biosensors are of extreme importance in disease diagnostics, food safety, environmental monitoring and in investigating other biological phenomena. Biosensors based on metamaterials have gained substantial attention because of their cost-effectiveness and label-free biomolecule detection from microwave to optical frequency [69]. Lee et al. [70] studied the use of split ring resonators to detect the binding of biotin and streptavidin, which is one of the most common non-covalent interactions found in nature, at microwave frequencies. A terahertz paper based biochemical sensor was proposed by Tao et al. [71] where the paper acts as a dielectric and a support while the SRR patterns defines the shift of the resonance as a result of the shift in the capacitance induced by the added material. A schematic and a fabricated sensor are displayed in figure 1.7. A metamaterial-based plasmonic biosensor was developed by Kabashin et al. utilizing an array of vertically aligned gold nanorods on a glass substrate, which improved the sensitivity by more than two orders of magnitude compared to the previously developed plasmonic biosensors [72]. The terahertz region has also been

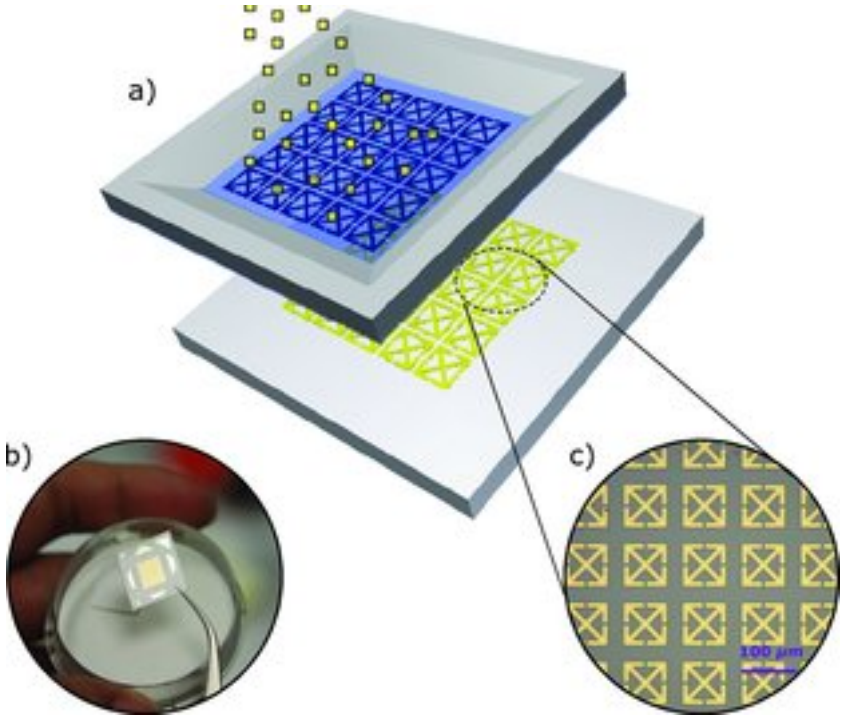


Figure 1.7: (a) Schematic of the micrometer-sized metamaterial resonators sprayed on paper substrates with a predefined microstencil (b) Fabricated sample (c) Optical microscopy image of an as fabricated paper metamaterial sample

explored to identify chemical and biochemical compound composition [69]. This can be achieved by sensing the resonant absorption of molecular or phonon resonances for small compounds. Yoshida et al. [73] proposed a novel, label-free sensing method in the terahertz frequency region by using a metallic mesh with thin profile to detect proteins.

Compared to Biosensors, not many studies have been reported on other types of sensors. Melik et al. [74] demonstrated a wireless strain sensor based on flexible metamaterial structure combining SRR structure and kapton tape. Ekmekci et al. proposed a metamaterial-based sensor for pressure, concentration, temperature and humidity sensor based on broadside-coupled split ring resonator (BC-SRR) [75]. Additionally, this research group also studied the feasibility of a V-shaped split ring resonator for pressure sensing applications.

### 1.2.5 Literature review

The following section will discuss the significant literatures that have pioneered the research in metamaterials and in wireless temperature sensing. The first half of the literature review will cover the development of metamaterials. An effort will be made to provide a brief history of the birth and growth of this extraordinary research area, which has made things possible that once were considered as impossible. Over a really short span of time this field has seen many revolutionary findings and has spread in a lot of areas. While every effort was made to cover all the significant pioneering literatures and important current findings, the overwhelming amount of research that is being done on this field has made it beyond the scope of this thesis to produce a complete report. The second half focuses on the recent development of the wireless temperature sensing system, which include both conventional approach and metamaterial-based approach.

#### *1.2.5.1 Metamaterials*

Although the surge of research in the area of metamaterials has started in the last decade, the idea of having artificial materials comprised of customized functional building blocks packed into an effective medium can be traced back to 1898 [76, 77], when Jagadish Chunder Bose conducted the first microwave experiment on twisted dielectric composites [78] which by today's definition was an artificial chiral medium [77] and it lead to artificial linear and circular birefringence. In 1920, Karl Lindman [76, 79] experimented with hand made copper helices individually wrapped into cotton balls and densely packed into an isotropic three dimensional chiral metamaterial which displayed enormous resonant optical activity at microwave frequency. W. E. Kock [77, 80] arranged conducting spheres, disks, and strips periodically to make microwave lenses and demonstrated that it is possible to tailor the effective refractive index of an artificial media.

The starting point of the research in metamaterials however, is considered to be the work of Viktor Veselago who first postulated that a material that has both the electric permittivity and

magnetic permeability, it will have a negative refractive index. This paper was published in 1967 [81] first in Russian and one year later in English. In addition to the negative refractive index or backward wave propagation he also hypothesized a flat lens, which was a possibility that was not considered ever before. But, despite these outstanding hypotheses the paper did not accelerate the research work in this area. After a long time in 1996, J.B. Pendry [82] proposed a grid of conducting wires that generates an effective frequency dispersive permittivity, obeys a Drude model and achieves negative values in the GHz frequency range. A few years later in 1999, he suggested another periodic structure in a form of SRR to achieve a frequency dispersive permeability obeying Lorentz dispersion [54]. It was also shown that by adjusting the parameters properly, the resonant frequency of the SRR could be brought down in the GHz range, resulting a negative value of permittivity in a frequency region that overlaps with the frequency region of negative permittivity. The following year, Smith et al. [83] made a composite medium combining an array of thin wires and SRR structures and demonstrated that indeed in the GHz range, it was possible to achieve simultaneous negative values of permittivity and permeability. So, it was proven that it was possible to make a composite medium to realize negative refraction, and shortly after, Shelby et al. [84] presented the first experimental realization of an LHM and confirmed the negative refractive index of the medium. Although this design undoubtedly produced negative refractive index, there were some drawbacks as well; the most important ones were low transmission level and a narrow band of left-handed properties [85]. Soon structures of novel geometries of SRR were proposed, including the axially symmetric SRR [86, 87], the broadside coupled SRR [88], the omega SRR [89, 90], the brickwall [91], the S-ring SRR [92] and some three dimensional designs [93-95] to rectify these two problems. The anisotropic nature of the SRR structures was another problem because it limits the excitation criteria of the structure [96]. Consequently, many researchers focused on preparing an isotropic structure that will display a negative refractive index irrespective of the propagation vector and orientation of the symmetry axes of the structure. For example, Vendik et al. [97] suggested an artificial structure, which had the arrangement of particles similar to the NaCl structure with cubic

symmetry. They proposed the use of two high permittivity sub-lattices embedded in a low permittivity matrix and the permittivity and permeability tensors of the structure were isotropic.

#### *1.2.5.2 Numerical simulations in designing and optimizing metamaterials*

The design and optimization of different geometries of SRRs depended on largely two approaches [85]: either an equivalent circuit approach [92] or full-wave numerical simulations [98]. The numerical simulation of SRRs verified the experimental results and offered the possibility of analyzing an effective media consisting of discrete elements to validate different properties. Right after the first experimental verification of negative refraction, an Finite Difference Time-Domain (FDTD) method based simulations of similar rings and rod structure provided the first verification of negative refraction by numerical simulations and it also clearly demonstrated the phenomenon of backward phase inside the structure [99]. Later, simulation works focused on analyzing the key properties of LHM [87] and afterwards, the emphasis was on developing efficient numerical algorithms for simulating large or three-dimensional geometries [94]. The use of full wave electromagnetic solver like Ansys Ansoft HFSS (High Frequency Structural Solver) has become more common where reflection and transmission characteristics could be simulated as a function of frequency [52] and the effective parameters could be calculated from the frequency responses of the S-parameters.

#### *1.2.5.3 Chiral Metamaterials*

If the particles of a medium cannot be superimposed on their mirror images then it's called a chiral medium [100]. Due to the intrinsic chiral asymmetry, the medium responds to the left circularly polarized (LCP) wave and right circularly polarized (RCP) wave differently [101]. There is also a cross coupling between the electric field and magnetic field going through a chiral medium which is described by a dimensionless chirality parameter $k$. Although researches on chiral materials have started long before [102], Tretyakov et al. [103] were first to discuss the possibility of realizing negative refraction in chiral nihility in 2003. The authors proposed the idea of fabricating a metamaterial composed of helical wires as a chiral media. One year later,

Pendry [104] analyzed the conditions to make negative refraction in chiral metamaterials possible and showed that it is in fact simpler than for regular metamaterials, since, a chiral medium does not need either $\varepsilon$ or $\mu$ to be negative to achieve a negative refractive index as long as the chiral parameter $k$ is large enough. Pendry then proposed a practical model with twisted Swiss rolls as elemental structures to obtain a chiral metamaterial working in the microwave regime. After that, the research on chiral metamaterials mainly branched into two directions: bulk chiral metamaterials and planar chiral thin films [101]. So far, most of the researches on bulk chiral metamaterials are theoretical due to the complexity in fabricating homogeneous 3D chiral structures. Significant studies on this topic include a quasi-planar chiral structure based on SRR [105], bulk isotropic magnetic metamaterials [106], and development of 3D isotropic chiral metamaterials [107]. Fabrication of complicated 3D chiral metamaterials using advanced manufacturing such as colloidal nanohole lithography has been reported recently [108-110]. Since planar structures are easier to fabricate than the bulk media, research by many groups has been reported on this topic and many interesting properties and potential applications has been addressed. Zheludev et al. were the first to report the optical activity of a planar chiral structure in the optical regime [111]. Later, a bi-layer rosette-shaped structure in the microwave regime was also reported by the same group, which displayed a very strong rotation in terms of rotary power per wavelength [112]. A planar chiral metamaterial made of duel strips connected by a tilted bridge was reported to have a negative refractive index in the terahertz frequencies [113]. Recently, planar chiral metamaterials has been developed for biosensing applications [114] and asymmetric transmission has been explored [115].

#### *1.2.5.4 Applications and prospects*

The first application for a metamaterial with a negative refractive index was proposed by Pendry [62], which was the exciting declaration of a possible perfect lens or 'superlens'. Another sensational application proposed by Pendry et al. [64] and later experimentally demonstrated by Schurig et al. [65] was cloaking of objects at microwave frequencies where the authors hid a

copper cylinder inside artificially structured metamaterial cloak. Other applications of LHM were in communication and miniaturization, which include obtaining new radiation patterns [116-118] and cavity resonant modes [85, 119]. Notable studies have been done in obtaining a reduced radar cross-section by analyzing the scattering of mainly canonical objects such as spheres or cylinders [120, 121], which was also extended to other random geometries [64]. The concept of cloaking soon crossed the boundary of only electromagnetic waves and was also applied in other applications. Yang et al. [122] demonstrated a dc electric cloak, which can make objects invisible to the applied static current fields. Theoretical discussion for both static [123, 124] and dynamic cloaking was found in literature. While the idea of static thermal coating was strictly equivalent to the static electric cloaking mentioned above [76, 125], dynamic thermal cloaking was more complicated [126]. Recently, Schittny et al. [127] designed, fabricated and characterized a micro structured transient thermal cloak that molds the flow of heat around an object in a metal plate, the fabricated cloak is shown in Figure 1.8. Other works of metamaterials beyond electromagnetism include acoustic metamaterials [128, 129], elastodynamic metamaterials [130], ultra-light metamaterials [131], 3D auxetic metamaterials [132] etc.

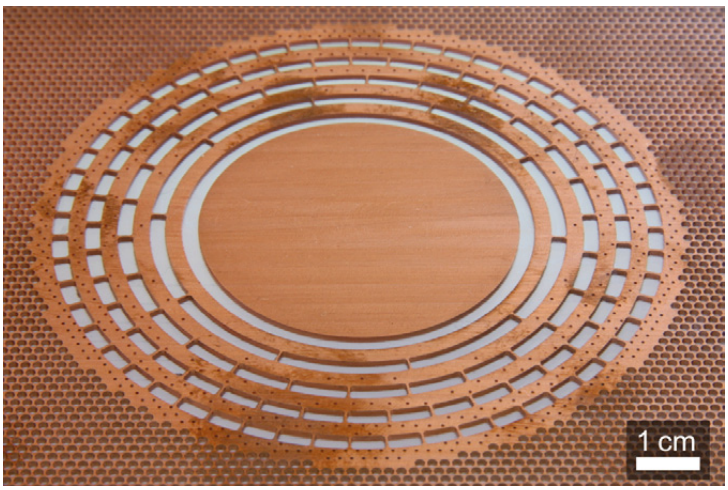


Figure 1.8: Photograph of an as built thermal cloak by Schittny et al. [127]

#### *1.2.5.5 Wireless temperature sensing*

Temperatures sensing has always been a very important aspect of any energy conversion system since it can reduce heat loss in a system, predict failure and enhance system efficiency. Numerous researches have been done to develop better temperature sensors. The necessity of wireless temperature sensors grew, as conventional wired sensing systems tend to be costly and hard to install and maintain. Many studies have been reported on developing wireless sensing technologies to develop cheap and accurate temperature sensors. Schimetta et al. [133] proposed a hybrid sensor for measuring pressure and temperature using Surface Acoustic Wave (SAW) reflective delay line but the proposed system lacked in accuracy and also had a low temperature limitation (up to 130 °C). Afterwards, advanced SAW based temperature sensors were realized for even moderately conductive media such as ionic water ink [134] or for high temperatures up to 1000 °C [135-137] and for better temperature resolution [138]. Although temperature sensors based on SAW propagation were useful for high temperature and harsh environments as they have the advantage of not having low thermal mass, low conductivity or the strong radiation coupling of the components at high temperature like most of the conventional approach, the acoustic wave propagation through the surface of the material does not depend only on the temperature but also on the geometric, environmental and material properties along the path, which makes it difficult to obtain reliable data [139]. Wireless temperature sensors utilizing a resonating inductor-capacitor (LC) circuit were another approach to overcome these limitations of SAW sensors. A wireless, passive, remote sensor based on a resonating LC circuit was proposed by Ong et al. [140]. The characteristic resonance frequency of this circuit was dependent on the temperature and was the basis of measuring temperature. Later, this concept was applied to measure temperature of a rotating component with a sensitivity of 30kHz/°C. The authors used a capacitive sensing element made of Lead-Lantanum-Zirconate-Titanate (PLZT) ceramic layer coated with NiCr, which can act as a parallel plate capacitor that is connected to an inductive antenna. The dielectric constant of the ceramic layer is temperature dependent and it can withstand up to 200 °C. Complementary Metal Oxide Semiconductors (CMOS) are another

approach to the temperature sensing which has gained attention over the years. Unfortunately, multiple components of this system make the fabrication complicated [141] and limit the operating temperature range [142]. Most of the developed sensing techniques required some power source, which makes it difficult to implement them at high temperatures. Therefore, an increasing demand of passive sensors is still present especially for harsh environment applications. Wang et al. [139] suggested a passive wireless temperature sensor for harsh environment in 2008 based on a completely passive LC resonant telemetry scheme but the sensor was calibrated and tested for only up to 235 °C. Recently, Cheng et al. demonstrated a resonator/antenna integrated passive wireless sensor using alumina as a dielectric substrate. The sensor was tested in the temperature range from 50 °C – 1000 °C while the resonance frequency of the structure decreased from 5.12 to 4.74 GHz with a sensitivity of 0.4 MHz/°C [143]. A schematic of the sensor is presented in Figure 2.2. The use of LC resonance circuits as a temperature sensing unit and the concept of representing a SRR structured metamaterials as a LC equivalent circuit inspired researchers to develop metamaterial based passive wireless temperature sensors since it offers more versatility, and scalability in design and also needs fewer components compared to the conventional LC circuit or CMOS circuits. So far, only a few studies suggesting

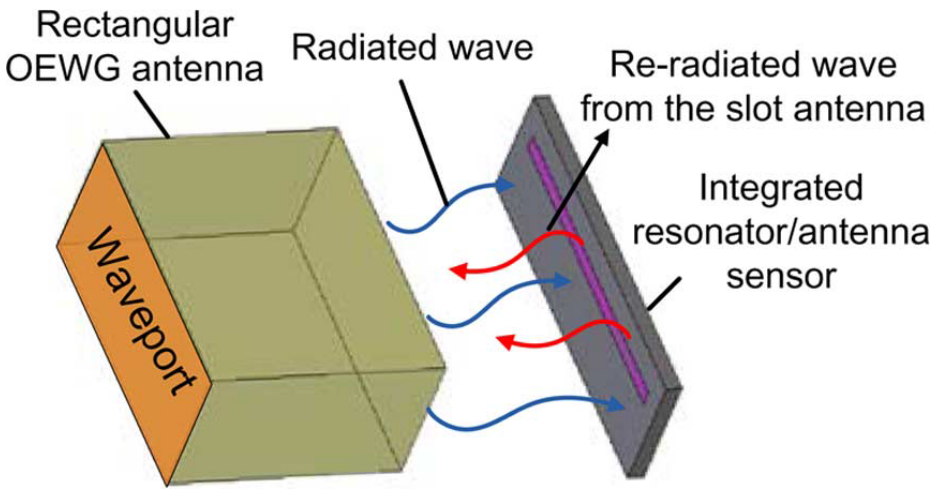


Figure 1.9: Schematic of wireless sensing of integrated resonator/antenna sensor developed by Cheng et al. [143]

metamaterials based wireless temperature sensors have been reported in literature. Thai et al. proposed an ultrasensitive wireless passive temperature transducer combining SRR structures with micro bimorph cantilevers [144]. The bilayer cantilevers deflect with the change of temperatures and thus shift the resonance frequency of the SRR structured resonators. The authors demonstrated a proof of concept utilizing Aluminum-PET (Polyethylene terephthalate) bilayer cantilevers that achieved a sensitivity of 2.14 MHz/°C. Ekmekci et al. [145] also demonstrated the feasibility of a metamaterial-based multi-functional sensor for temperature, humidity, density and pressure sensing. The authors proposed a double-sided split ring resonator (DSRR) topology with an additional sensing medium sandwiched between two identical broadside couple SRR unit cells. The resonance frequency of the DSRR unit changes when the thickness or the dielectric permittivity of this interlayer medium changes with the change of temperature, density, humidity or pressure of the environment surrounding the sensor. The authors used seawater as the interlayer medium for the demonstration of temperature sensing and achieved a sensitivity of 7.5 MHZ/°C with the change of temperature from 10 °C to 30 °C.

#### *1.2.5.7 Conclusion*

Although many studies have been conducted over the years to develop a passive wireless temperature sensor sustainable in harsh environments, there are still several drawbacks of the current solutions, mostly due to the need of a power supply, complicated fabrication processes or temperature limitations. Metamaterials based temperature sensors have been proposed lately but have not been demonstrated for high temperature applications and hence further studies are needed to establish this as a suitable alternative of the current solutions.

## 1.3 Pyroelectric energy harvesting

### 1.3.1 Introduction

Energy harvesting provides the possibility of self-powered devices for continuous operation with an almost inexhaustible source of energy [146]. Various sources of energy harvesting has been investigated such as piezoelectric generators [147, 148], thermoelectric

microgenerator [149-151], pyroelectric nanogenerators [6, 152, 153], photovoltaic devices [154, 155] and electromagnetic microgenerators [156, 157]. As pyroelectric materials require temporal temperature gradient (dT/dt) instead of a spatial temperature gradient (dT/dx), which is more difficult to realize at micro/nanoscale [158], compared to theremoelectric devices, they are better suited for the conversion of thermal energy into electrical energy at small scale. Pyroelectric materials such as $LiNbO_3$ that have high curie temperature (~1200 °C) provides another advantage over thermoelectrics for harvesting energy from high-temperature environments. In addition, pyroelectric energy harvesting devices require low or no maintenance since they do not include any moving parts unlike piezoelectric energy harvesting devices.

The term pyroelectricity is derived from the direct relationship between polarization and temperature. Pyroelectric materials form a subgroup of piezoelectrics, while ferroelectrics form a subgroup of pyroelectrics [159]. Pyroelectric materials display a spontaneous change in polarization when subjected to a temperature change. When the temperature of the material is slightly increased, the change in electric polarization of the material creates a potential difference between certain faces of the pyroelectric sample. Conversely, if the temperature is decreased by the same amount, the same magnitude of change in polarization occurs with the sign reversed.

All crystals can be categorized into 32 different classes based on their (i) center of symmetry, (ii) axes of rotation, (iii) mirror planes, and (iv) several combinations of the elements [159-161]. These 32 points groups are further subdivided into 7 basic crystal systems: triclinic, monoclinic, orthorhombic, tetragonal, rhombohedral (trigonal), hexagonal and cubic. There are 21 noncentrosymmetric groups among these 32 crystal groups that exhibit piezoelectricity with the exception of point group 432. Among these 21 groups, the pyroelectric effect can be observed only in those materials whose point-group symmetry is consistent with the vector property of the polarization. Pyroelectric materials include crystalline materials (whose structures belong to 10 point groups: 1, m, 2, mm2, 3, 3m, 4, 4mm, 6, and 6mm) and ceramics (which are polymeric and composite materials whose structures belong to textural or basic Curie point groups:∞, ∞m) [159]. Pyroelectric materials can be classified into two principle categories:

(i) nonferroelectric pyroelectric materials, which have unchangeable polarization with the application of an external electric field. Some semiconductors and biological materials fall within this category, and (ii) ferroelectric pyroelectric materials, which has polarization that can be changed with an electric field and are needed to be poled. The pyroelectric property of these materials is present below curie temperature and is more dependent than the nonferroelectric pyroelectric materials. To summarize, ferroelectrics is a subclass of pyroelectrics, which are in turn, a subclass of piezoelectrics, which generally belong to the main class of dielectrics. Consequently, all ferroelectrics are pyroelectric, and all pyroelectric materials are also piezoelectric, however, the reverse relationship is not true.

### 1.3.2 Theory

Pyroelectricity is defined as the spontaneous polarization in certain anisotropic crystals that are created by a change in temperature [162-164]. This effect generates an electric current/potential in materials with non-centrosymmetric crystal structure when subjected to a temporal temperature gradient (dT/dt). The dipole moment per unit volume of the material is defined as the spontaneous polarization and pyroelectric materials have a unique polar axis along which the spontaneous polarization exists [162, 164]. The pyroelectric coefficient $p$ is defined as the differential change in the spontaneous polarization $P$ of the material caused by a change in temperature [165]. Pyroelectricity is a coupled effect where a change in temperature causes a change in electric displacement $\boldsymbol{D}$. There are two contributions to the pyroelectric effect [159]. The first contribution is from the primary pyroelectric effect caused by the change in temperature, which produces a change in the electric displacement in a crystal under a constant strain $x$, rigidly clamped to prevent change in dimension. The second contribution is the result of crystal deformation, which is due to the thermal expansion from temperature change that causes strain in the piezoelectric process, which in turns alters the electric displacement. The pyroelectric effect an constant stress $X$ and electric field $E$ can be expressed as [159]:

$$\left(\frac{\partial \boldsymbol{D}}{\partial T}\right)_{E,X} = \left(\frac{\partial \boldsymbol{D}}{\partial T}\right)_{E,x} + \left(\frac{\partial \boldsymbol{D}}{\partial x}\right)_{E,T}\left(\frac{\partial x}{\partial T}\right)_{E,X} \quad (1)$$

where, $\boldsymbol{D}$, $x$, and $T$ are the electric displacement, strain and temperature of the pyroelectric material, respectively. The first term of the right side of equation (1) is the primary pyroelectric response or effect. The second term represents the secondary effect that arises from the piezoelectric effect where additional charge is produced due to the piezoelectric contribution from thermal expansion. For a ferroelectric material, the electric displacement is related as [159],

$$D = P + dX \tag{2}$$

where, $d$ is the piezoelectric coefficient of the material, and $P$ is the polarization, defined as [159],

$$P = P_s + \varepsilon E \tag{3}$$

where, $E$ is the electric field, $P_s$ is spontaneous polarization and $\varepsilon$ is permittivity. From equation (1) and (2) the pyroelectric coefficient $p$ can be derived,

$$p = \left(\frac{\partial \boldsymbol{D}}{\partial T}\right)_{E,X} = \left(\frac{\partial P}{\partial T}\right)_{E,x} + E\left(\frac{\partial \varepsilon}{\partial T}\right)_{E,X} \tag{4}$$

where, the first term in the right side is the primary pyroelectric coefficient below the curie temperature and the second term is the pyroelectric coefficient significantly closer to the curie temperature, where the change of dieletric permittivity due to the change of pyroelectric is quite significant. Now, from equation (4), if E=0 (no applied electric field), or the permittivity of the material does not change with temperature and the dimensions of the material is considered constant, then the primary pyroelectric coefficient ($P_p$) only corresponds to the change in spontaneous polarization with temperature and can be expressed as:

$$P_p = \left(\frac{\partial P_s}{\partial T}\right)_{E,X} \tag{5}$$

The secondary pyroelectric coefficient ($P_s$) is described as:

$$p_s = \left(\frac{\partial \boldsymbol{D}}{\partial x}\right)_{E,T}\left(\frac{\partial x}{\partial T}\right)_{E,X} = \left(\frac{\partial \boldsymbol{D}}{\partial X}\right)_{E,X}\left(\frac{\partial X}{\partial x}\right)_{E,T}\left(\frac{\partial x}{\partial T}\right)_{E,X} = dc\alpha \tag{6}$$

where $c$ is the elastic stiffness, $d$ is the piezoelectric co-effiecient, and $\alpha$ is the thermal expansion coefficient of the material. It is noteworthy here that the pyroelectric coefficient is generally a vector, however, for practical purposes is treated as a scalar [159]. Lee et al. [166] reported the

primary, secondary and observed pyroelectric coefficient values of several materials, some of the commonly investigated materials are listed in table 1.1.

**Table 1.1.** Primary, secondary, and observed pyroelectric coefficients of some materials at room temperature [159, 166]

| **Materials** | **Point group symmetry** | **Observed total effect ($\mu C/m^2K$)** | **Calculated secondary effect ($\mu C/m^2K$)** | **Primary effect ($\mu C/m^2K$)** |
|---|---|---|---|---|
| $BaTiO_3$ | ∞m | -190 | +80 | -270 |
| $LiTaO_3$ | 3m | -176 | +2 | -178 |
| $LiNbO_3$ | 3m | -83 | +12.9 | -95.9 |
| $NaNO_2$ | 2mm | -140 | -5 | -135 |
| $Li_2SO_4(H_2O)$ | 2 | +86.3 | +26.1 | +60.2 |
| Tourmaline | 3m | +4 | +3.2 | +0.8 |
| Bone | ∞ | $+25x10^{-4}$ | $+117x10^{-4}$ | -92x10 |
| $Ba_2Si_2TiO_8$ (Fresnoite) | 4mm | +10 | +22, +16 | -12, -6 |
| $Li_2GeO_3$ | 2mm | -27 | -12.8 | -14.2 |
| CdS | 6mm | -4 | -1 | -3 |
| CdSe | 6mm | -3.5 | -0.56 | -2.94 |
| ZnO | 6mm | 0.43 | +0.34 | --- |
| BeO | 6mm | -3.4 | -0.008 | -339 |

The current generation process during the heating and cooling of a pyroelectric material is illustrated in Figure 1.10. When the pyroelectric sample does not have electrodes, the spontaneous polarization attracts free charges (shown as positive and negative circles) to the material's surface, and in result, masking the charges Figure 1.10 (a). When the sample has electrodes but is not subjected to a temperature change (Figure 1.10 (b)), no current is generated.

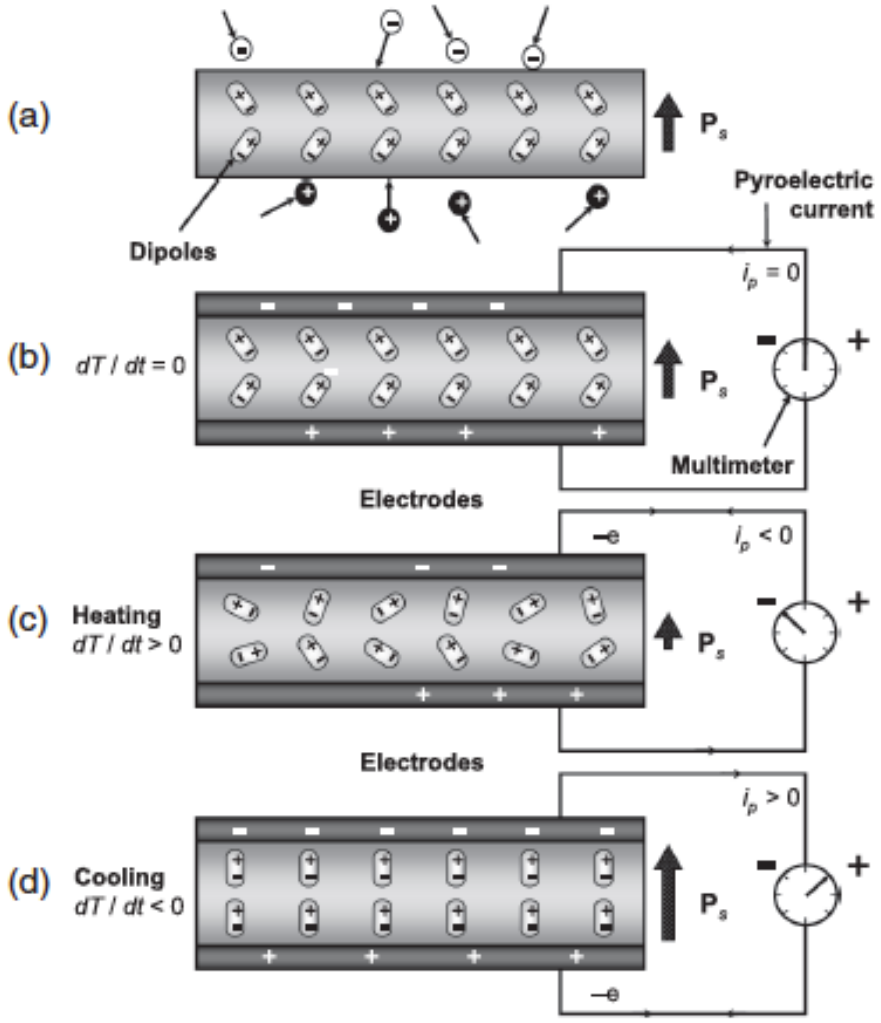


Figure 1.10: Pyroelectric sample showing dipoles and polarization vector, (a) without electrodes, (b) with electrodes, connected to an ammeter at constant temperature, (c) while heating, and (d) while cooling [159]

When the pyroelectric sample with electrode is heated (Figure 1.10 (c)), there is a reduction in dipole movement toward polar alignment, which reduces the spontaneous polarization and consequentially, reduces the charge-storage capacity of the material. The decrease in the quantity of the bound charges leads to the ejection of bound charges, creating current flow through the external circuit. When the sample is cooled (Figure 1.10 (d)), the spontaneous polarization increases and attracts ambient charges to the surface of the electrodes and generates a current with the sign reversed.

The pyroelectric current $i_p$, generated while heating or cooling is generally expressed as [32],

$$i_p = \frac{dQ}{dt} = Ap\frac{dT}{dt} \tag{7}$$

where, $Q$ is the induced charge, $A$ is the electrode surface area, $p$ is the pyroelectric coefficient, and $dT/dt$ is the rate of temperature change with time. The direction of the flow of current is dependent on the direction of temperature change with respect to time (heating or cooling). Pyroelectric cells are generally modeled as current sources [167]. The generated charge can be found integrating (7) over time:

$$Q = \int_{t_i}^{t_f} Idt = \int_{t_i}^{t_f} Ap\frac{dT}{dt}dt = \int_{t_i}^{t_f} ApdT = Ap(T_f - T_i) \tag{8}$$

where, $T_f$ and $T_i$ are temperatures at the considered final and initial time respectively. Therefore, based on (3) the amount of charge does not depend on the temperature change rate; rather it depends on the temperature difference [167].

### 1.3.3 Literature review

Pyroelectricity is one of the least known electrical properties of solid materials [164]. Although the phenomenon was known for more than 24 centuries and was found in natural materials such as tourmaline crystal, the theoretical analysis has emerged in modern times. The first scientific description of pyroelectricity was written in 1717, but the quantitative understanding of this effect did not transpire until the nineteenth century [162, 164]. Eventually, pyroelectric materials have found applications in diverse fields as smart materials, especially in energy harvesting and sensing. For energy harvesting, they convert the thermal energy from temporal change in temperature to electricity, and in sensors, they are used as sensing elements to detect heat (or indirectly motion) signals by conversion into an electric signal. Recently, Sarker et al. reported the concept of temperature sensing using pyroelectric materials [4]. To keep the discussion pertinent to the scope of the dissertation, only recent progress on nanowire, nanofibers, thin film and bulk pyroelectrics in the application of energy harvesting will be addressed in this section.

### *1.3.3.1 Nano and micro scale materials and devices*

Significant numbers of research have been done on the development of nano and microscale pyroelectric energy harvesting devices consisting of nanofibers, nanowires, microwires and thin films. The principle advantage of thin film is that it offers a large surface area to facilitate improved thermal exchange and current output [168, 169]. The technological advancement in nanotechnology has provided the opportunity to harvest energy using 1D materials such as nanowires and nanofibers (Figure 1.11) [32, 164]. The size of the pyroelectric element has been used to tailor the phase transition temperatures in ferroelectric nanowires [170, 171]. It was theoretically shown that the pyroelectric coefficient can be tuned by modifying the nanowire radius and the nature of the surrounding media such as template material, gas or gel as the ferroelectric-ambient interface controls the surface energy properties; this shows a great potential for nanoscale pyroelectric energy harvesting.

Another advantage of nanowires is that they encompasses enhanced mechanical properties in comparison to the bulk materials [172]**,** often resulting because of the lowered defect in these materials. This property allows the nanowires to withstand larger strains compared to bulk materials, which makes them very attractive for flexible nanogenerators, which holds promise for wearable electronics (Figure 1.11 (d)) [153, 164, 173]**.** It was also demonstrated that nanowires show enhanced piezoelectric and thermoelectric properties compared to their bulk complements [174, 175]. Yang et al. [32] estimated from experimental studies the pyroelectric coefficient of ZnO nanowires to be ~1.2-1.5 $nC/cm^2K$, which is larger than the values for the bulk and thin films of ZnO (~1$nC/cm^2K$). Nanowires have also found their application into composite structures to develop multifunctional smart materials. Composite nanogenerators based on $KNbO_3$, which is a low cost and easily available material were recently reported (Figure 1.11 (c) & (d)) [153].

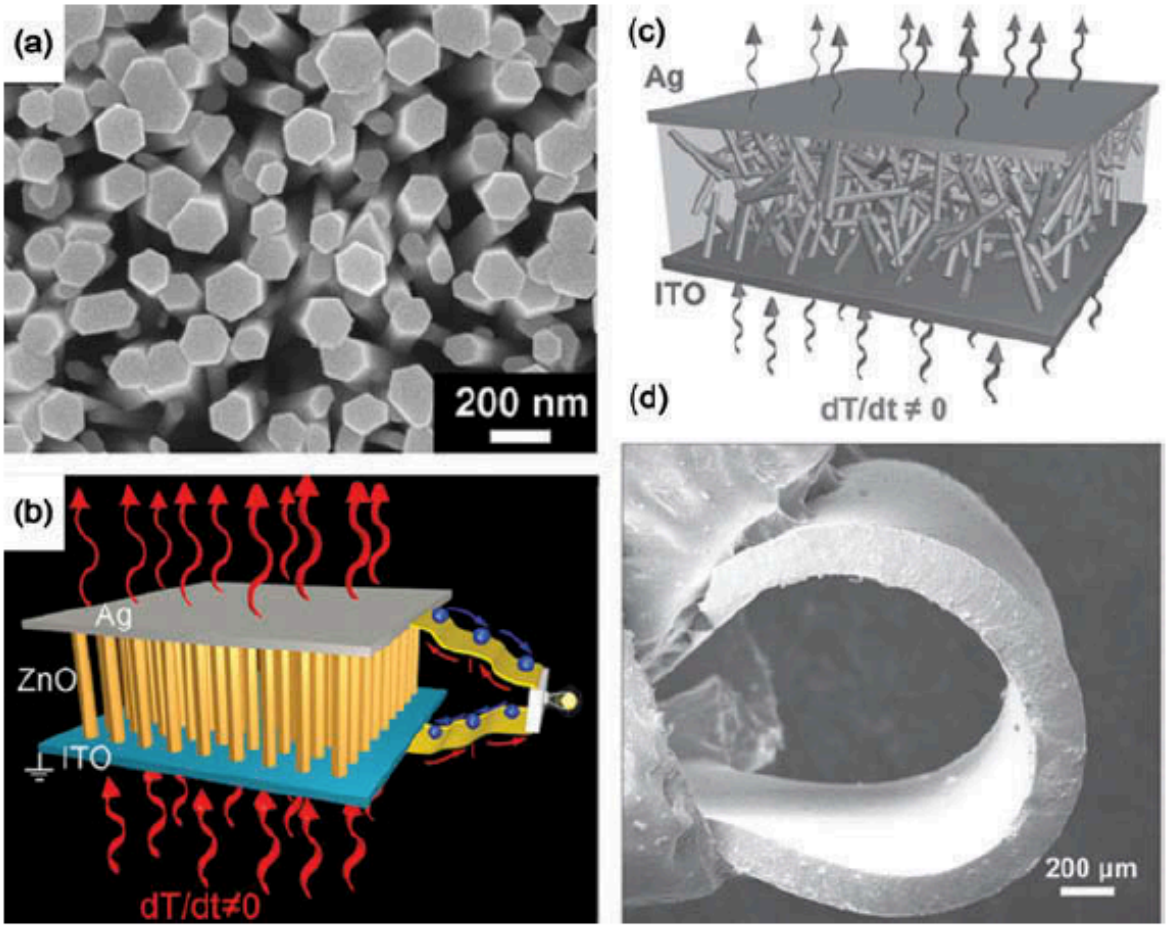


Figure 1.11: Pyroelectric energy harvesting from nanowires and nanowire composites. (a), (b) vertical bundle of ZnO nanowires are sandwiched between two electrodes [32, 164]. Copyright (2012) American Chemical Society. (c), (d) flexible pyroelectric nanogenerator based on KNbO3 nanowire composites [153, 164]. Copyright (2012) John Wiley and Sons

Nanofibers are also getting increasing attention in addition to nanowires for pyroelectric energy harvesting. The major advangtage of nanofiber is that they are generallly mechanically soft and can be readily integrated into flexible devices [175, 176]. The most common fabrication method for nanofibers is electrospinning [164, 177]. Polyvinylidene fluoride (PVDF) and its copolymer poly(vinylidene fluoride-trifluoroethylene) P(VDF-TrFE) has been synthesized using this technique [178], which are high-performance thermoplastic with excellent mechanical and physical properties. They are also chemically inert towards most acids, solvents, oxidants,

alcohol and halogens [179]. Recent developments of PVDF microgenerators for portable devices make it a very interesting area for self-powering devices.

At the microscale, it was demonstrated that a single PZT microwire can produce enough power to energize temeperature sensors [180]. A single PZT microwire was placed on a glass substrate and silver paste was used as electrodes on its two ends. The device was then packaged inside polydimethylsiloxane (PDMS) and the device was poled electrically at a voltage of 3.5 kV. The device was then placed on a heater and the generated temporal temperature change was used for the pyroelectric energy harvesting. Hsiao et al. [181-183] has reported that etching of the pyroelectric surface and the electrode structure improves energy harvesting performance as partially covered top electrodes provide a higher current and voltage compared to the fully covered electrode as it allows the pyroelectric layer to be in better contact with the heat source [184]. They also demonstrated that a meshed top electrode and trenched pyroelectric improved the responsitivity of the PZT as the trenched architecture enhances the rate of temperature change due to a lateral temperature gradient. Branch like and vortex-like electrodes with deep structure was also created (Figure 1.12) [183] using sandblasting technique. It was observed that the harvested power was improved by 11% compared to a fully covered electrode.

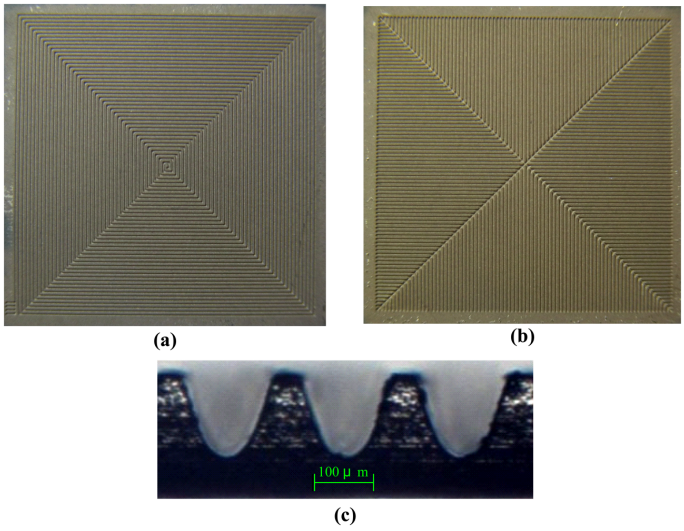


Figure 1.12: Fabricated pyroelectric cells: (**a**) vortex-like electrode; (**b**) branch-like electrode; (**c**) cross section of trenches [183]

### *1.3.3.2 Hybrid generators*

Since all pyroelectric materials are also piezoelectric, there have been several investigations to combine both these energy-harvesting properties. Hybrid flexible energy cell for simultaneously harvesting thermal-mechanical-solar energy has been introduced by Yang et al. [185] with PVDF film for piezoelectric and pyroelectric harvesting unit along with a ZnO-poly(3-hexylthioohene) hetero-junction solar cell for solar energy harvesting (Figure 1.13). A pyroelectric coefficient of ~44 μC m−2 K−1 was measured. Using a lithium-ion battery to store the harvested energy the device could drive four red light-emitting diodes (LED). Lee et al. [186] fabricated a stretchable, piezoelectric-pyroelectric hybrid nanogenerator based on a micropatterned piezoelectric P(VDF-TrFE) polymer sandwitched between micro-patterned PDMS-carbon nanotube (CNTs) composite and graphene nanosheets (Figure 1.14). Graphen was used in the top layer due to its high thermal conductivity to facilitate enhanced heat transfer rate

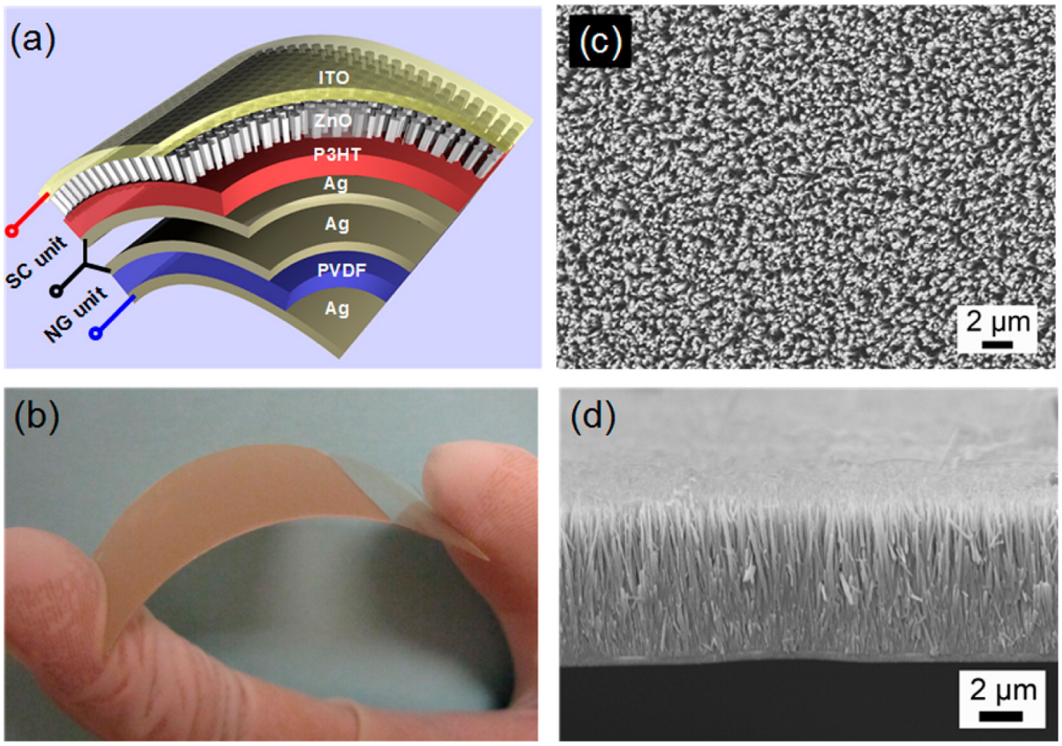


Figure 1.13: (a) Schematic diagram of the fabricated hybrid energy cell (b) Photograph of the bent ZnO nanowire array grown on an ITO/PET substrate (c) SEM image of the ZnO nanowire array (d) Cross-section SEM image of the ZnO nanowire array [185]

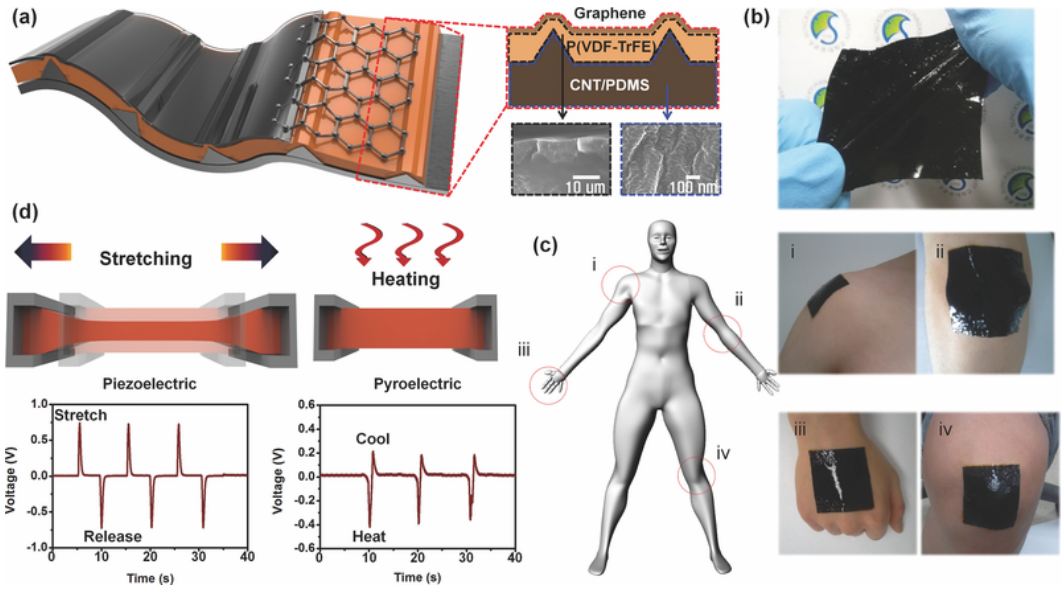


Figure 1.14: (a) Schematic illustration of the device, (b) photo image of the HSNG, (c) photo images of the HSNG at various locations on human body, showing good compatibility of the device with various parts of body, and (d) piezoelectric output voltage from the HSNG under stretch-release condition, and pyroelectric output voltage under a thermal gradient (heat and cool) [186]

to the device. The PDMS-CNT made the device flexible while also serving as a robust electrode. Energy harvesting using both mechanical loads and temperature changes were examined. Erturun et al. [187] investigated combined piezoelectric and pyroelectric energy harvesting utilizing PZT on a vibrating beam while subjected to heat by a heating lamp. The effects of pyroelectric and piezoelectric properties were investigated both individually and afterward coupled. It has been found that the combination can sometime result in having a negative effect on the amount of harvested energy and it is important to tune both parameters to optimize the performance of the device.

### *1.3.3.3 Pyroelectric systems and oscillators*

Different kind of pyroelectric energy harvesting systems and MEMS oscillators has been introduced recently. A MEMS based cantilever system for energy harvesting based on thermally cycled pyroelectric capacitor that acts as a bimorph cantilever was proposed by Oak Ridge National Laboratory [188, 189]. When the cantilever is heated it deforms because of the thermal

mismatch between the bimorph layers and consequentially comes in contact with the cold surface making the structure cool and deforming in the reverse direction and so on. The advantage of MEMS approach is that an array of devices could be used to increase the scavenged energy and this particular design can operate at high frequencies. Another approach to increase operating frequency was proposed by Cha et al. [190] using liquid-based switchable thermal interfaces which converts a spatial temperature gradient into temporal temperature oscillations. In this system, a pyroelectric material is actuated up and down making alternating thermal contact with the heat source and sink to undergo temperature oscillations (Figure 1.15). In the thermally conducting state, the actuator brings down the pyroelectric and presses it against the hot or cold surface and liquid droplets at the interface deform and produce a continuous thin liquid layer of low thermal resistance. The pyroelectric material is physically separated from the hot and cold surfaces during the non-thermally conducting state and the liquid on the pyroelectric interface exists as discrete droplets. The rupture distance was reduced by creating a hydrophilic pattern on the surfaces, this in turn reduced the distance required and enabled it to operate at high frequency of the order of 1 Hz.

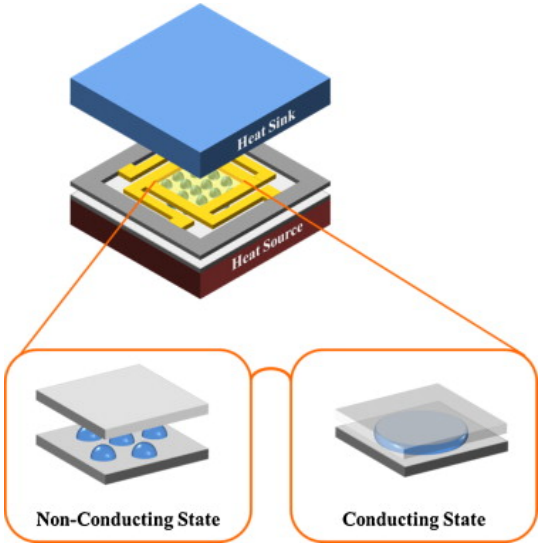


Figure 1.15: Pyroelectric energy harvesting module. The electrode assembly containing a pyroelectric material is actuated up and down to make alternating thermal contacts with the heat source (hot side) or source (cold side) via switchable thermal interfaces [190].

Huesgen et al. presented a micro heat engine based on a cavity filled with a liquid-gas phase change fluid that produces a reciprocating motion between a heat source and heat sink [191-193]. A bi-stable membrane generated an upward and downward motion between the heat source and sink by buckling during expansion and contraction of the phase-change fluid. Carlioz et al. [194] explored the idea of combining piezoelectric materials with hard and soft magnetic materials which has a temperature variant attracting force. Kotipalli et al. [195] reported a micro-system consisting of a carbon nanotube film integrated with a PZT cantilever for harvesting light and thermal energy. The carbon layers absorb the thermal radiation, consequently changes the shape of the carbon layer and induces bending into the piezoelectric cantilever. It was demonstrated by Zhang et al. [196] that a pyroelectric material under solar radiation can produce sufficient energy to acquire pyroelectric effect only from fluctuation induced by wind variation. Krishnan et al. [197] advanced this concept further and developed a pyrorelectric-based solar and wind harvester and obtained maximum power density of 421 $\mu W.cm^{-3}$ for a PZT prototype. Battista et al. [198] used an optical system to focus solar-radiation onto $LiNbO_3$ (LNB) and utilized the pyroelectric property of LNB to harvest energy. The exposed face was coated with carbon black-graphene particles nanocomposite that improved the adsorption of solar radiation onto the LNB crystal. Bhattacharjee et al. [199] investigated the feasibility of capturing thermal energy from natural heating of pavements and utilizing this as alternative power source to sensor bridges. It was shown that addition of carbon nanofibers increases the pyroelectric properties of the cement.

A major concern for piezoelectric and pyroelectric energy conversion is its very low efficiency. One approach to improve the effectiveness of the energy conversion is proposed in [200] by utilizing the concept of the 'Synchronized Switch Harvesting on Inductor' (SSHI), which was first developed for energy harvesting from piezoelectric materials [200] and then expanded to pyroelectric energy harvesting [201]. The SSHI contains a switching device and an inductor parallel to the pyroelectric materials. The switching device and the inductor are in series. The switch is opened and closed in a controlled way to enhance the energy harvesting.

The experimental results show that under the same heating condition, the efficiency from 0.02% of the Carnot efficiency with a standard interface to 0.05% of Carnot efficiency using a SSHI interface.

## 1.4 Dissertation overview

The following two sections will present the contributions of this research in the development of functional materials for energy system applications and will provide a brief description of the research performed in each chapter.

### 1.4.1 Contributions

The emissions from the fossil fuel based energy conversion systems are a subject of big concern for the global climate. The emission performance of these systems can be improved by having improved moitoring of the key parameters such as temperatuere of the combustion process. On the first part of the dissertation a metamaterial based design of a passive and wireless temperature sensor for harsh environment application was investigated to ensure higher efficiency of operation of those systems. The first contribution lies to the development of a CRR (Closed Ring Resonator) based temperature sensor design. Most commonly used metamaterial design consists of split ring resonators, which are complex to fabricate. It was shown that the CRR based design is not only simple; it is more sensitive to the change in temperature compared to the other split based structures. The second contribution is the approach to a macro level manufacturing of metamaterials. While, most traditional metamaterial-based design uses technology such as lithography, which is very complex and costly, a simpler fabrication technique based on traditional powder compression is investigated. The limitation of the proposed sensor is also investigated. It is known that the alignment between the sample and antennas in the test setup are very important to get reliable result in microwave transmission or reflection based measurement. The dissertation makes an effort to quantify the effect of misalignment between the antennas on the response of the sensor in the transmission operation. The effect of some environmental parameters such as humidity and stress is also investigated.

The second part of the dissertation reports a new material for pyroelectric energy harvesting to decrease the waste heat of any energy systems. The most widely used pyroelectric material is Lead Zirconate Titanate (PZT), which contains environmentally detrimental material Lead and also has a low curie temperature around 300 °C. The contribution of this dissertation lies in reporting $LiNbO_3$ as a lead free alternative material for pyroelectric energy harvestings, which also has a very high curie temperature over 1000 °C that makes it highly suitable for the energy conversion systems. The energy harvesting was demonstrated using different kind of diodes and supercapacitors and was shown that the individual circuit elements are also highly important in obtaining the maximum energy output from these sources.

### 1.4.2 Chapter summary

Chapter 1 provides the introduction of the concept and theories pertaining to the dissertation as well as summarizes the pervious work in the related areas. It starts with motivation behind this project and then discusses the concept behind the metamaterial based wireless temperature sensor. The application of metamaterials and the recent work of metamaterials at different areas as well as recent developments of wireless temperature sensing is also discussed. The chapter then provides the introduction to the pyroelectric energy harvesting and explains the theory of operation of the material and discusses the recent developments in the energy harvesting area.

Chapter 2 conducts a feasibility study of a metamaterial based design of a passive and wireless temperature sensor for harsh environment application. The proposed sensor would have a resonance frequency that will change linearly with the change in temperature. The CRR structure was chosen for the simplicity of the structure and for ease of fabrication as commercial washers could be used as a cheap source of the CRR structure and high cost fabrication techniques such as lithography could be avoided. The details of the CRR based design, preliminary simulation using HFSS comparing the CRR design to other Split Ring Resonator

(SRR) structures and the investigation of geometric parameters on the design are found in this chapter.

Chapter 3 discussed the finalization of the design based on the preliminary design from chapter 2, fabrication and test of the sensor up to 200 °C. This chapter explains the reasoning and steps behind the selection of materials, details the synthesis and fabrication procedure, material characterization using SEM and XRD as well as dielectric properties characterization using waveguides and split cavity resonators. Some preliminary simulations are discussed prior to the experimental investigation. The test results illustrating the sensor response as a function of temperature is analyzed and more investigation in the material property using HFSS simulation to predict the dielectric properties of the sensor are also carried out.

Chapter 4 investigates the limitation of this sensor. Three factors were chosen for the investigation. First, the importance of a perfectly aligned test setup was investigated by measuring the sensor response at different angles of misalignment between the transmitting and receiving antennas. The second factor that was investigated was the effect of humidity. The third factor investigated was the effect of compressive stress on the sensor response. The chapter discusses the details of the experiments and results in each case.

Chapter 5 reports a lead free alternative of PZT for pyroelectric energy harvesting. $LiNbO_3$ (LNB) is the proposed material, which has lower pyroelectric coefficient, however, the significantly higher curie temperature compared to PZT makes it appealing for high temperature operations of the energy conversion systems. The feasibility of the material as a pyroelectric energy harvester was demonstrated as well as importance of choosing the proper circuit elements such as diodes and capacitor was also investigated and reported.

The final chapter of the dissertation is chapter 6, which draws the conclusion with a brief overview of the results found throughout the dissertation. It then outlines the recommendation of future work that can be performed to improve the design and performance of the sensor as well as to achieve higher efficiency in the energy harvesting from pyroelectric materials.

# Chapter 2: Concept and Model of a Metamaterial-Based Passive Wireless Temperature Sensor for Harsh Environment Applications

## 2.1 Introduction

Wireless passive sensors are highly desirable for measuring critical parameters in harsh environments and remote sensing platforms. Sensing in harsh environments such as high temperature and corrosive conditions is crucial in many automotive and industrial applications such as power plants, gas turbines, space shuttles and air crafts. These applications require that the sensor is easy to fabricate, cheap, small, easy to integrate and highly reliable. However, most existing solutions require a power source or have low temperature limitations [144, 202, 203]. Optical based wireless sensors were developed but the accuracy was not satisfactory [204, 205]. SiC and $Si_3N_4$ based micro-sensors have been introduced in a harsh chemical environment at high temperature, but the complexity of the fabrication process makes it costly [206, 207]. Temperature sensing has received wide attention recently because of its importance for the effective operation of many industrial systems. Several approaches were made to develop a passive, wireless temperature sensor for high temperature operations. Scott and Peroulis [208] presented a slot antenna with an embedded temperature sensor which can sense up to 300°C. Yang [23] proposed a silicon carbide wireless sensing system that can operate at 450°C under high centrifugal load. Cheng et al. [143] have developed a resonator/antenna based wireless temperature sensor and reported test results at 1000°C. Thai et al. [144] used micro-bimorph cantilevers to develop an ultrasensitive temperature sensor working at a high frequency of 30 GHz. Metamaterials have drawn significant attention lately because of their ability to display extraordinary properties such as negative refractive index, reverse Doppler effect etc. [48, 209-211]. Several approaches were reported to develop wireless sensors inspired from the concept of metamaterials, which are man-made materials that can display properties that are not normally observed in nature. A metamaterials based Surface Plasmon Resonance (SPR) sensor in terahertz region was proposed by Arbabi et al. [212]. Melik et al. demonstrated an RF-MEMS and nested SRR based setup for strain measurement [213]. He et al. [214] developed a thin layer sensor with

tip-shaped SRR metamaterials for microwave region. Xia et al. [215] proposed a sensor based on a single SRR metamaterial structure for wireless sensing of gas density, temperature, gas pressure, etc. Ekmekci et al. [145] demonstrated the feasibility of DSRR (Double Sided Split Ring Resonator) structure based wireless sensors for applications in temperature, humidity, density, concentration or pressure sensing. However, the common methods of fabricating SRR structures such as photolithography or electron beam lithography make the fabrication complicated and costly. In this study, a metamaterial inspired cheap, passive wireless temperature sensor is proposed that can work in high temperature and harsh environments. This is achieved by using a dielectric matrix that embeds two CRR structures. The sensor unit can be represented as an LC circuit and the resonance frequency of this circuit/structure will change with the change of temperature enabling the measurement of temperature. The model is validated through finite element method and the effect of different geometry and combination of SRR structures on the sensitivity and electrical sizes of the proposed sensor are evaluated.

**2.2 Concept and model of the sensor**

The proposed sensor has two metal CRR embedded in a dielectric material matrix, which separates them as depicted in Figure 2.1(a). The dielectric matrix surrounding the metal CRRs helps protecting the metals from harsh and corrosive environments. The unit cell can be simplistically represented by LC resonant circuit (Figure 2.1 (b). The resonant frequency *f* of the structure can be expressed as:

$$f = \frac{1}{2\pi\sqrt{LC}} \tag{1}$$

where, *L* and *C* is the total inductance and capacitance of the unit cell respectively. Calculations for the capacitance and inductance terms can be found elsewhere [216-218]. CRR structure was chosen to make the fabrication of the sensor easy and cheap as commercially available washers can be used as a CRR structure and complicated fabrication process like photolithography can be avoided.

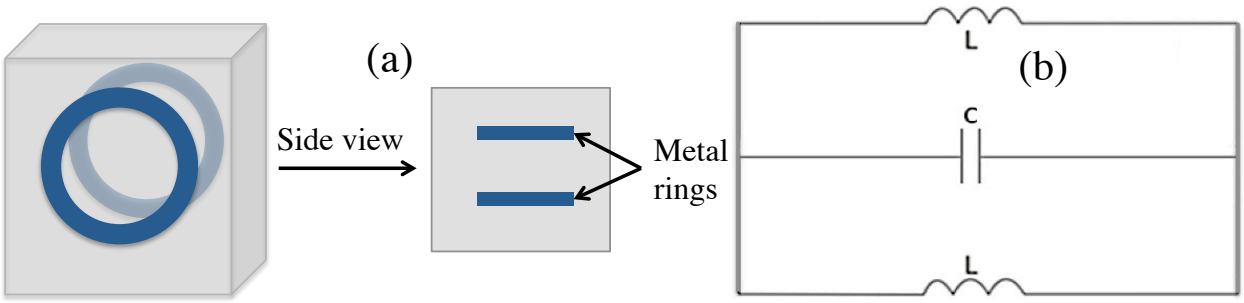


Figure 2.1: (a) Proposed model of the temperature sensor (b) Equivalent circuit

**2.3 Different SRR structure and their response with varying parameters**

To determine the geometry and configuration of proposed wireless temperature sensor, finite element based modeling was performed using Ansys Ansoft HFSS (High Frequency Structural Solver) 15.0, which is a full wave electromagnetic solver. Parameters for the sensor modeling process consisting of two CRR (Closed Ring Resonators, as shown in Figure 2.2) were evaluated to validate the feasibility of this structure for the sensing application. The most common SRR structures, i.e. EC-SRR (Edge Coupled-SRR) and BC-SRR (Broadside Coupled-SRR) and other variations developed from these common structures were assessed for the effect of substrate thickness, dielectric constant and split gap of the SRRs on the resonance frequency of the sensor unit. The different structures considered for the study is shown in Figure 2.3.

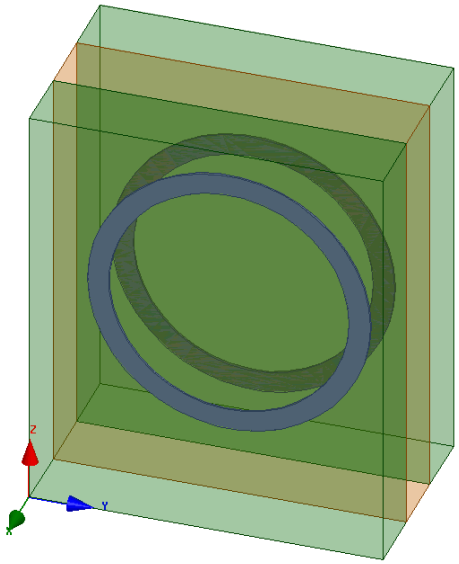

Figure 2.2: Proposed sensor based on CRR structure modeled in Ansys Ansoft HFSS

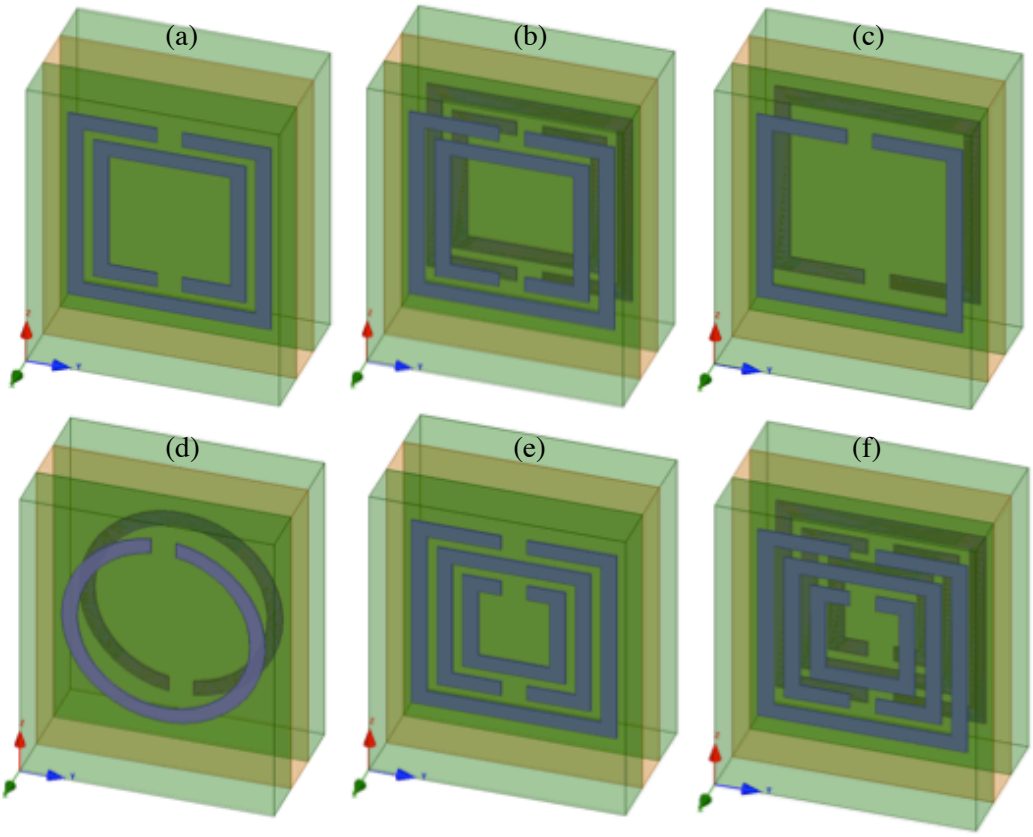


Figure 2.3: Sensor model with different SRR structures: (a) EC-SRR (b) DSRR (c) BC-SRR (d) BC-CSRR (e) MSRR (f) DMSRR

In all the models, a dielectric material separates two ring resonator structures. The distance between these two rings are $d$ as identified in Figure 2.4. The length = width = $L$ = 6mm, and thickness = $D$ = 3mm. The sides of each ring is $l_1$ = 4mm (all structures except CRR), $l_2$ = 3mm (not present in BC-SRR, BC-CSRR, CRR structure), $l_3$ = 2mm (only in MSRR and DMSRR). The width of the metal rings $w$ = 0.3mm and thickness $t$ = 0.03mm are same for all the SRR structures in every model. Except for CRR, all other ring resonator structures have a split of $s$ mm. The outer diameter for CRR and CSRR structure is 4 mm. In case of EC-SRR, DSRR, DMSRR, and MSRR, separation between the two rings are $g$ = 0.1 mm.

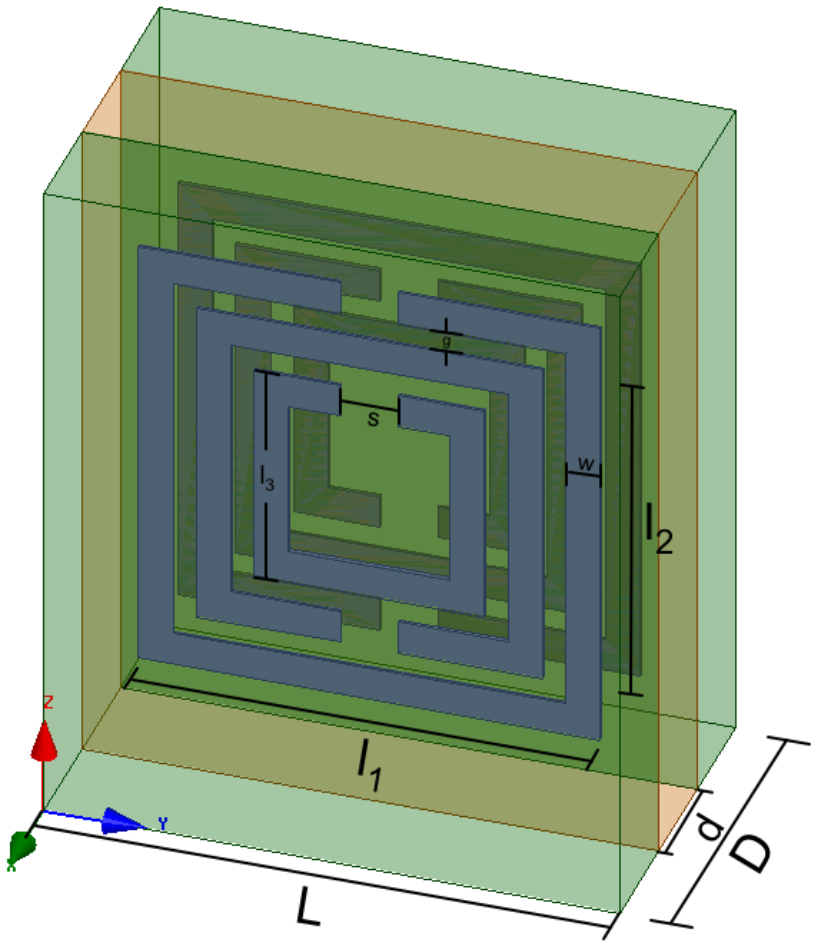


Figure 2.4: An DMSRR model showing all the geometry parameters

**2.4 Effects of the substrate thickness (d) on resonance parameters**

To determine the effect of substrate thickness on sensor characteristic, transmission spectra of different SRR structured sensor model are simulated by the HFSS software using the geometry parameters constant as mentioned above but varying for different substrate thickness, d= 0.5 mm, 1 mm, 1.5 mm, 2 mm, 2.5 mm and 3 mm.

As the substrate thickness d of the CRR structure increases from 0.5mm to 3mm, the resonance frequency of this sensor structure decreases from 14.44 GHz to 12 GHz with a sensitivity of 976 MHz/mm over the range as shown in Figure 2.5 (a). While for EC-SRR structure, the variation is small with all the resonance frequencies within 2.5-2.6 GHz. The sensitivity for 1 mm substrate thickness increase for this structure is 28 MHz/mm.

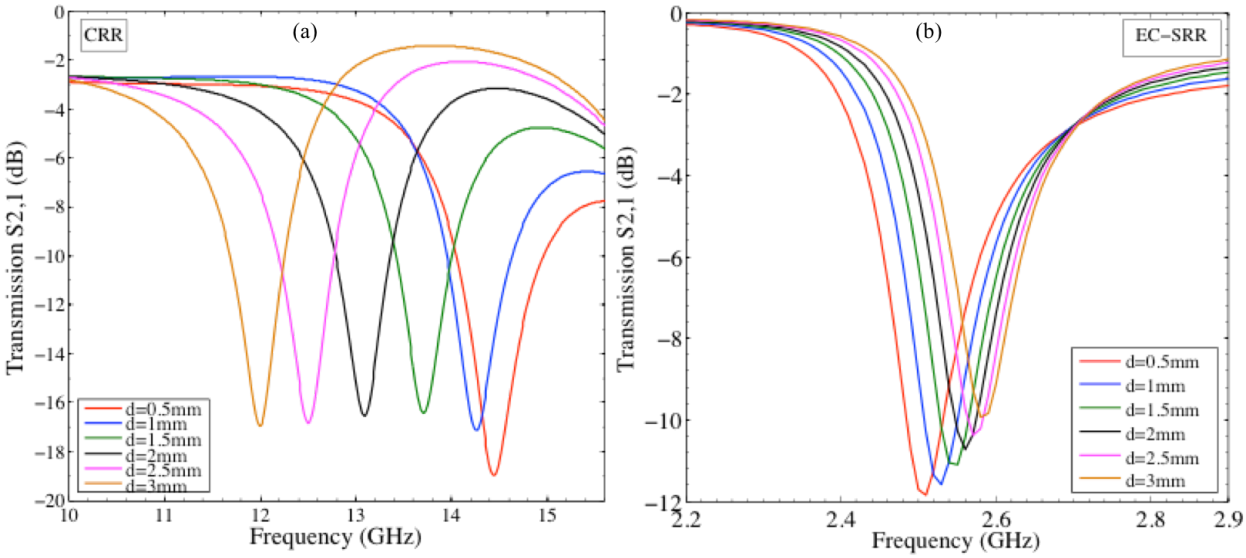


Figure 2.5: Transmission spectrum, (a) CRR, (b) EC-SRR

For DSRR, as this structure has SRR structures on both sides, changing the substrate thickness has greater influence on the resonance frequency than the EC-SRR structure. A drop in the resonance frequency value is also expected because of the higher capacitance between the SRRs on opposite sides. As shown in Figure 2.6 (a), for DSRR structures, the resonance frequency increases from 2.00 GHz to 2.44 GHz and the sensitivity of thickness change is 176 MHz/mm. For BC-SRR structure, the resonance frequency increases from 2.3 GHz to 2.98 GHz with a sensitivity of 272 MHz per mm, as shown in Figure 2.6(b). It should be noted that the resonance frequency values for this structure is in between EC-SRR and DSRR since there is only one SRR structure on each side; there is no capacitance effect between neighboring SRRs as in case of DSRR structure. But, because of the higher capacitance between the SRRs on opposite sides, the resonance frequencies are lower than EC-SRR structure. As expected, DMSRR structure has a little lower resonance frequency then DSRR structure. The frequency range for this structure is from 2 GHz to 2.43 GHz with a sensitivity of 172 MHz / mm.

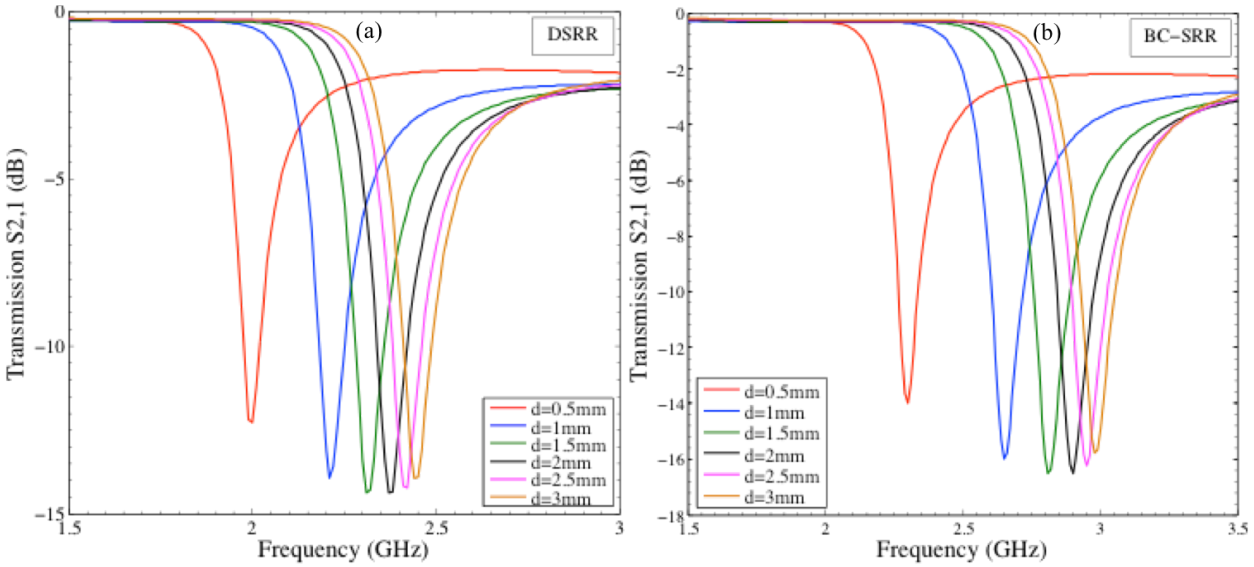


Figure 2.6: Transmission spectrum, (a) DSRR (b) BC-SRR sensor structures

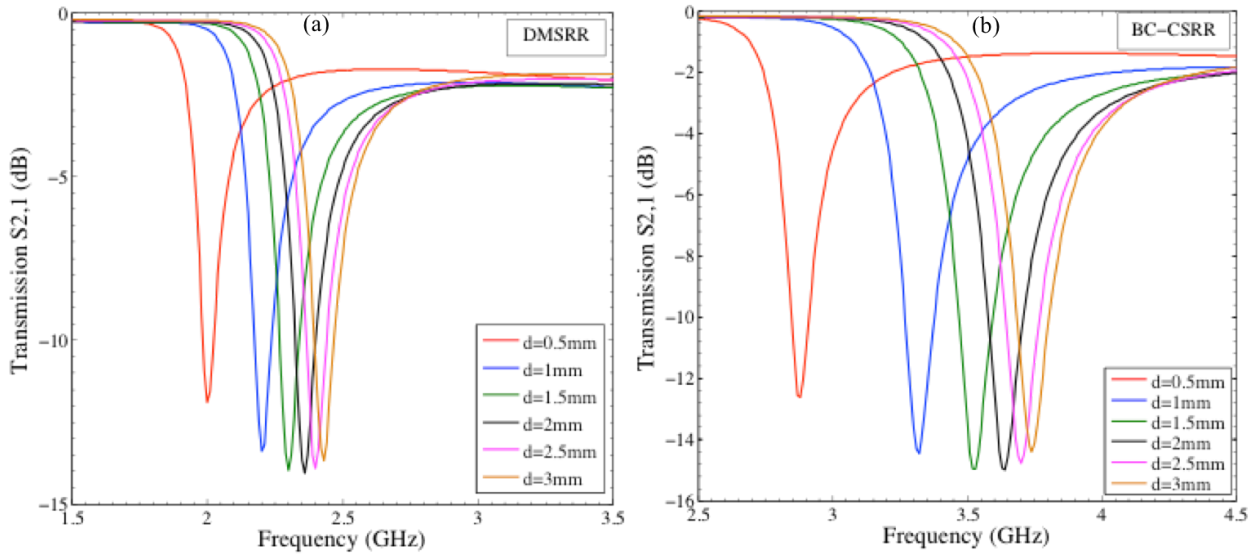


Figure 2.7: Transmission spectrum, (a) DMSRR (b) BC-CSRR sensor structures.

BC-CSRR structure, which basically consists of circular split rings instead of square rings and has the diameter equal to one side of the square SRR in BC-SRR structure displays a higher resonance frequency at any substrate thickness than the BC-SRR structure and the range of resonance frequency for BC-CSRR structure is from 2.88 GHz to 3.74 GHz with sensitivity of

344 MHz/mm. MSRR structure displays resonance frequency close to the EC-SRR structure since there is only one additional ring added to the EC-SRR structure. It demonstrates that

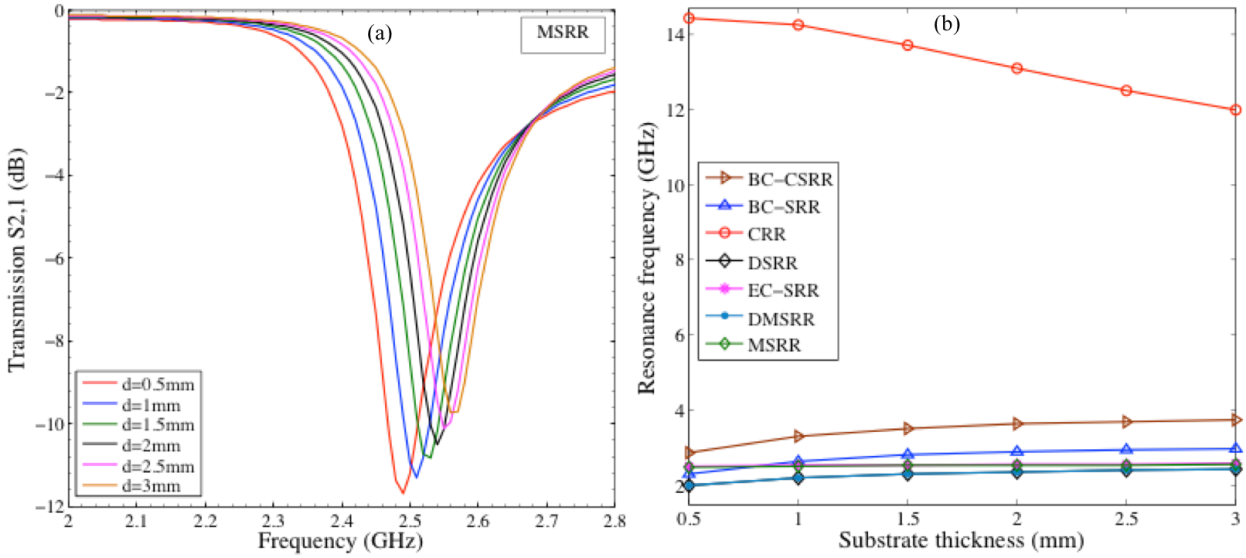


Figure 2.8: (a) Transmission spectra, MSRR structure (b) Effect of substrate thickness on resonance frequency for different SRR structured units.

adding more SRR structure on one side will decrease the resonance frequency. The sensitivity of this structure in terms of substrate thickness is also 28 MHz/mm.

Figure 2.8 (b) depicts a comparison among all the different structures in terms of their change in resonance frequency with the change of substrate thickness. Only CRR structure shows a decrease in resonance frequency with the increase of the substrate thickness and all the other structures display increase but with different sensitivity. Also, CRR structure has the highest sensitivity to the change of substrate thickness than the other structures.

### 2.5 Effects of the split gap (g) on resonance parameters

Effect of split gap on the resonance frequency of the structure was evaluated from a gap of 0.2 mm to 3.4 mm. All the other parameters were kept constant. Thickness of each dielectric material layers were 1 mm, ring thickness = 0.03 mm, length of the sides of the SRR was 4mm by 4mm and same materials were used. Since the CRR structure has no split, this parameter is

not applicable to this structure. All the other structures show an increase of resonance frequency with the increase of split gap as shown in Figure 2.12. The highest change in resonance

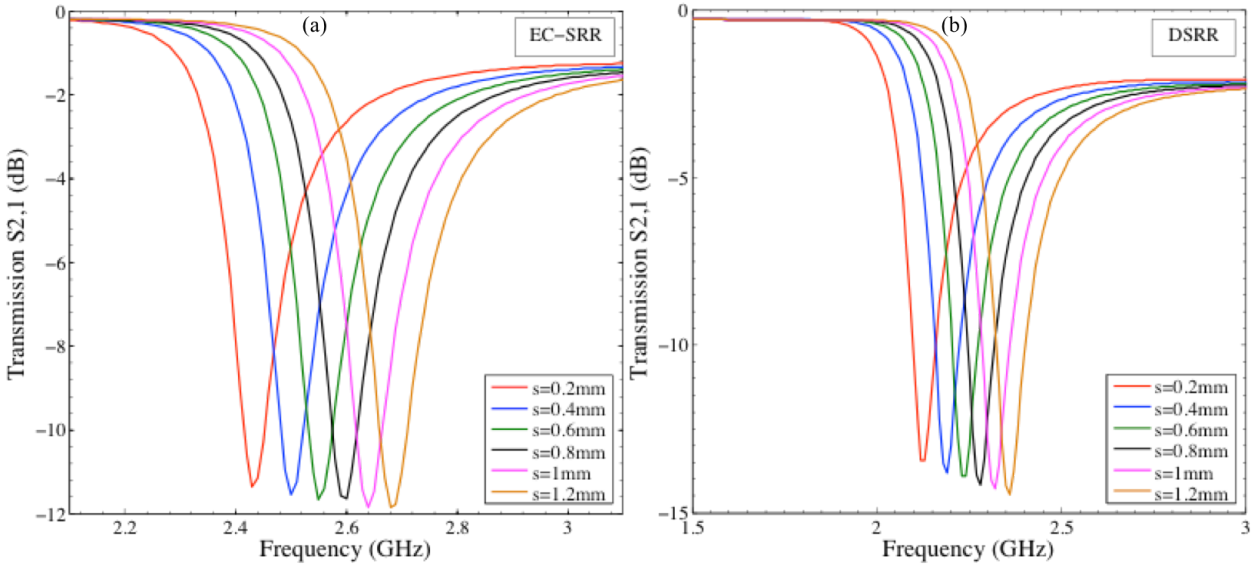


Figure 2.9: Transmission spectra, (a) EC-SRR structure (b) DSRR structure

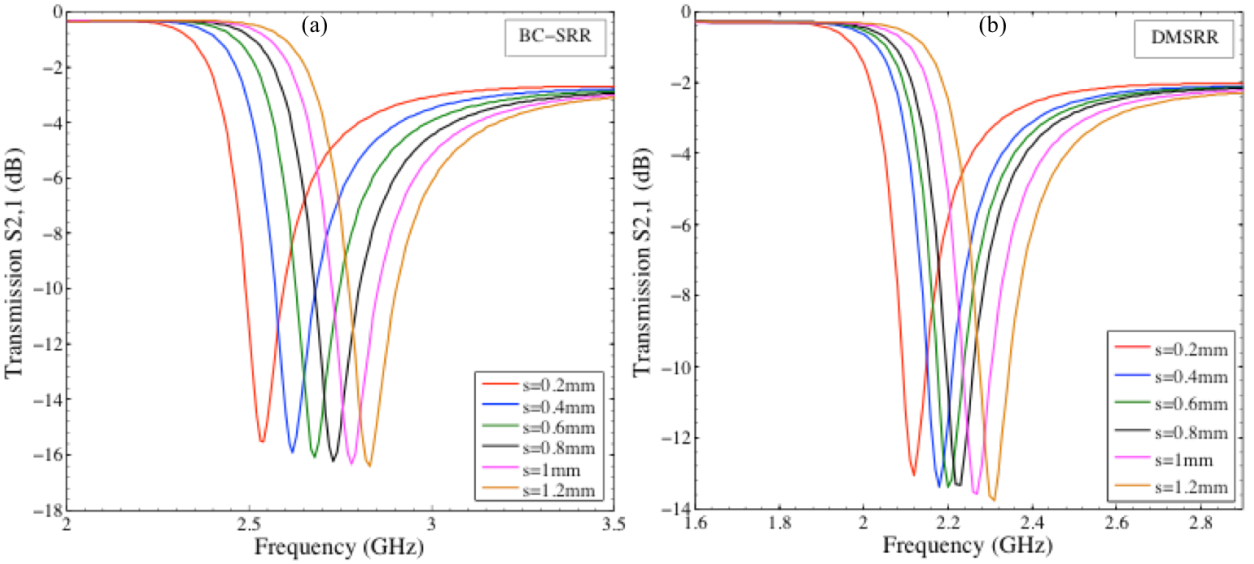


Figure 2.10: Transmission spectra, (a) BC-SRR structure (b) DMSRR structure

frequency was observed for the BC-CSRR structure which shows a change of 470 MHz increase with 1 mm increase of the split gap. The BC-SRR structure displays a change of the resonance frequency from 2.54 to 2.83 GHz with a total change of 290 MHz. The least sensitive structure

among these structures is the DMSRR, which shows a change of 190 MHz as the resonance frequency increases from 2.12 to 2.31 GHz. The EC-SRR and MSRR structure displays similar behavior and also has the resonance frequency values really close to each other. It is seen that the resonance frequency is reduced with the introduction of one additional SRR structure in the EC-SRR structure.

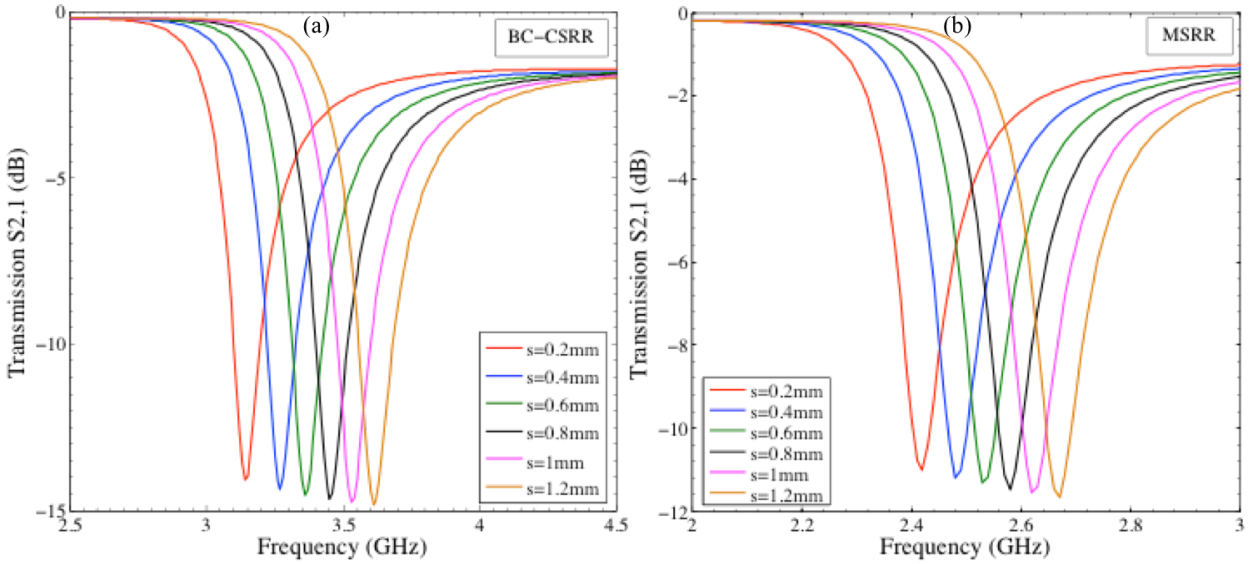


Figure 2.11: Transmission spectra, (a) BC-CSRR structure (b) MSRR structure

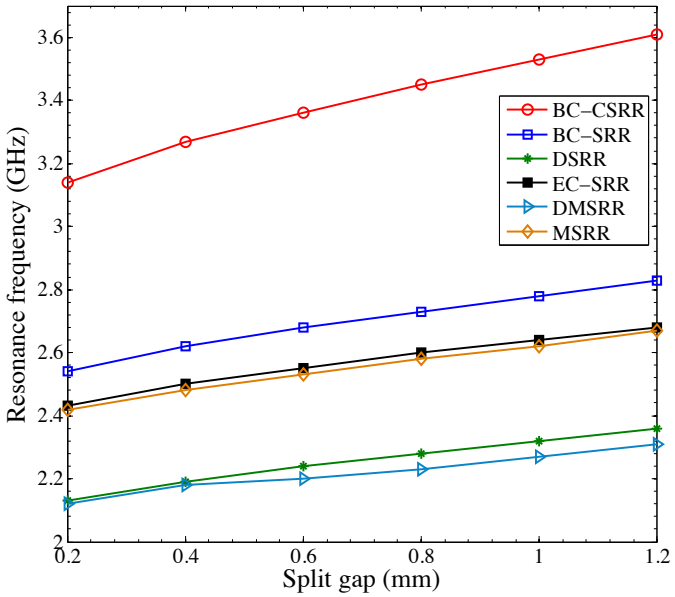


Figure 2.12: Effect of split gap on resonance frequency for different SRR structured units.

## 2.6 Effect of relative permittivity ($\varepsilon_r$) on the resonance frequency

To evaluate the temperature sensitivity of the sensor structures, standard dielectric constant of $LiNbO_3$ from 400 °C to 800 °C was taken into account [219], which varies from 52 to 145 within this temperature range. Using the dielectric constant of 52, 55, 65, 76, 87, 110 and 145 at temperatures 400 °C, 500 °C, 600 °C, 700 °C, 800 °C respectively, the temperature sensitivity of all the different structures was evaluated. All the structures show a decline in the resonance frequency with the increase of temperature. While CRR structure shows the highest resonance frequency values as expected, it also shows the highest sensitivity of 6.375 MHz/°C. The sensitivity for BC-CSRR, BC-SRR, DSRR, EC-SRR, DMSRR and MSRR structures are 1.475 MHz/°C, 1.15 MHz/°C, 0.975 MHz/°C, 1.125 MHz/°C, MHz/°C and 1.1 MHz/°C respectively. The transmission values for the CRR structures with different dielectric constant and comparison of the all structures are shown in Figure 2.13 (a) and (b) respectively.

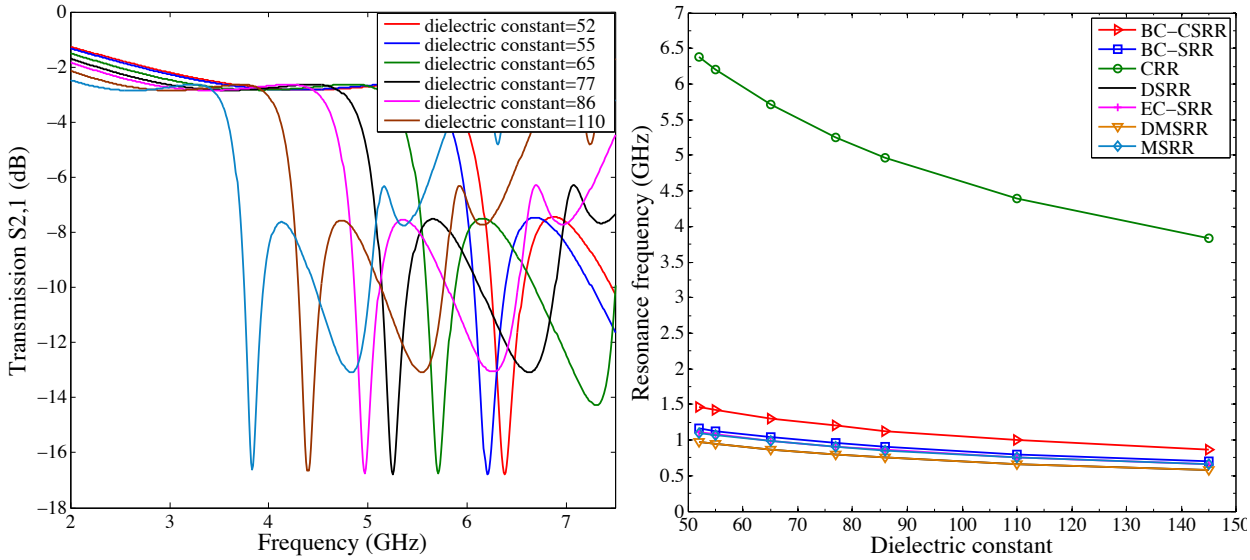


Figure 2.13: (a) Transmission spectra, CRR structure (b) Effect of dielectric constant on resonance frequency for different SRR structured units.

## 2.7 Comparison of the Electrical sizes of the sensor model with different SRR structure

Electrical size is a very important parameter for a metamaterial unit cell because smaller electrical size provides more effective medium approximation and more accuracy from the quasi-static analysis is also expected. The electrical size of the different structure can be calculated

using equation (2.1) and to have a common base of comparison for all the structures, the resonance frequency values for dielectric constant of 145 from figure 2.13 (b) are used. It is observed that for all the substrate thickness and relative permittivity values DSRR and DMSRR structure has the smallest electrical size 0.016 while the CRR structure has the highest electrical size 0.108. The electrical size for the BC-CSRR, BC-SRR, EC-SRR, DMSRR and MSRR structure is 0.0246, 0.0198, 0.0186, and 0.0187 respectively. Electrical size of a resonator cell is defined as [220],

$$u = \frac{D}{\lambda_0} = \frac{D}{c/f_0} = f_0 \frac{D}{c} \tag{2.1}$$

Where, D = Maximum linear dimension of the resonator

= Diagonal of the square sample $= 8.49$ mm

$\lambda_0$ = Free space wavelength at the resonance frequency [220, 221]

c = Speed of light in vacuum = $3 \times 10^8$ m/s

$f_0$ = Resonance frequency of the resonator

**2.8 Conclusion**

Two CRR structure embedded in a dielectric ceramic matrix is proposed as a temperature sensor operable in high temperature and harsh environments. The use of CRR structure makes the fabrication cheap and simple as complex technique like lithography can be avoided. The feasibility of such sensor is validated through Finite Element Method using HFSS. In order to obtain the optimum dimensions, effect of substrate thickness and split gap was evaluated and also compared against other common metamaterial structures found in literature. A comparative analysis of the sensitivity of each structure was examined using the dielectric constant of $LiNbO_3$ at different temperatures. It was demonstrated that proposed CRR structure is highly sensitive to the change of temperature and hence a good candidate for a temperature sensor.

# Chapter 3: Design, Fabrication and Test of the Metamaterial based Passive Wireless Temperature Sensor for Temperatures up to 200 °C

## 3.1 Introduction

In chapter two, the feasibility of a metamaterial based temperature sensor has been evaluated using Ansoft HFSS and CRR based geometry was proposed for such a sensor considering the ease of fabrication as well as higher sensitivity to change in dielectric constant, i.e. temperature. In this chapter a sensor has been designed, fabricated and tested based on the concept presented in chapter two. Due to the instrumental constraints the working range of the sensor was chosen to be 7-16 GHz. Two high temperature dielectric material $BaTiO_3$ (BTO) and Boron Nitride (BN) was mixed to get the desired dielectric properties of the sensor. Copper washers purchased from Mcmaster-carr was used as the CRR structure to avoid complicated fabrication techniques. The detailed design, preliminary calculation and simulation, material characterization, fabrication and experimental test and results will be discussed in this chapter.

## 3.2 Design and Material Selection

Conventional powder compression using die-punches was chosen to be used for the fabrication of the sensor as will be discussed later. Consequentially, the biggest sample that could be made by this method was 2" by 2" (Across International). However, the antenna that were used in the tests had a beam diameter of 2.5", which made the sample too small to avoid the edge effect and get reliable results. Hence, four samples of 2" by 2" dimensions were made and assembled to have a sample of 4" (101.6mm) by 4" (101.6mm) dimensions. The thickness of the sensor was 9/32".

Barium Titanate (BTO) is a ceramic material which is robust to chemically harsh environments, has a high melting point (1625 °C), and also significantly high dielectric constant which is very sensitive to temperature [222]. These properties make BTO very desirable for the purpose of temperature sensing. However, both the real and imaginary part of the permittivity is still quite high resulting in significantly high loss tangent values [223], which would result in a

decrease of the transmitted signal through the sensor unit. Preliminary simulations were done to evaluate the effect of loss values to the transmission response of the sensor and it was found that if the loss value is above 0.1 the resonance peak loses its intensity significantly and it would be very difficult to obtain significant resonance response from the sensor and as BTO has a loss value of about 0.7 at the desired working range of this sensor, it would be clearly unable to provide a resonance response significant enough to detect.

To address this issue Barium Titanate (99.95%, advancedmaterials.us) was incorporated with another ceramic material, Boron Nitride (BN) (US research nanomaterials, Inc.) with high melting point, but low dielectric constant and more importantly significantly low loss, 0.005 at 17 GHz from room temperature to up to 600°C [224]. Another advantage of using BN is that it has a somewhat constant dielectric constant with the change of temperature and frequency. Therefore, the temperature sensitivity comes from only one material, i.e. BTO and avoids the setback of having two different trends in two materials.

There are several approaches to predict the dielectric constant values of a mixture of two different dielectric materials [225-227]. Maxwell-Garnett method [228] gives a good approximation of mixture involving nanoparticles, however, it assumes that one material is sparsely dispersed into a host material. On the other hand the Bruggeman method [229] assumes that the low content material $\epsilon_{r2}$ is present such a way that any block of material will contain of $\epsilon_{r1}$ material. This is a better approximation of the system under investigation. The Bruggeman effective media is described as [227]:

$$f\frac{\epsilon_{r1}-\epsilon_B}{\epsilon_{r1}+2\epsilon_B}+(1-f)\frac{\epsilon_{r2}-\epsilon_B}{\epsilon_{r2}+2\epsilon_B}=0 \tag{3.1}$$

where, $\epsilon_{r1}$ is the dielectric constant of the host medium (BN), $\epsilon_{r2}$ is the dielectric constant of the second medium (BTO), $\epsilon_B$ is the dielectric constant of the mixture, and $f$ is the fill fraction of $\epsilon_{r1}$. The solution for the Bruggeman method can be found using the following equations [227],

$$\epsilon_B=-\frac{B+\sqrt{B^2-4AC}}{2A} \tag{3.2}$$

$$B=(\epsilon_{r1}-2\epsilon_{r2})+3f(\epsilon_{r2}-\epsilon_{r1}) \tag{3.3}$$

$$C=-\epsilon_{r1}\epsilon_{r2} \tag{3.4}$$

where, A is a constant = 2. The fill fraction was taken to be 0.7. The dielectric constant of BTO and BN at 12 GHz was taken to be 124.71 and 4 respectively. The dielectric constant of BN was reported at 1 MHz from the supplier and 17 GHz [224] and it was seen that the value has minimal change with the change in measurement frequency, the dielectric constant for BN was taken as 4. The dielectric constant of BTO was taken 124.71 at 8 GHz [223]. The dielectric constant and the loss properties of the mixture was calculated using equations (3.1) to (3.4) for 10% increments of BN in the mixture as shown in table 3.1.

**Table 3.1.** Calculated properties of BN-BTO mixture using Bruggeman effective medium equations

| **Fill fraction (BN)** | **Bruggeman Effective Dielectric Constant** | **Bruggeman Effective Dielectric Loss** | **Density-mixture** |
|---|---|---|---|
| 0.1 | 106.94 | 0.597 | 5618 |
| 0.2 | 89.29 | 0.495 | 5216 |
| 0.3 | 71.86 | 0.393 | 4814 |
| 0.4 | 54.83 | 0.292 | 4412 |
| 0.5 | 38.63 | 0.194 | 4010 |
| 0.6 | 24.32 | 0.104 | 3608 |
| 0.7 | 13.90 | 0.043 | 3206 |
| 0.8 | 8.22 | 0.020 | 2804 |
| 0.9 | 5.46 | 0.013 | 2402 |
| 1 | 4.00 | 0.009 | 2000 |

From the table, it can be seen that for the mixture of 70% BN and 30% BTO, the loss value drops below 0.05 and this was chosen as the ratio for the sample as it is desired to use the minimum amount of BN possible to retain the sensitivity of the sensor as high as possible. Preliminary simulations were done using these material properties in Ansoft HFSS to investigate the response of the sensor at the desired range (6-18 GHz). The unit cell design is shown in

Figure 3.1(a). Floquet ports were used for the excitation whereas master and slave boundaries were applied on the faces perpendicular to the x and y axis to make the unit cell repeated infinitely along the x and y axis. The transmission response of the infinite array is shown in Figure 3.1(c). After observing the desired resonant behavior of the sensor for the ideal case of infinite array simulation, it was necessary to see the response of a finite simulation, which would be more realistic. The sample dimension for this simulation was taken to be 4" by 4" to replicate the final sensor assembly. Perfectly Matched Layer (PML) boundaries were used to make the boundary condition finite and waveports were used for the excitation. The sensor along with airbox and PML boxes are shown in Figure 3.1(b) and corresponding transmission response is shown in Figure 3.1 (d). It can be seen that the response from the finite simulation is very similar to the infinite conditions demonstrating the feasibility of obtaining resonance from the 4" by 4" sample design.

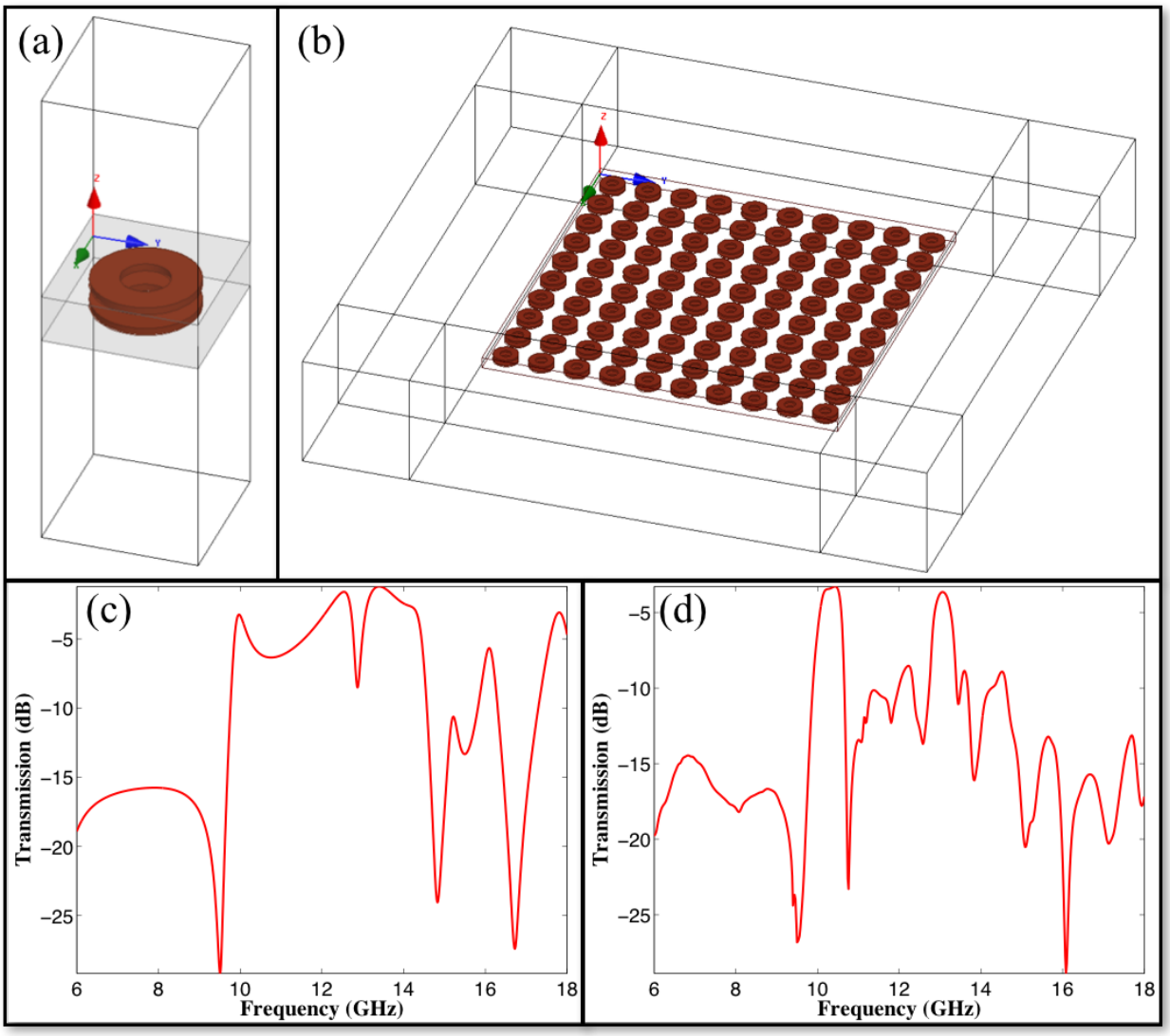


Figure 3.1: Preliminary simulation using Ansoft HFSS (a) Unit cell with airbox (b) Finite simulation setup with airbox and PML boxes surrounding the airbox (c) Transmission response of the unit cell shown in (a) and (d) Transmission response of the finite cell shown in (b).

### 3.3 Sample preparation & Material Characterization

Based on the preliminary simulation results, 70% BN (volume) was mixed with 30% of BN. Polyvinyl Alcohol (PVA) was used as a binder as the dry mixture of BN and BTO after compression was developing cracks. Since, it was desired to use the minimum amount of PVA possible, several samples were made using incremental amount of PVA and 7.5 wt% was found

to be the minimum required to hold the sample sufficiently. The details of the synthesis of PVA and the fabrication method are discussed in section 3.3.1.

The material properties were investigated using different material characterization tools. Scanning Electron Microscopy (SEM) was used to obtain the particle size of Barium Titanate (BTO) and Boron Nitride (BN). The microstructure of the materials after BTO, BN and PVA was mixed together, and after heating up the sample at 500 °C for 4h is also observed. X-ray Diffraction (XRD) was used to characterize the chemical composition of the material. Pure BTO and BN as well as the mixture of the materials were investigated. The dielectric properties of the materials were investigated using waveguide setup as well as cavity resonator setup. The real and imaginary values of the dielectric constant of the materials and the dielectric loss were characterized.

### 3.3.1 Sample preparation

#### *3.3.1.1 Synthesis of PVA*

Polyvinyl alcohol (99% hydrolyzed, Sigma Aldrich) was mixed with deionized (DI) water in a 1:10 ratio under heavy stirring (600 rpm) at room temperature. The PVA was added gradually into the DI water until the ratio was reached. After that, the solution was heated to 90 ºC until the powder was fully dissolved into the water, resulting in a transparent solution and was cooled down naturally to the room temperature.

#### *3.3.1.2 Fabrication*

Conventional method of powder compression was used to fabricate the samples. 30 vol% of BTO and 70 vol% of BN nanopowders were mixed in a mortar with 7.5 wt% PVA. The optimum amount of PVA was chosen experimentally [230]. The mixture was ground to achieve uniform binder distribution. After that, the ceramic/binder mixture was placed inside of the compressive die. Pressing the powder mixture by hand with the punch attained uniform surface to place the washers. The Cu washers and the guide that was used to place the washers are shown in Figure 3.2 (a) and (b) respectively. The second and third layers of the BTO-BN-PVA mixture

were prepared following the process aforementioned. Two layers of copper washers (25 washers in each layer) were placed and centered inside of the die in between each of the ceramic layers. The die was then placed inside of a CARVER pressing machine and compressed using 3 metric ton pressure for 10 minutes, as shown in Figure 3.2 (c). A schematic of the ceramic/washer configuration can be seen in Figure 3.2 (d). The fabricated samples are shown in Figure 3.3.

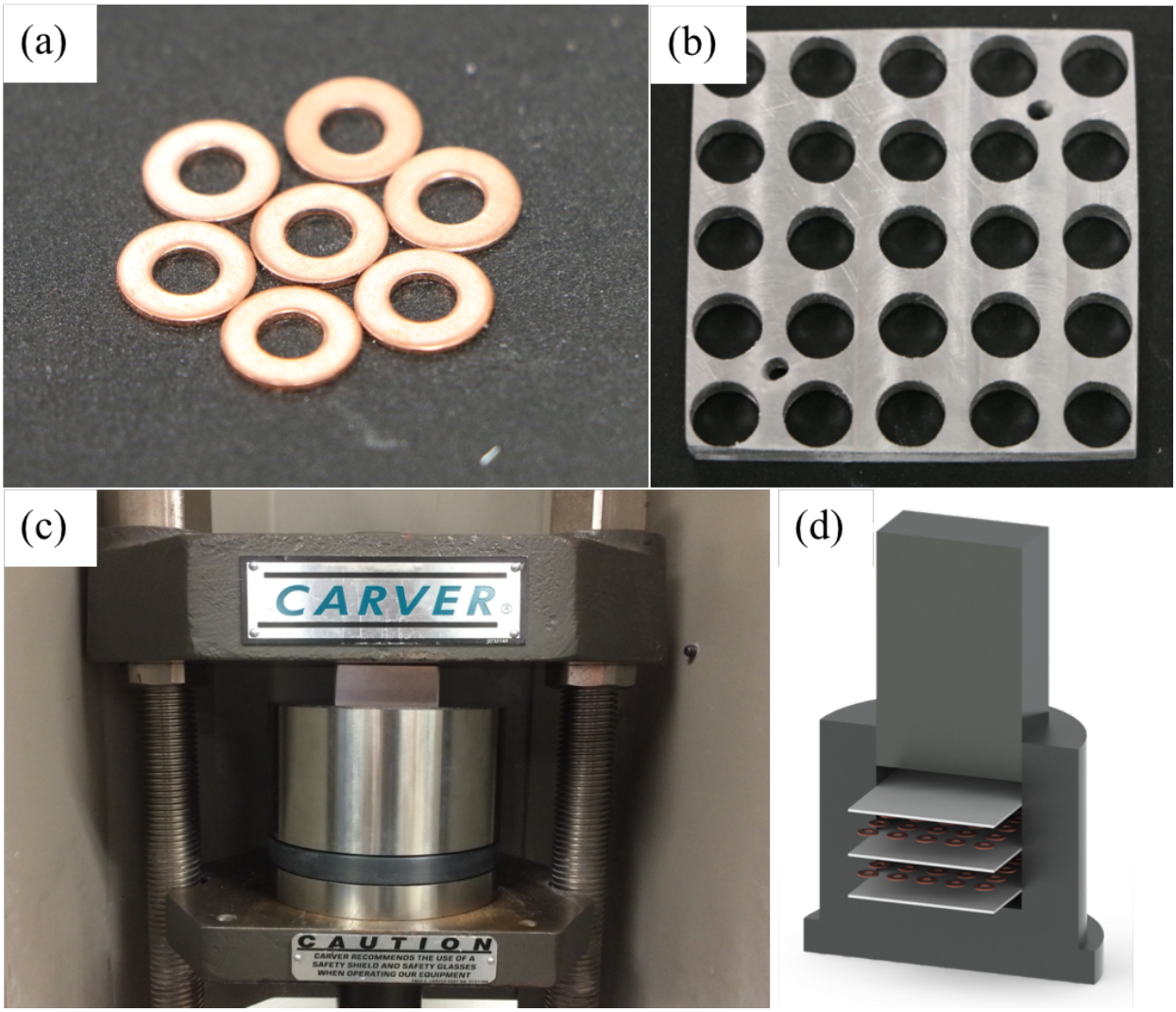


Figure 3.2: (a) Cu washers used for the fabrication, (b) A machined guide was used to insert the washers, the smaller holes in the guide was used to insert two strings for the ease of inserting into and removing from the die, (c) The die placed in the Carver hydraulic press, and (d) A 3D schematic showing the layers of the fabricated sample

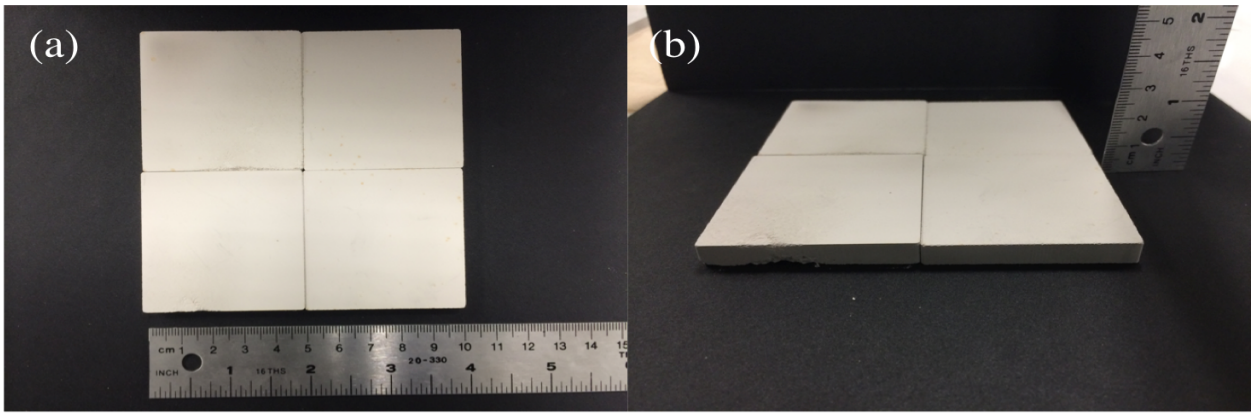


Figure 3.3: Fabricated samples with 70% BN, 30% BTO and 7.5% PVA with Cu washers embedded inside (2" X 2" X 9/32") (a) Top view (b) 3D view

### 3.3.2 Scanning Electron Microscopy (SEM)

Scanning Electron Microscopy (SEM) was carried out to observe the morphology of the raw materials and the materials after the fabrication and heat treatment of the sample. Figure 3.4 shows the SEM images of pure Barium Titanate and BN at different magnifications. The particle size of the BTO and BN powders were ~100 nm and ~800 nm respectively. The SEM of the mixture of BN, BTO and PVA after the fabrication of the sample is shown in Figure 3.5 (a). The sample was then heated at 500 °C for 4h. A very slow heating rate was used (2 °C/min) to avoid any thermal shock to the sample that might produce crack. The SEM image after the sample was heated is shown in Figure 3.5 (b). It can be seen that after the heating the sample became more porous as the binder evaporated. Figure 3.5 (c) and (d) shows the SEM image of a Cu washer at different magnification that are used in the fabrication.

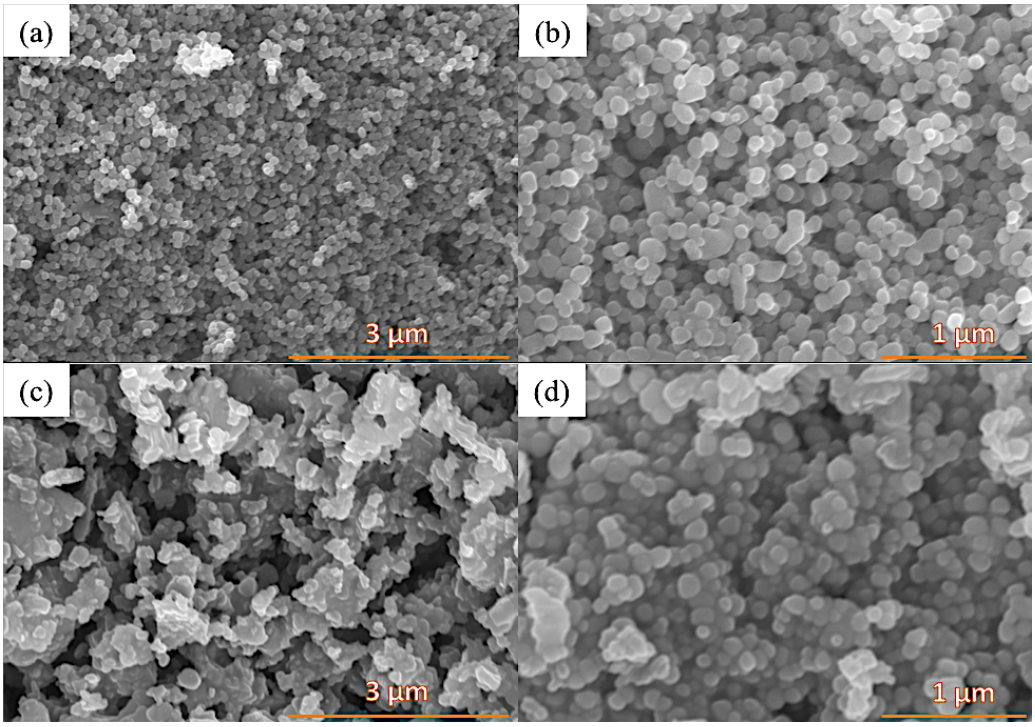


Figure 3.4: SEM images of (a) and (b) Barium Titanate, and (c) and (d) Boron Nitride raw powder

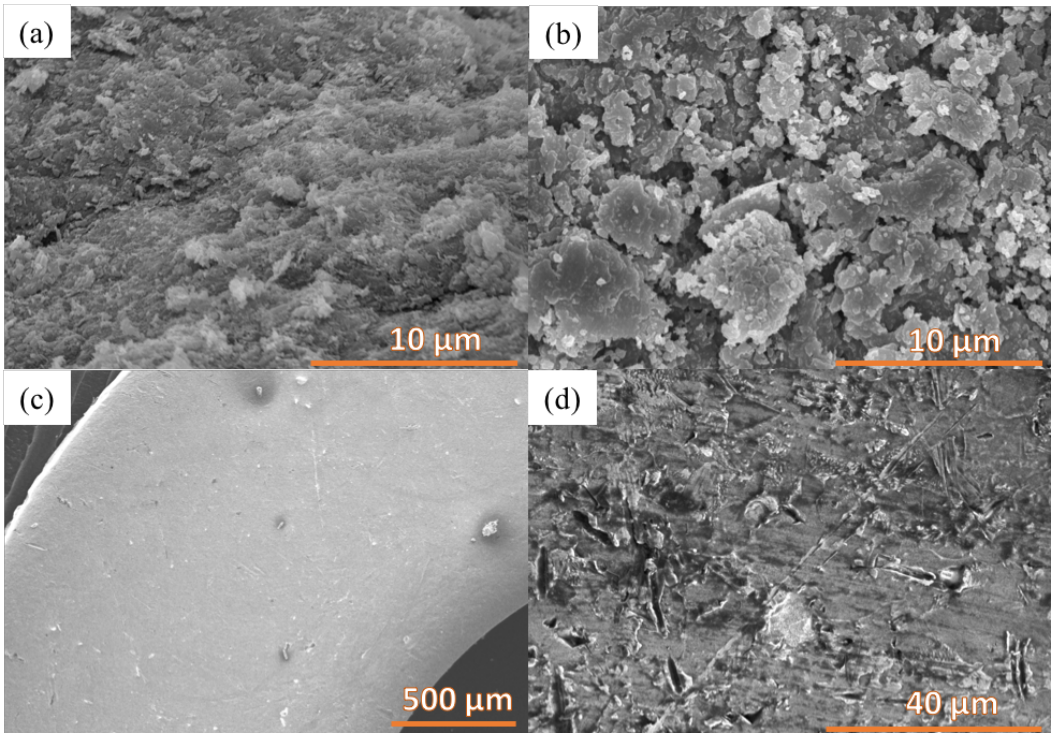


Figure 3.5: SEM images of (a) BN-BTO-PVA sample after fabrication (b) after heating the sample at 500 °C for 4h (c) and (d) Cu washer used in the sensor fabrication

### 3.3.3 X-ray Diffraction (XRD)

X-ray Diffraction (XRD) was carried out to characterize the materials used in the fabrication of the sensor. Figure 3.6 shows the XRD peaks of (a) pure BTO powder, (b) pure BN powder and (c) powders from the fabricated sensor. The peaks of BTO powder were matched with JCPDS (00-005-0626) of Barium Titanate. The most significant plane was (110) at 31.65°. The BN powder peaks matched with JCPDS (00-034-0421) of Boron Nitride. The principle plane was (002) at 26.77°. The fabricated sample shows the presence of peaks from both BTO and BN. Since, PVA is an amorphous material, its presence cannot be identified using XRD.

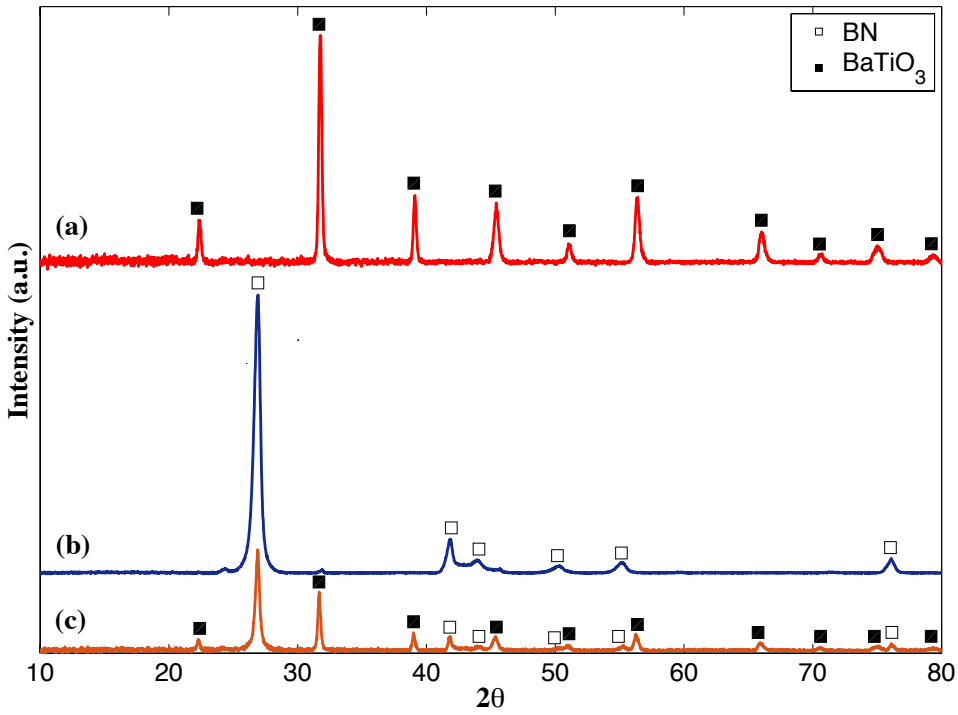


Figure 3.6: XRD spectra of (a) pure $BaTiO_3$ (b) pure BN (c) fabricated sample

### 3.3.4 Characterization of dielectric properties

#### *3.3.3.1 Dielectric property measurement using waveguides*

The relative permittivity and loss properties of the materials were investigated using X-band waveguide (8.2 to 12.4 GHz). The waveguide was connected to an Agilent PNA-X-N5245A network analyzer with the material characterization option 85071E, and the dielectric

properties were calculated from the S-parameters using Tran e fast method, which is suitable for the non-magnetic materials. All the samples were made by powder compression method as described in the fabrication section and later was sanded down to fit the waveguide properly. For BTO and BTO-BN samples, the powders were mixed with 7.5 wt% PVA in order to prevent the breakage of the samples after fabrication; however, it was not required for pure BN samples. The waveguide is shown in Figure 3.7. Figure 3.8, 3.9, and 3.10 shows the relative permittivity and loss properties of BN, BTO-PVA and BN-BTO-PVA respectively. After recording the properties of BTO-PVA and BN-BTO-PVA samples, they were heated at 500 °C for 4h to evaporate the PVA and then were tested again to measure the dielectric properties. Figure 3.11 and 3.12 shows the dielectric properties of BTO and BN-BTO samples after the heating.

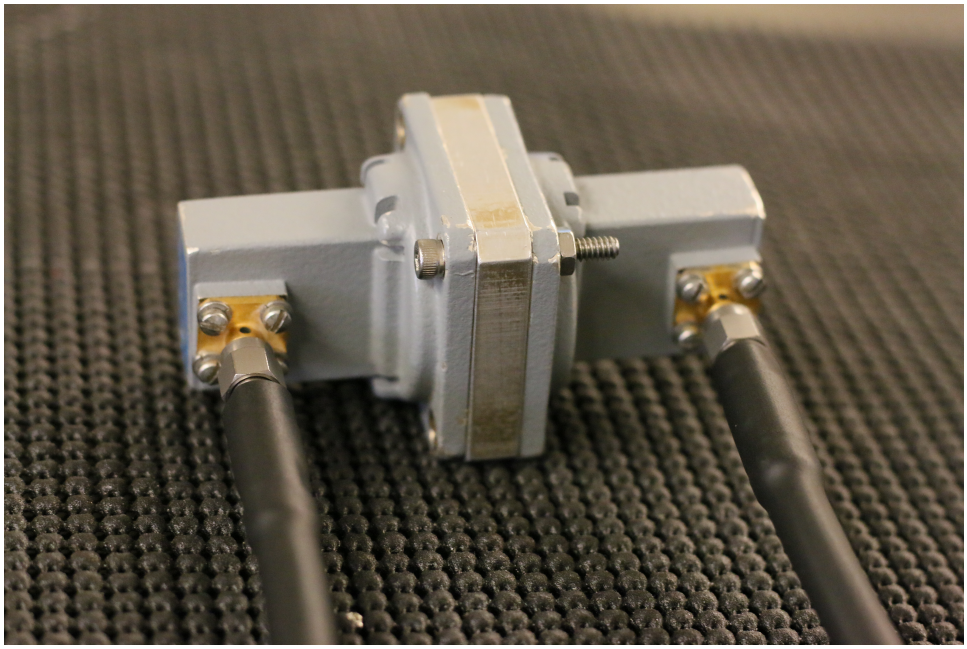

Figure 3.7: Dielectric measurements using waveguide setup. The sample is inside the waveguide, which is connected to the network analyzer

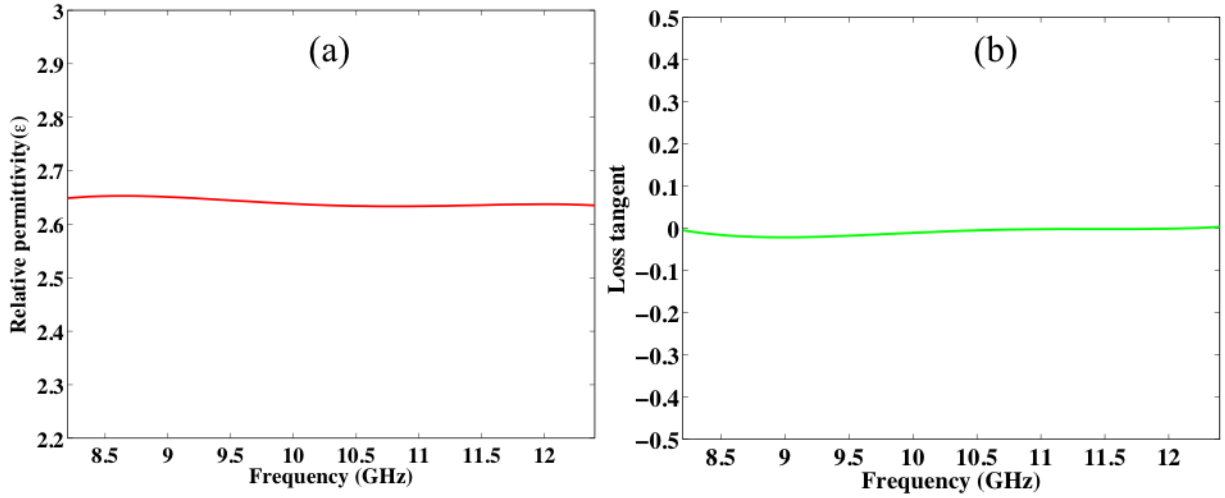


Figure 3.8: (a) Relative permittivity, and (b) Loss tangent of BN measured using X-band waveguide.

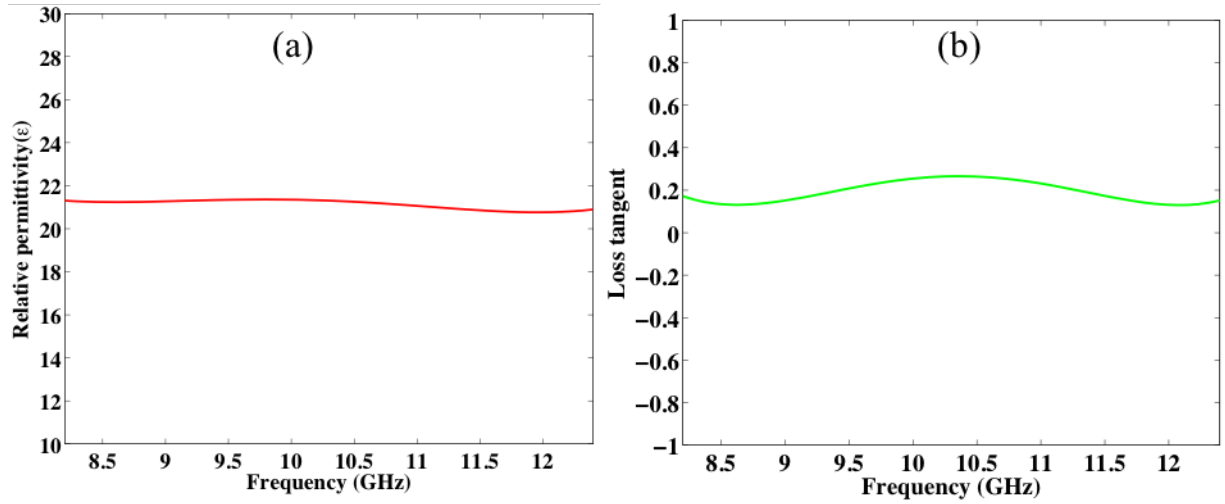


Figure 3.9: (a) Relative permittivity, and (b) Loss tangent of BTO-PVA measured using X-band waveguide.

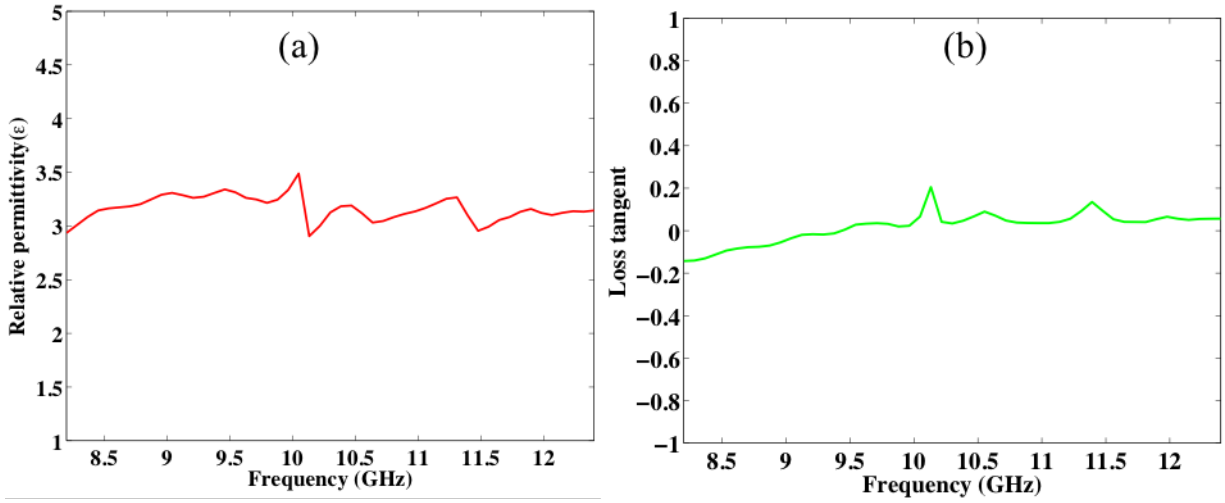


Figure 3.10: (a) Relative permittivity, and (b) Loss tangent of BN-BTO-PVA measured using X-band waveguide.

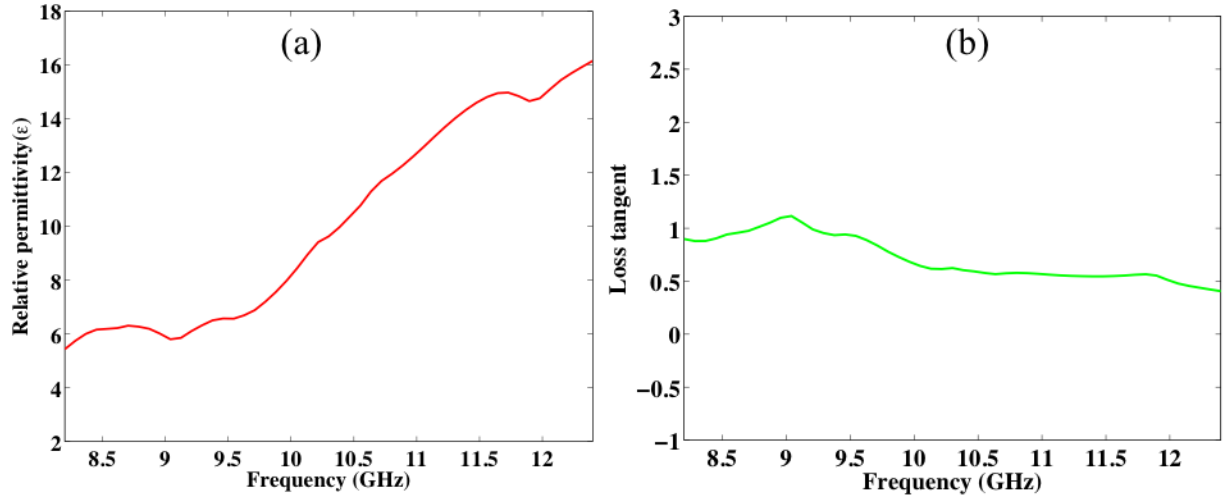


Figure 3.11: (a) Relative permittivity, and (b) Loss tangent of BTO (after heating) measured using X-band waveguide.

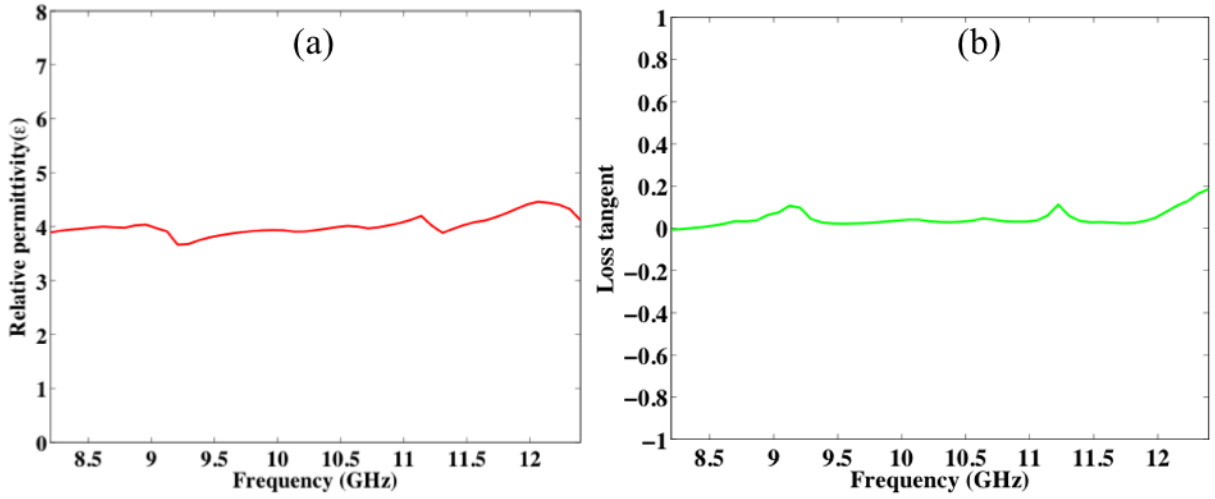


Figure 3.12: (a) Relative permittivity, and (b) Loss tangent of BN-BTO (after heating) measured using X-band waveguide.

### *3.3.3.2 Dielectric property measurement using split cavity resonator*

The Dielectric constant and dielectric loss of the BN-BTO-PVA was also investigated using split cavity resonator. Two different cavity resonator from Damaskos, Inc was used in this purpose, as shown in Figure 3.13. The cylindrical split cavity resonator (125HC thin sheet tester) is suitable for samples with less than 3 mm thickness and with dielectric constants lower than 10. The rectangular split cavity resonator (015 thin sheet tester) is suitable for less than 1.5 mm thick sample also with dielectric constants less than 10. A sample with the same ratio of BN, BTO and PVA with thickness about 2.7 mm was fabricated for this purpose. The relative permittivity and loss tangent of the BN-BTO-PVA as fabricated sample is shown in Figure 3.14 and 3.15, measured by 125HC and 015 thin sheet tester respectively. Similar to the waveguide measurements, the sample was then heated at 500 °C for 4h and then was measured again using the 015 thin sheet tester as shown in Figure 3.16. It should be noted here that unlike waveguide setup the split cavity resonator calculates the dielectric properties at discrete points far apart from each other by identifying the resonance at that particular frequency and comparing that with resonance of air of the same thickness (open cavity). It can be seen from figure 3.14 that the dielectric constant measured by the 125HC thin sheet tester lies below 4 and the lowest value is 1.1, however, for that corresponding value the loss is measured negative, which is probably a

measurement error. The same sample was measured in 015 thin sheet tester and the values calculated by this resonator lies around 4 for the dielectric constant and around 0.014. After the sample was heated, the dielectric constant value increased slightly over 4 and the loss was around 0.01.

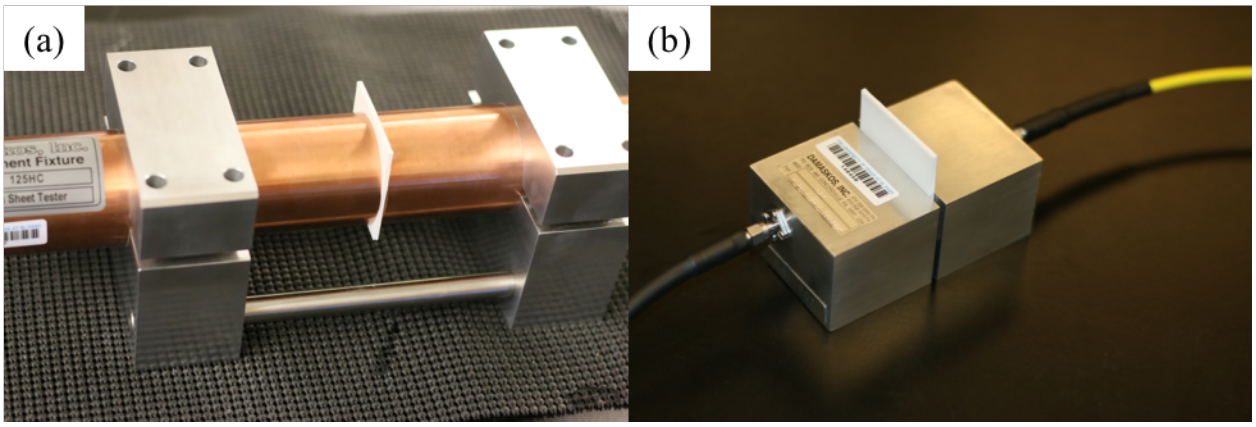


Figure 3.13: Dielectric properties measurement using split cavity resonators (a) 125HC thin sheet tester and (b) 015 thin sheet tester

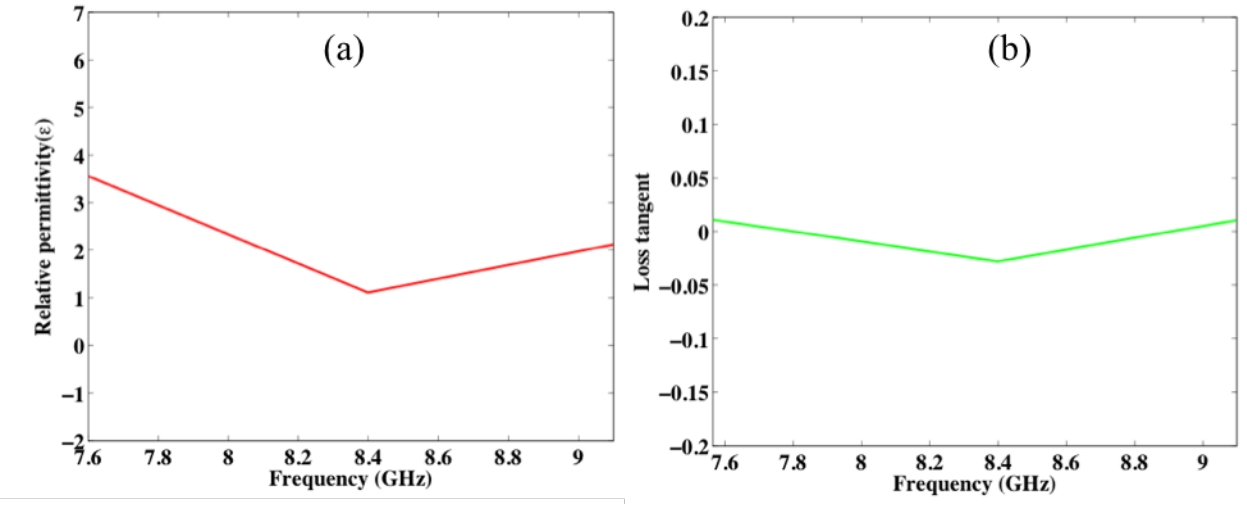


Figure 3.14: (a) Relative permittivity, and (b) Loss tangent of BN-BTO-PVA measured using cylinder cavity resonator.

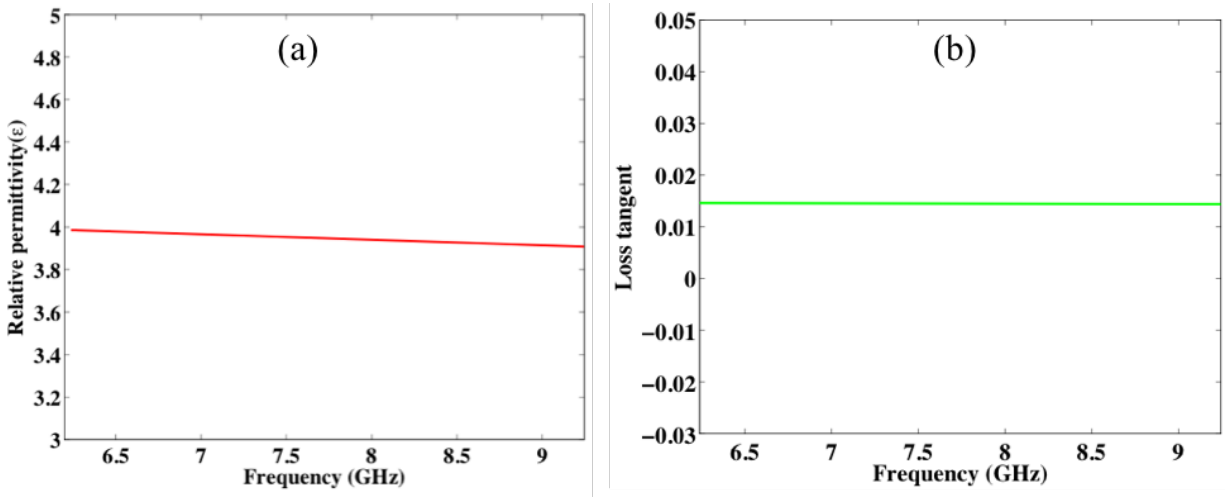


Figure 3.15: (a) Relative permittivity, and (b) Loss tangent of BN-BTO-PVA using rectangular cavity resonator.

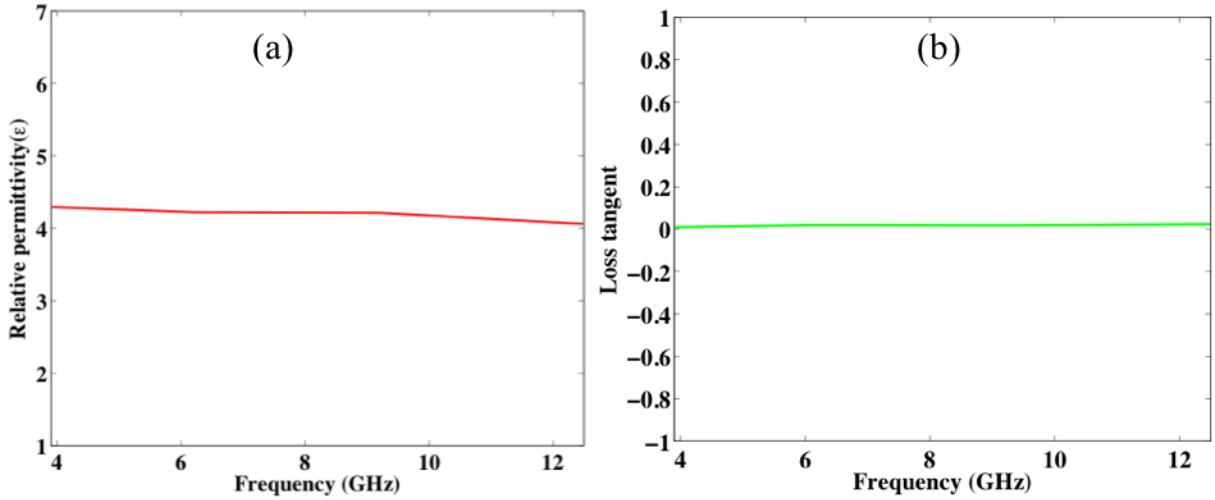


Figure 3.16: (a) Relative permittivity, and (b) Loss tangent of BN-BTO (after heating) measured using rectangular cavity resonator.

As it was found out that the initial predicted dielectric values of the BN-BTO mixture using the Bruggeman mixing method is significantly different than the measured dielectric properties measured using X-band waveguide and cavity resonators, it is necessary to update the simulation to see the resonance of the sensor using these new dielectric parameters. Therefore, the unit cell with the floquet ports simulation was updated with the new values of dieletric constant and loss tangent. Since there is always some experimental uncertainty in the

measurements, all the dielectric constant and corresponding loss values from different tests were used for the simulation and the results are shown in Figure 3.17. The red line corresponds to the measurements for BN-BTO with PVA using X-band waveguide whereas the dark blue line represents the X-band measurement after the PVA burnout. The black line and the cyan line represent the BN-BTO measurement with PVA using the circular and rectangular cavity resonator respectively and the pink line represents the BN-BTO measurement after the PVA burnout using the rectangular cavity measurement. Based on Figure 3.17 it can be seen that the lowest resonance frequency lies slightly over 10 GHz and the highest was in between 14 and 15 GHz and it can be expected that the experimental result will fall within this range.

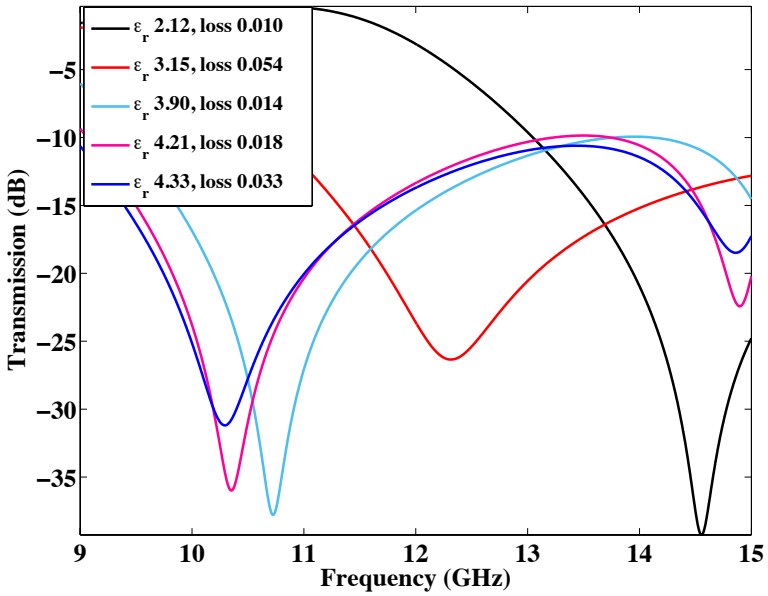


Figure 3.17: Simulation result of the sensor with the dielectric constant and loss values measured by different tests

### 3.4 Experimental setup

The major equipment used for the testing of the sensor are an Agilent E38362B network analyzer and a pair of Gaussian beam poly-rod antenna (MWI lab, Inc). The network analyzer has an operating range from 10 MHz-20 GHz, whereas, the poly-rod antenna is designed to work from 7-18 GHz with a beam size of 2.5" diameter. To facilitate the heating of the sample, a

custom furnace was built using Fiberfrax, which is a very good insulator as well as Microwave transparent. A sample holder was also fabricated using the same material. The experimental setup is shown in Figure 3.18 (a), the sample holder is shown in Figure 3.18 (b) and the sample placed in the sample holder inside the furnace is shown in Figure 3.18 (c). A base was made using Styrofoam, which is also effectively electromagnetically transparent in the microwave range to raise the furnace to the proper height. An assembly was made using 3d printing to make the antenna fixture. The fixture was aligned and fixed with the table to make sure that the alignment is always consistent between the antennas. The assembly was made such a way that the antenna could be rotated horizontally to quantify the effect of the misalignment, which will be discussed in Chapter 4. The antennas were connected to the network analyzer, which was used to generate a frequency sweep and to record the data. Initially, a wider window of operation (7-17 GHz) was chosen to obtain the resonance information and afterwards it was narrowed (9-15 GHz) with 16001 points to obtain higher resolution data. A transmission calibration was performed with the sample holder inside without the sample and then the sample was inserted and the measurements (transmission) were taken.

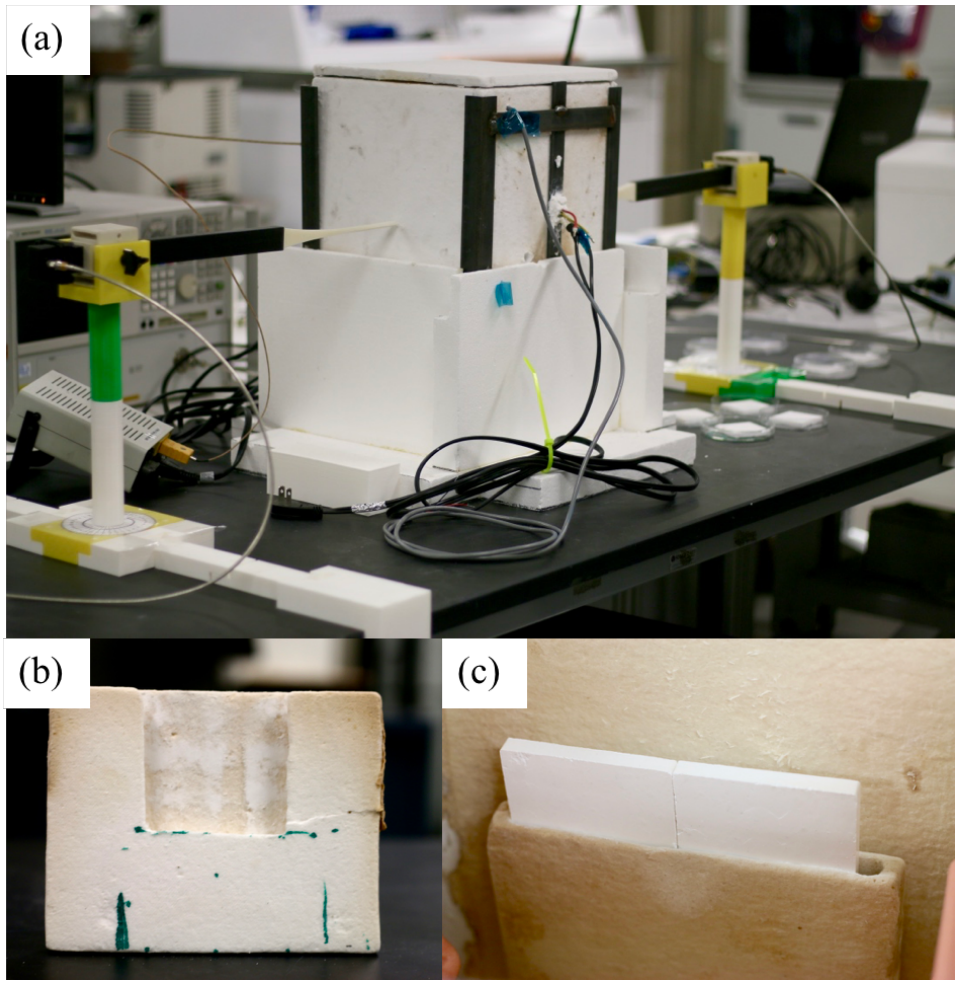


Figure 3.18: (a) Experimental setup showing the furnace, antennas, the network analyzer and temperature controller (b) the fiberfrax sample holder, and (c) samples placed inside the furnace

### 3.5 Results

First, the room temperature response of the sensor was investigated. A time domain gating was used, which is a great tool to reduce the noise from the data and obtain only the signal from the sensor and avoiding the multipath responses. Figure 3.19 shows the time domain response of the sensor. The response without the applied gate is shown in Figure 3.19 (a) and the response after the applied gate at 980 ps is shown in Figure 3.19 (b). The gated result contains only the first significant peak, which corresponds to the wave traveling the shortest distance (i.e. through the sensor) and excludes the response traveled multiple paths (scattered and reflected

from surroundings). Figure 3.20 shows the response of the sensor at room temperature. The log mag transmission response is shown in Figure 3.20 (a) and (b) without the applied gate and with the applied gate respectively. The Resonance frequency from the gated response is around 11.9 GHz. The phase response of the sensor is shown in Figure 3.20 (c) and (d) without the time domain gate and with the gate respectively.

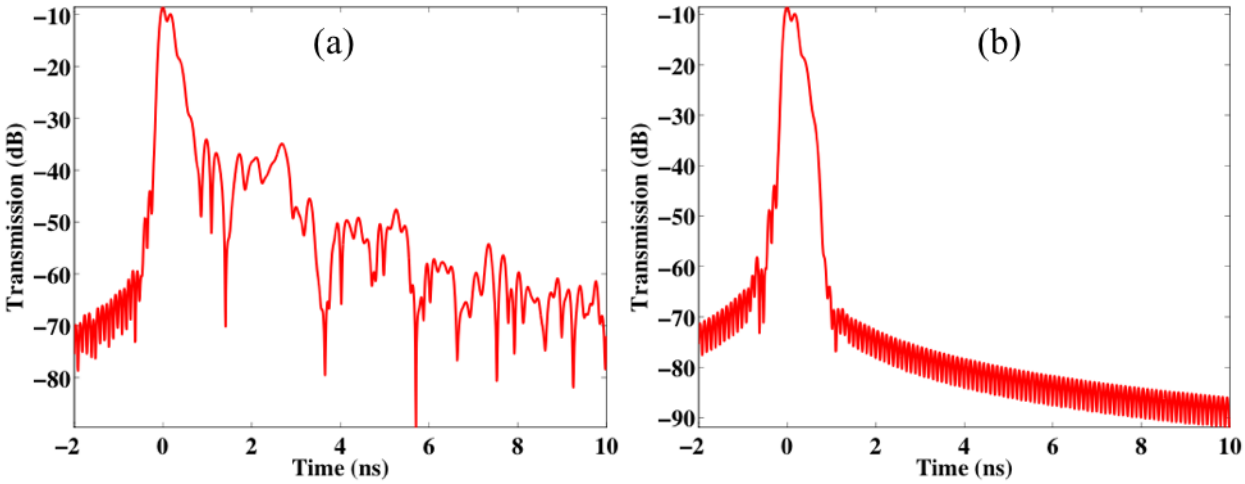


Figure 3.19: Time domain response of the sensor (a) Response without time domain gating applied and (b) gated after the first major peak to only consider the wave that travelled the shortest distance (i.e. through the sample) and avoid the other reflected waves.

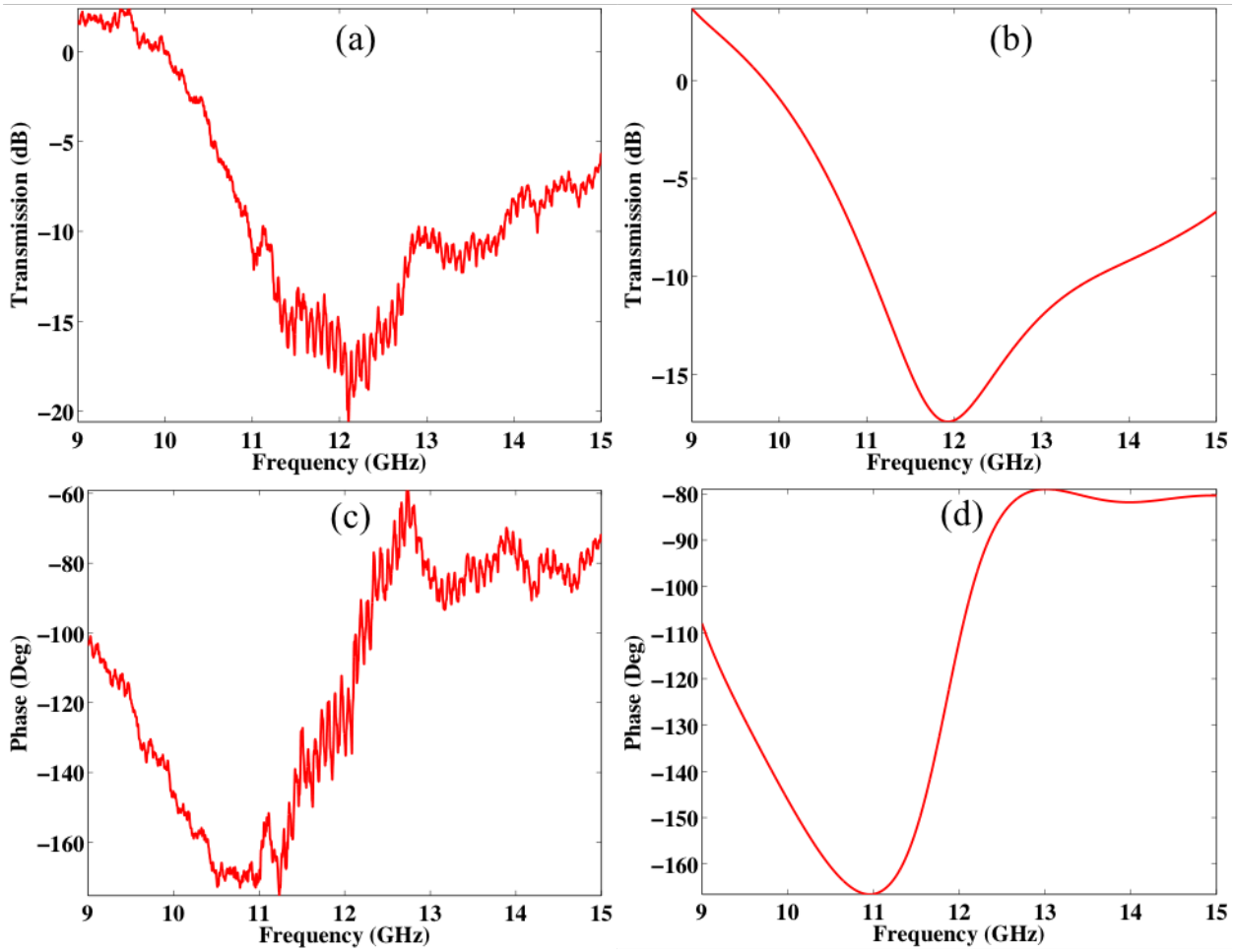


Figure 3.20: Room temperature response of the sensor (a) transmission response without time domain gating (b) transmission response with time domain gating (c) phase without time domain gating, and (d) Phase with time domain gating

After the room temperature response was recorded, the sensor was heated slowly up to 200 °C and the response of the senor was recorded at different temperatures. The temperature response of the sensor is shown in Figure 3.21. The change in resonance frequency of the sensor as a function of temperature for every 10 °C is shown in Figure 3.22. It was observed that for a temperature change from 23 °C to 200 °C, the change in resonance frequency was 81.75 MHz, corresponding to a temperature sensitivity of 0.462 MHz/°C. The tests were then repeated 5 times on different days and with new calibration and the responses are shown in Figure 3.23. It can be seen that for room temperature, the resonance frequency varied from a little over 11.91 GHz to a little over 11.94 GHz and shows a similar trend of shift in resonance frequency for the

change in temperature in all the tests. An average of the resonance frequency at different temperatures from the six tests showed in Figure 3.23 along with the standard deviation at each measurement point is illustrated in Figure 3.24. The maximum standard deviation observed was 0.012 for 200 °C.

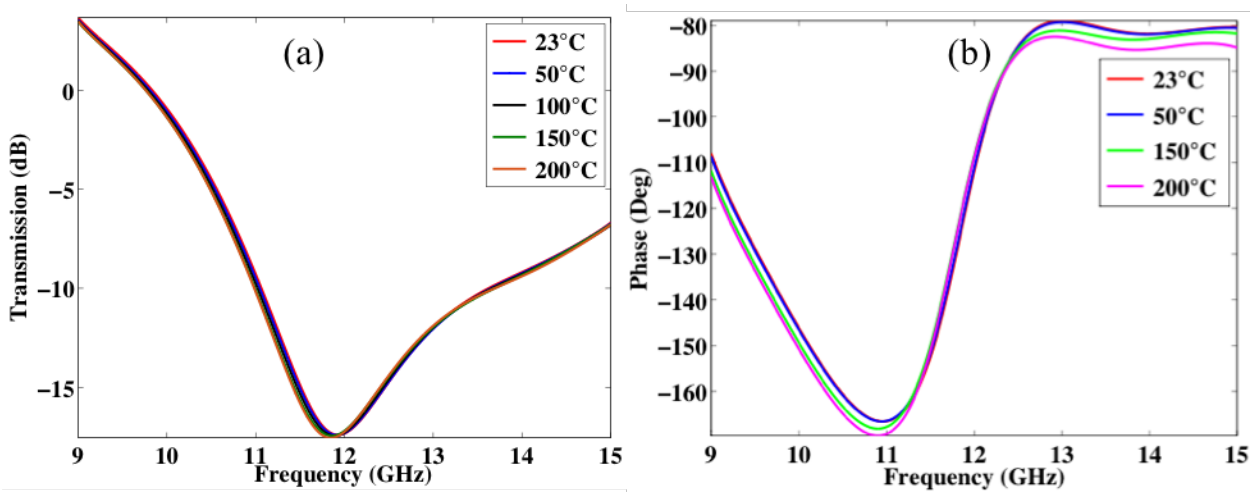


Figure 3.21: Response of the sensor at different temperatures, (a) Transmission response (b) Phase response as a function of frequency

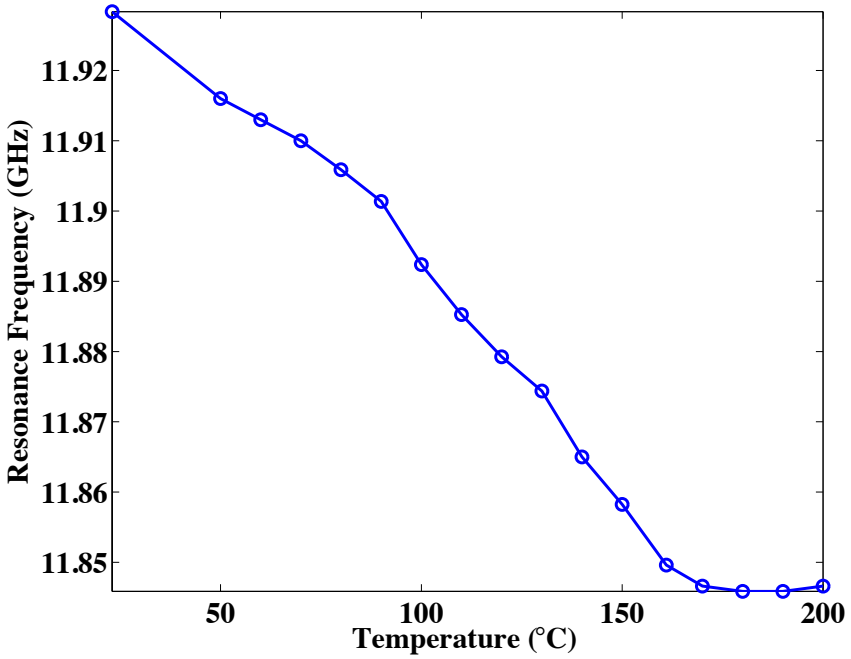


Figure 3.22: Shift of resonance frequency as a function of temperature from room temperature to 200 °C

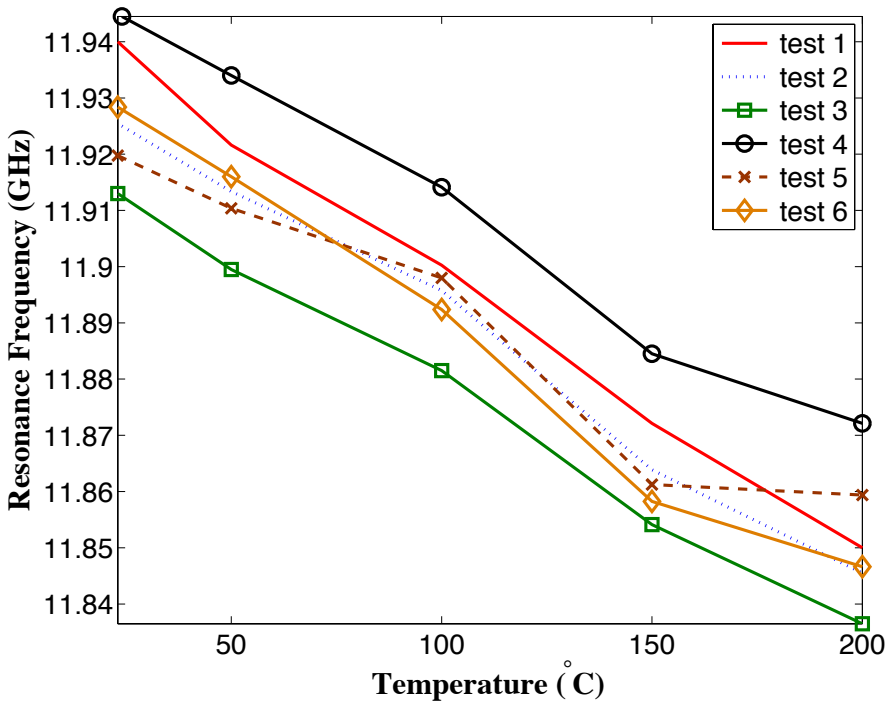


Figure 3.23: Change in resonance frequency of the sensor as a function of temperature for different tests

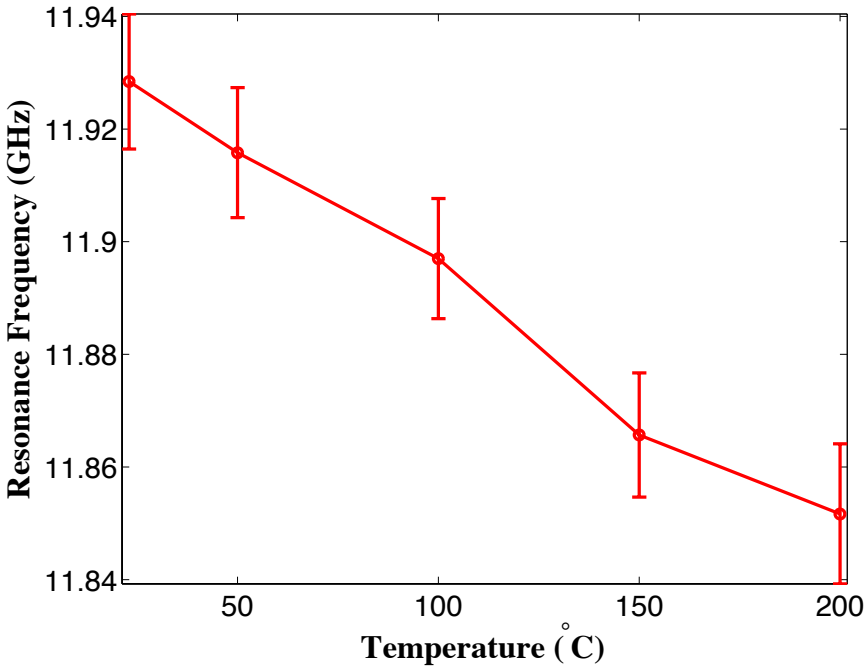


Figure 3.24: Average shift in resonance frequency with change in temperature from 6 tests, with standard deviations displayed as error bars

### 3.5.1 Estimation of dielectric properties by comparing simulation and test results

It can be seen that all the experimental results for the 6-test fall within the range of resonance frequencies predicted by simulation (Figure 3.17). However, none of the measured dielectric property was able to predict the exact resonance frequency at room temperature. Therfore, the average experimental result from the six tests are used to update the simulation to match the result presented in Figure 3.24 and to predict the dielectric constant and loss tangent values corresponding that resonance response.

To evaluate the effect of loss tangent value of the dielectric material on the sensor response, the dielectric constant was fixed at 3.9075, which is the middle value predicted by the dielectric constant measurements (Figure 3.17) and a parametric solution was obtained using HFSS for the loss tangent values starting from 0.01 to 0.1 with 10 equal steps in between as shown in Figure 3.25. It can be inferred from Figure 3.25 that the loss value has significant impact both on the resonance frequency and on the response intensity. The resonance frequency increases with the increase in loss and the intensity of the transmitted signal decreases significantly with the increase of the loss tangent values.

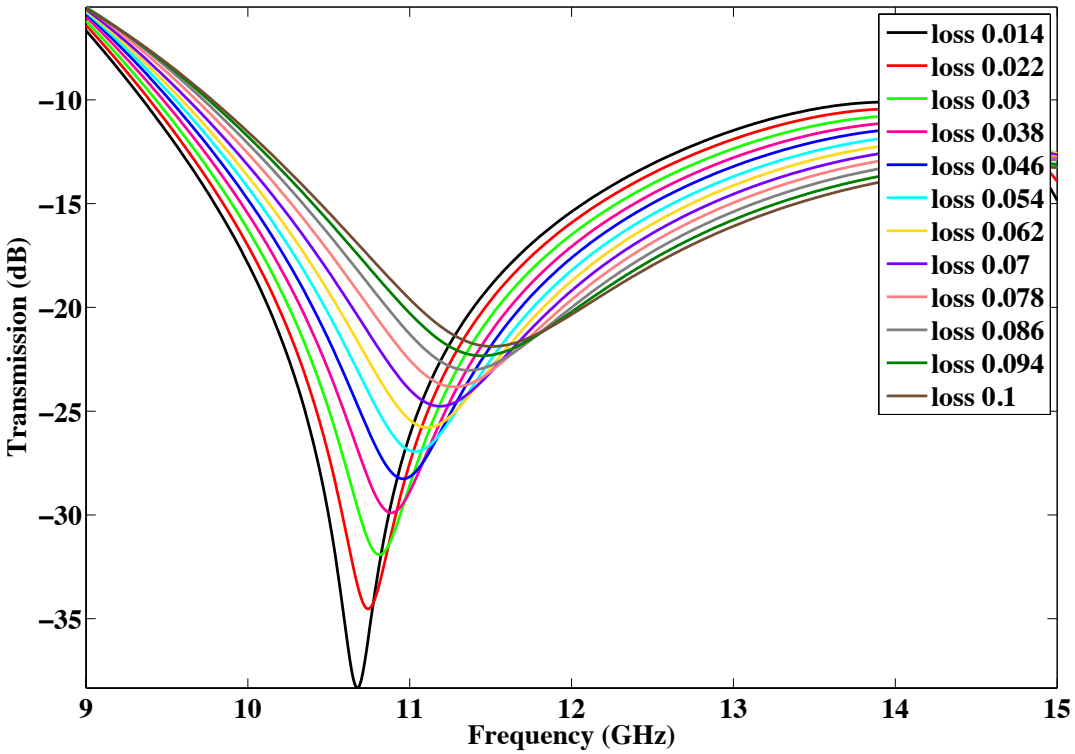


Figure 3.25: Parametric simulation of loss tangent from 0.014 to 1 while the relative permittivity was kept constant at 3.9075

Another characteristic change is observed is the change of bandwidth of the signal. The resonance gets broader with the increase of loss, resulting in a larger bandwidth. Table 3.1 summarizes the resonance frequency and bandwidth change with the increase in loss tangent values. The bandwidth of the resonances at room temperature from test 1-6 was also calculated and the average is about 1.23. Since, the resonance peak of the sensor is very broad as can be seen from Figure 3.15 (stack of temp) and instead FWHM, 75% of the peak height was chosen while calculating the bandwidth. It can be seen from table 3.1 that the closest bandwidth value to the experimental result is 1.24 and the corresponding loss tangent value is 0.054. Hence, this was taken as the potential loss tangent value of the material for future simulations.

**Table 3.2.** Change of bandwidth and resonance frequency with loss tangent values (simulated)

| Loss Parameter | Bandwidth | Frequency (GHz) |
|---|---|---|
| 0.014 | 0.44 | 10.68 |
| 0.022 | 0.61 | 10.74 |
| 0.03 | 0.77 | 10.81 |
| 0.03 | 0.77 | 10.81 |
| 0.038 | 0.93 | 10.89 |
| 0.046 | 1.1 | 10.96 |
| 0.054 | 1.24 | 11.03 |
| 0.062 | 1.42 | 11.11 |
| 0.07 | 1.58 | 11.19 |
| 0.078 | 1.75 | 11.28 |
| 0.086 | 1.93 | 11.37 |
| 0.094 | 2.13 | 11.45 |
| 0.1 | 2.28 | 11.51 |

After the effect of loss tangent was investigated, the effect of change in relative permittivity i.e. dielectric constant was evaluated. For this simulation the loss tangent was kept constant at 0.05426 and a parametric analysis of relative permittivity was carried out from 2.12 to 4.31 dividing the range into 20 steps. The result is illustrated in Figure 3.26. It can be seen that the impact of dielectric constant is mostly on the resonance frequency and it is less significant to the bandwidth or intensity of the signal. The resonance frequency decreases from over 15 GHz to less than 11 GHz as the permittivity increases from 2.12 to 4.31.

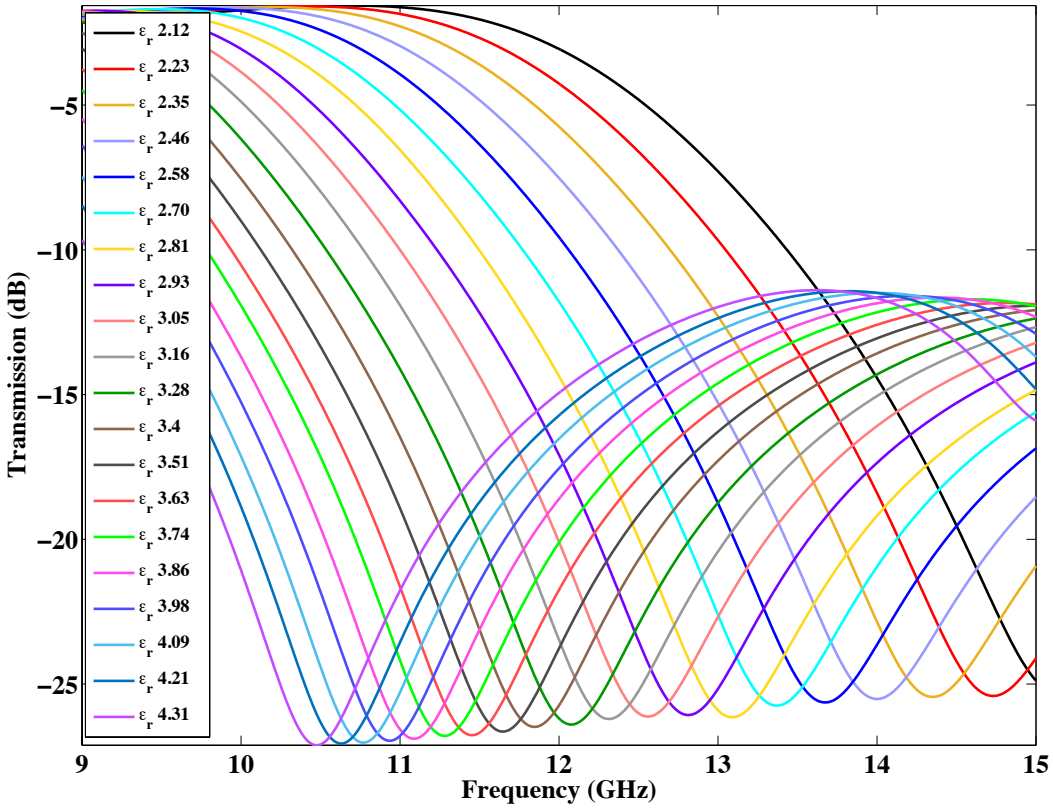


Figure 3.26: Parametric simulation of relative permittivity ranging from 2.12 to 4.31 while the loss tangent value was kept constant at 0.05426.

However, the desired resonance frequency of 11.93 was not achieved as it falls between the resonance frequency obtained for 3.28 and 3.4. To fine-tune the response to be as close as to 11.93 GHz is possible, another parametric simulation was done keeping the loss tangent at its constant value and dividing the dielectric constant from 3.28 to 3.4 into 0.01 increments. The result is shown in Figure 3.27 and it was found that the resonance frequency of 11.93 was obtained for the dielectric constant of 3.36. Hence, it was predicted the room temperature dielectric constant and loos tangent value of the BN-BTO is approximately 3.36 and 0.05426 respectively. After the room temperature dielectric constant was predicted, the average resonance frequency from the experiments was matched with the simulation with the same loss value (0.05426) and corresponding dielectric constant values were found out. Figure 3.28 shows the average resonance frequency of the 6 experiments and the predicted dielectric constants obtained from the simulation for each temperature.

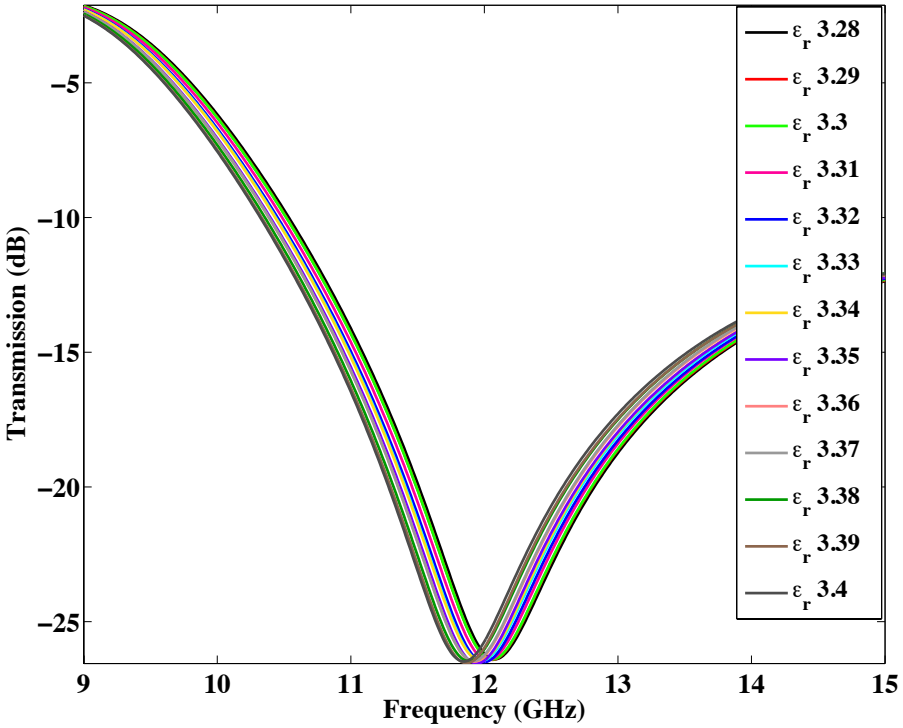


Figure 3.27: Parametric simulation of relative permittivity ranging from 3.28 to 3.4 while the loss tangent value was kept constant at 0.05426.

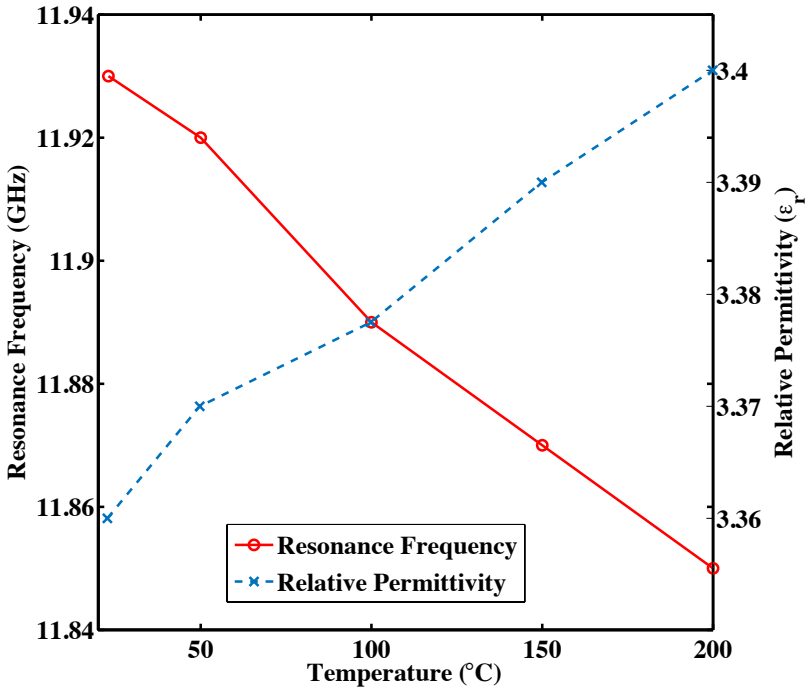


Figure 3.28: Change of resonance frequency (average from 6 tests) and relative permittivity of the corresponding point (simulated) as a function of temperature

# Chapter 4: Investigation of Angle Dependence and Cross-sensitivity of the Sensor

## 4.1 Introduction

In chapter 3 the temperature response of the sensor was investigated from room temperature up to 200 °C and it was seen that the sensor shows a somewhat linear decrease in the resonance frequency as a function of the temperature. The phase of the transmission response also shows a linear change. In this chapter, the effects of three different factors are investigated on the sensor performance to find out its limitations. The three factors are the misalignment between the antennas, humidity and strain. The details of the experimental setup and results will be discussed in the following sections.

## 4.2 Effect of misalignment of antennas on the sensor response

It is expected that the misalignment of the antennas would affect the response of the sensor. However, it is also known that the effect of misalignment is more significant on the reflection parameter that on the transmission spectra. In this experiment, the effect of the misalignment between the antennas on the resonance response of the sensor was investigated. The experimental setup and some components are shown in Figure 4.1. The antennas were first aligned based on the developed fixture by putting both antennas at the 0-degree mark of the printed angle (Figure 4.1(b)).

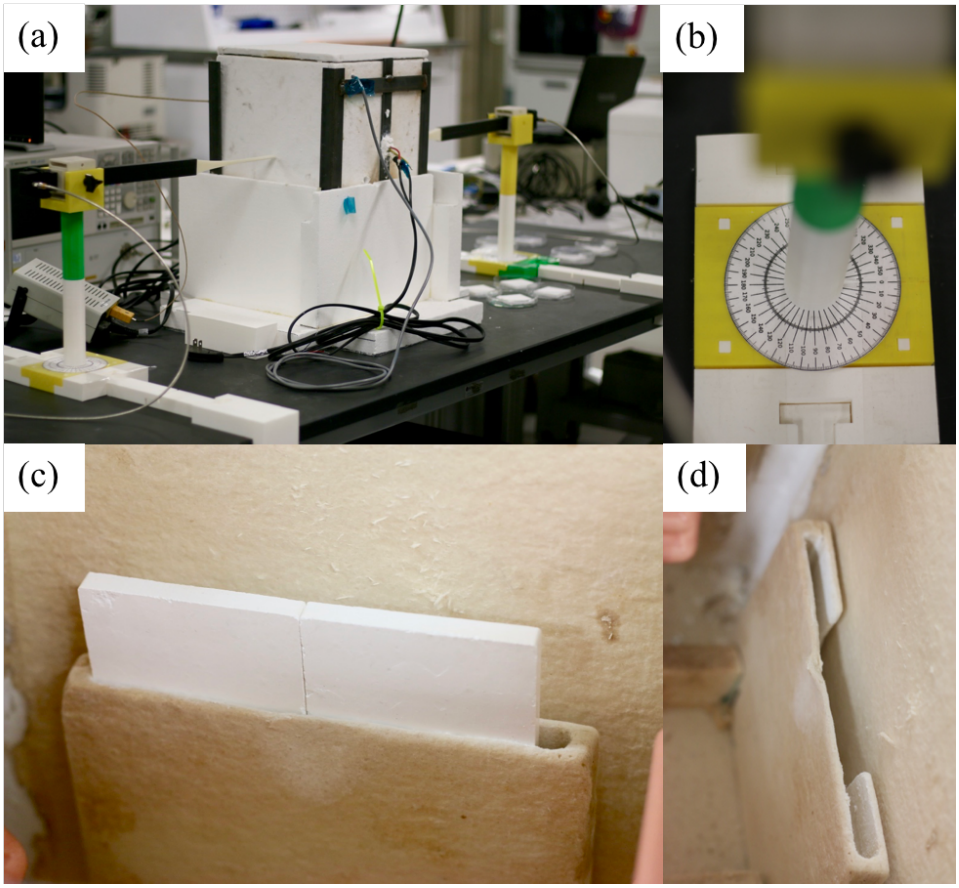


Figure 4.1: (a) Experimental setup of the test (b) the printed angle on the base of the antenna (c) the samples inside the furnace and (d) the empty sample holder inside the furnace

A transmission calibration was then carried out. After that, the sensor was inserted in the sample holder (Figure 4.1 (c)) and the response was recorded at 0-degree. The receiving antenna was then rotated clockwise (considered positive angles for these tests) up to 10 degrees at 1-degree interval with the transmitting antenna fixed at its place. The responses for the sensor for the clockwise rotation of the receiving antenna are shown in Figure 4.2. It can be seen that the resonance frequency decreases somewhat linearly for the first 7 degrees and then the response becomes random. At 10 degrees, the peak gets really broad, which is probably because the antenna is too far away to have any reliable result. The second peak around 14 GHz also seems to get stronger as the misalignment progresses.

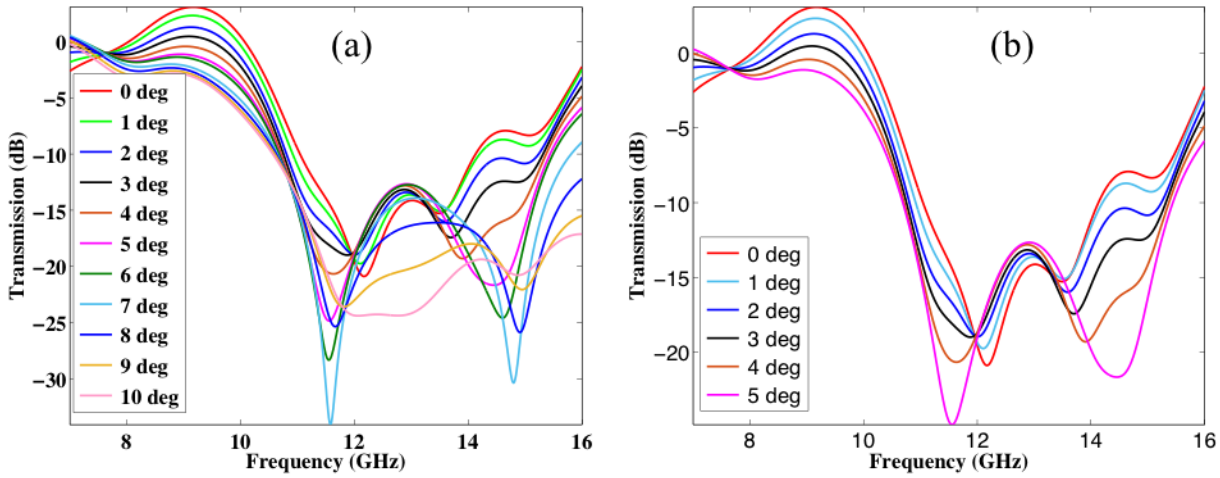


Figure 4.2: Response of the sensor while the receiving antenna is rotated from (a) 0 degree to 10 degree (b) 0 to 5 degree clockwise

After that the receiving antenna was returned to 0-degree and then rotated counter-clockwise (considered negative angles) up to -10 degrees. The responses for the negative angles of the receiving antenna are shown in Figure 4.3. The response seems to follow an opposite trend than the positive angles. The resonance frequency increases till the misalignment of -8 degrees and then starts to decrease. The increase of the second peak around 14 GHz is not as significant as it was for the positive angles. The change of resonance frequency from negative 10 degrees to positive 10 degrees is shown in Figure 4.4.

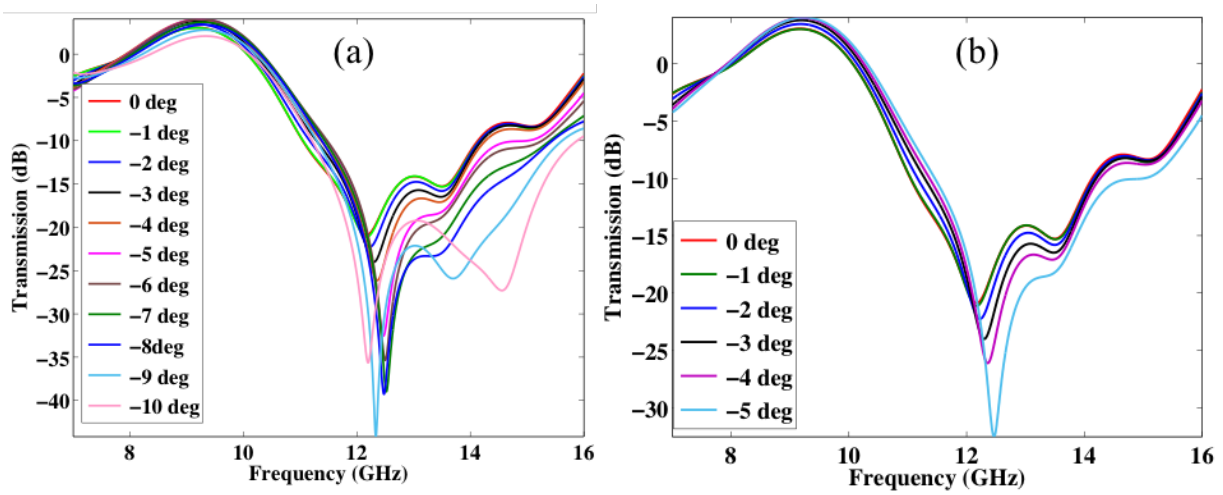


Figure 4.3: Response of the sensor while the receiving antenna is rotated from (a) 0 degree to 10 degree (b) 0 to 5 degree counter-clockwise

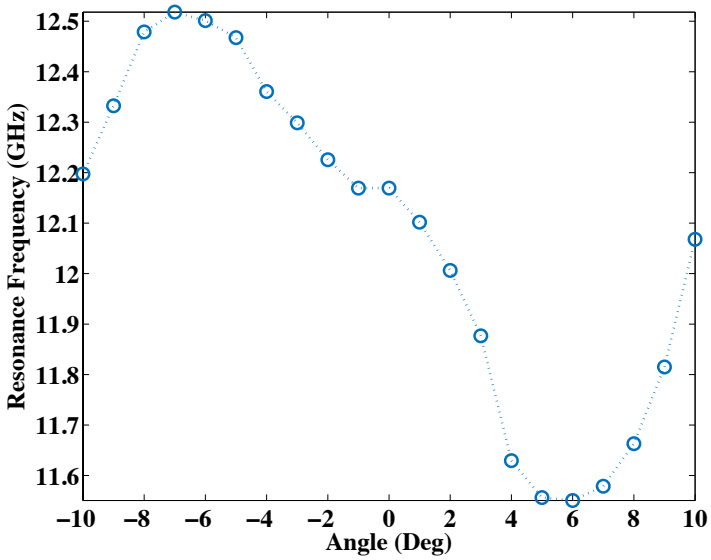


Figure 4.4: Change of Resonance frequency when the angle of the receiving antenna was changed from -10 degree to 10 degrees

Another similar set of tests was carried out by rotating the transmitting antenna while the receiving antenna was fixed. Figure 4.5 shows the response of the sensor with the clockwise rotation of the transmitting antenna. It can be seen that the resonance frequency moved to the right with the increase in angle, however, the intensity of the response increased significantly for up to 3 degrees and decreased afterwards and after 7 degrees, the resonance peak practically disappeared.

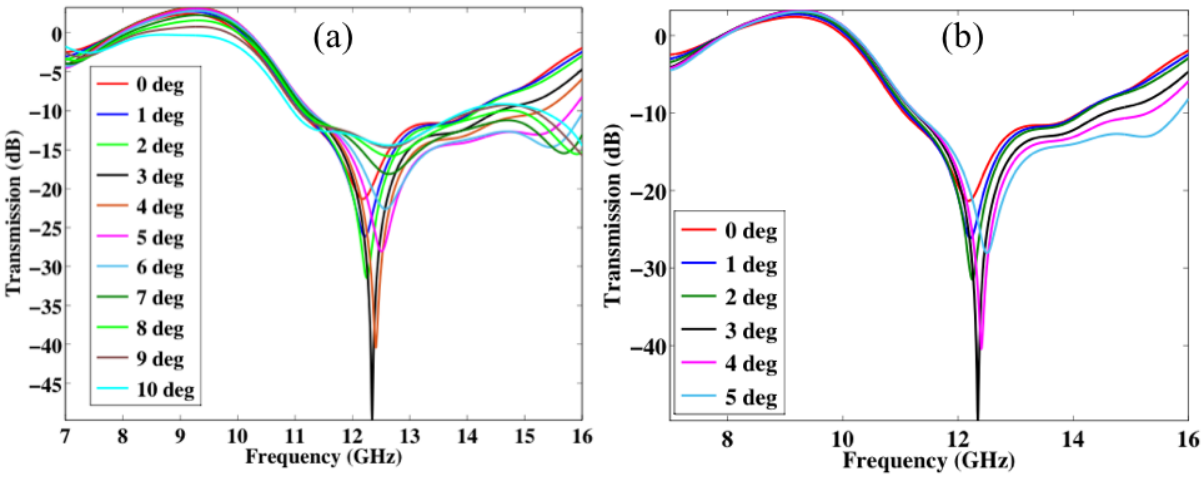


Figure 4.5: Response of the sensor while the transmitting antenna is rotated from (a) 0 degree to 10 degree (b) 0 to 5 degree clockwise

After that the transmitting antenna was brought to 0 degree and then rotated counter-clockwise. The response of the sensor for the counter-clockwise movement of the transmitting antenna is shown in Figure 4.6. It can be seen that similar to the receiving antenna test, the response for the counter-clockwise movement follows an opposite trend than the clockwise movement. The resonance frequency decreases with the increase in negative angles. The intensity of the response decreases up to 3 degrees and then starts increasing.

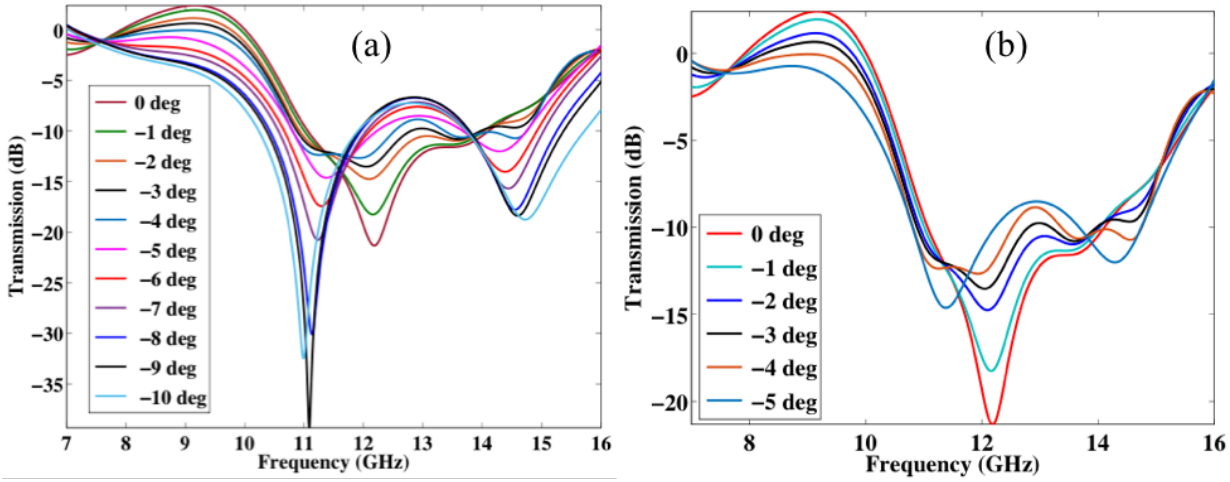


Figure 4.6: Response of the sensor while the transmitting antenna is rotated from (a) 0 degree to 10 degree (b) 0 to 5 degree counter-clockwise

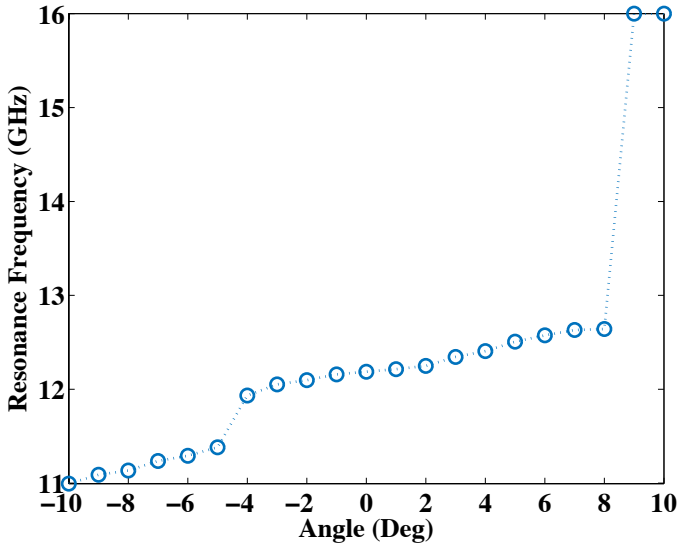


Figure 4.7: Change of Resonance frequency when the angle of the receiving antenna was changed from -10 degree to 10 degrees

The trend of change in resonance frequency with the change in angles from -10 degrees to 10 degrees for the transmitting angle can be observed in Figure 4.7. It can be observed that the resonance frequency increases as the angle changes from -10 to all the way to 10 degrees. After 8 degrees of clockwise rotation, the resonance frequency is practically invisible as shown in Figure 4.5 and the minimum value for the response are around 16 GHz, however, they do not truly represent resonances anymore.

### 4.3 Effect of humidity on the sensor response

The first parameter checked for the cross-sensitivity of the sensor is humidity. It is anticipated that the sensor response would change with the change of humidity in the environment, as the sensor material comprises 70% BN, which is a highly hygroscopic material. Water has significant dielectric properties; a relative permittivity of 58.5 and loss around 0.55 at 11.73 GHz [231], therefore, it is expected the resonance frequency of the sensor would be affected by the presence of water in the environment. To investigate the effect, a humidifier was used to supply a cold steam and the regulator of the humidifier controlled the rate of supply of steam in the fiberfrax chamber. A humidity sensor (Omega Inc., HX-71MA) was also inserted in the furnace to continuously monitor the humidity of the chamber as can be seen from Figure 4.8.

Figure 4.8: Experimental setup for the changing humidity experiment

Since the furnace was not perfectly sealed it was challenging to maintain a constant humidity for long time. A high volume of steam was flown into the chamber for several hours and then it was stopped and measuerement was taken when the humidity settled to a certain value for several several minutes. The environment was very dynamics as during the steam input the humidity sensor displayed as high as 90% humidity and after stopping the flow the humidity level would decrease and get somewhat stable at a lower value. Three tests were carried out and Figure 4.9, 4.10 and 4.11 shows the Transmission spectra and phase response of the sensor while being subjected to humidity change.

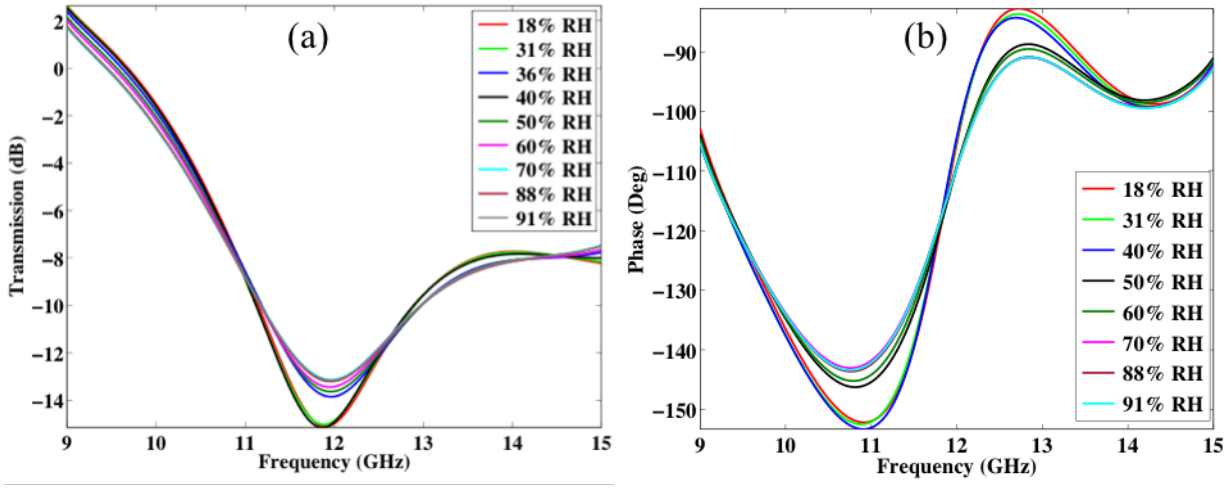


Figure 4.9: Sensor response (a) Transmission (b) Phase at different relative humidity - Test 1

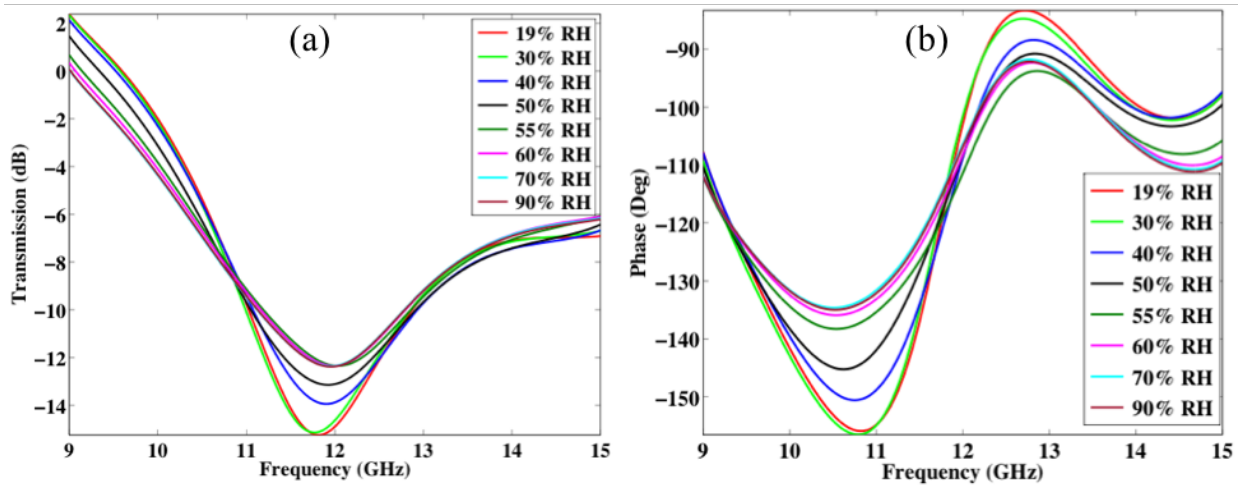


Figure 4.10: Sensor response (a) Transmission (b) Phase at different relative humidity - Test 2

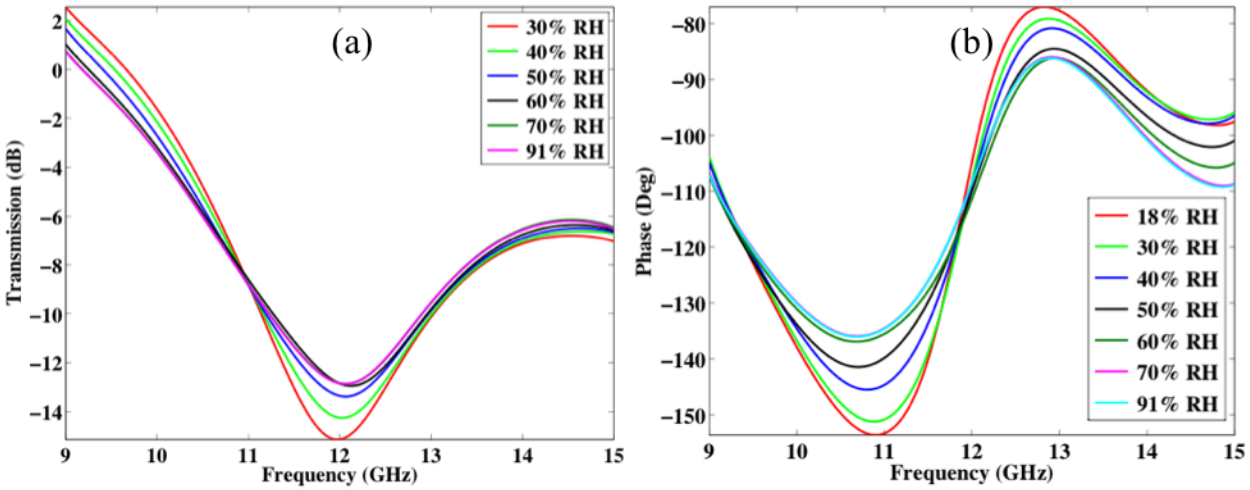


Figure 4.11: Sensor response (a) Transmission (b) Phase at different relative humidity - Test 3

All the tests show quite similar trend in the change of resonance frequency and phase. With the increase of humidity, the resonance frequency increases while the intensity of the response decreases and the resonance peak becomes broader. The decrease in intensity and the increase in bandwidth of the resonance peak could be indication of increasing loss of the sensor as the material absorbs more and more moisture from the environment. Interestingly, the change in phase with the change in humidity is different than with the change in temperature, which was discussed in the previous chapter. Whereas, in case of temperature change the phase shifts linearly, in case of humidity the peak around 11 GHz decreases while the peak around 13 GHz increases in angle. Among the three tests, test 3 was most stable as longer time exposure to humidity was carried out at every point.

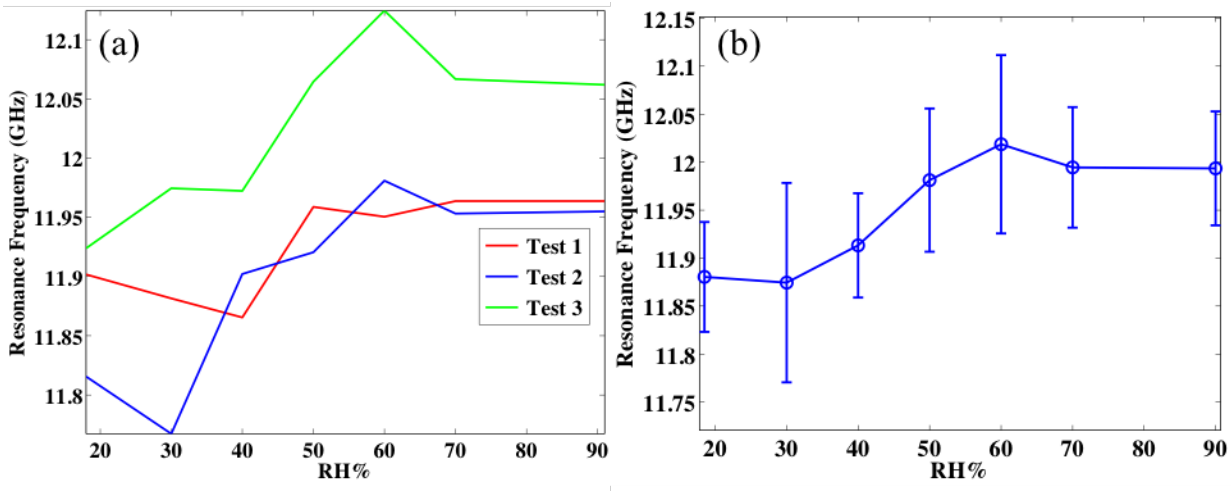


Figure 4.12: Change of resonance frequency of the sensor as a function of relative humidity (a) Test 1, 2, and 3 (b) Average resonance frequency and standard deviation at each point of measurement from the three tests shown in (a)

The change in resonance frequency as a function of relative humidity for the three tests are shown in Figure 4.12 (a). For test 1 and 2 it can be seen that the resonance frequency initially decreases and then starts increasing. However, it was anticipated that this is caused because the sensor did not have enough time to become stable before the test was started. For test 3, the flow of steam was started about 20 minutes after inserting the sample in the furnace and an opposite trend compared to test 1 and test 2 was observed. It can be observed from all the tests that after 70% RH the response of the sensor remains unchanged. By this time the sensor seems to be saturated with moisture and does not absorb any more moisture and the material property remains unchanged. No measurement at 80% RH was taken as it was very difficult to obtain a stable value at that point. Figure 4. 12 (b) shows the average and standard deviation of this three tests. The average resonance frequency increases from 11.88 GHz at 18% RH to 11.99 GHz at 70% and after that remains almost unchanged and the standard deviation ranged from minimum 0.054 at 40% RH to maximum of 0.1 at 30% RH.

### 4.4 Effect of strain on the sensor response

The sensor was next subjected to compressive force and the effect of strain was investigated. The experimental setup is shown in Figure 4.13. The sensor was inserted inside a

custom made fixture with two parts attached to the Admet Mtestquattro testing machine, which was used to apply load on the sensor. Four strain gages (120 ohm, pre-wired, Omega, Inc.) were attached on each of the top right and bottom left sample (two on one side and two on the other) to create a full-bridge circuit and were connected to a portable data acquisition unit (Instrunet i555). Due to the powder nature of the samples and brittleness of the ceramic material, complex surface preparation as generally required for the installation of the strain gauges were not possible and a strain gage adhesive (Omega, Inc.) was applied directly on the surface to install the strain gages. However, it should be noted here that due to very poor bonding of the strain gages to the surface of the sample, two of the strain gages of the bottom-left sample took off during the insertion of the sensor in the compression fixture. Hence, only the strain gages of the top-right sample were connected to the DAQ. However, the surface bonding of these strain gages were also very poor as the adhesive created a very thin polymeric layer which detached from the surface of the sample and no detectable strain was recorded in the DAQ. The strain gages were investigated on different materials and they were performing properly, which confirmed that the no response recorded in the DAQ is due to the fact the load was not transferred to the strain gages due to the poor surface bonding. The strain was hence calculated from the displacement reading of the Admet Mtestquattro software using the following equation,

$$s = \frac{x}{L} \tag{1}$$

where, s is the strain, x is the change in dimension (displacement), and L is the original length of the sample. The compressive length of the sample was 101.6 mm. Two Gaussian beam antennas were placed on each side of the sensor and were mounted on a 3d-printed fixture. The antennas were connected to the network analyzer. The setup with the compression fixture mounted at the home position of the test was first calibrated and the sensor was then inserted into the fixture and the instrument was taken back to the home position. The displacement was created such that the sample was held at a constant displacement at every 0.01 mm increment. The sensor response was recorded using the network analyzer and the load was applied till the next displacement stop point.

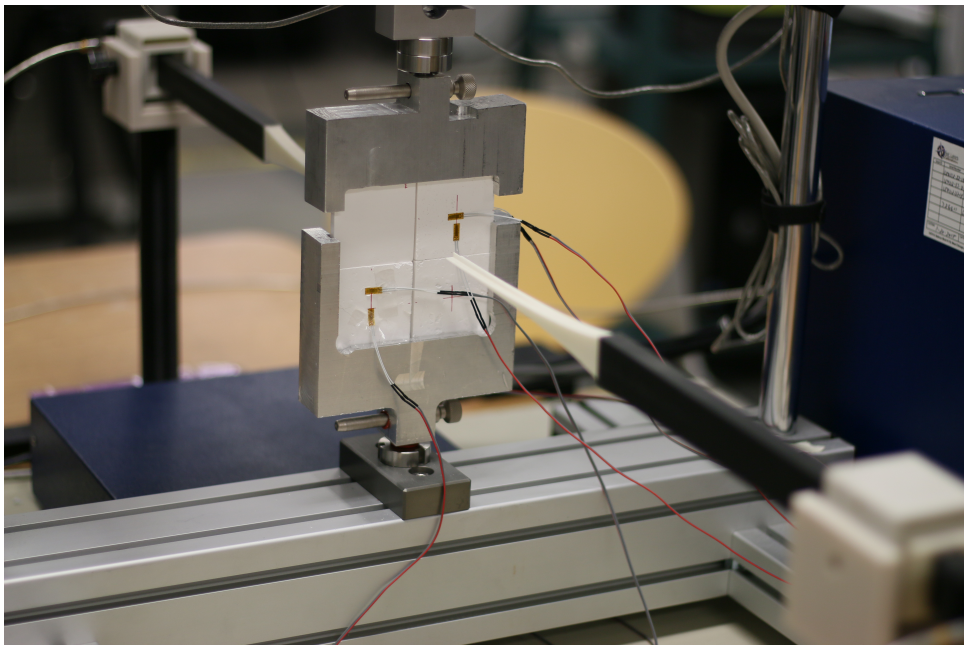

Figure 4.13: Experimental setup for testing the effect of strain on the sensor

Figure 4.14 shows the resonance frequency change of the sensor as a function of displacement (Figure 4.14 (a)) and calculated strain (4.14 (b)). It can be seen that the sensor response does not change significantly below 0.3 mm of displacement. After that, the resonance frequency starts increasing slowly till about 0.8 mm and then starts increasing rapidly until 1.1 mm and then the response become random and as can be seen from Figure 4.15, the response pattern has changed significantly. It should be noted here that the first significant load drop was observed at 0.65 mm, which is correspondent to the initiation of a crack on the sample, the calculated strain at this point is about 6 mstrain. As the crack further propagates throughout the sensor, the response further changes linearly until 1.1 mm displacement, where the corresponding calculated strain is 10.63 mstrain. At 2 mm, the sensor was significantly broken and it can be seen from Figure 4.16 that the interface between the Cu washers and the ceramic is the weakest zone of the samples as samples are broken along that interface.

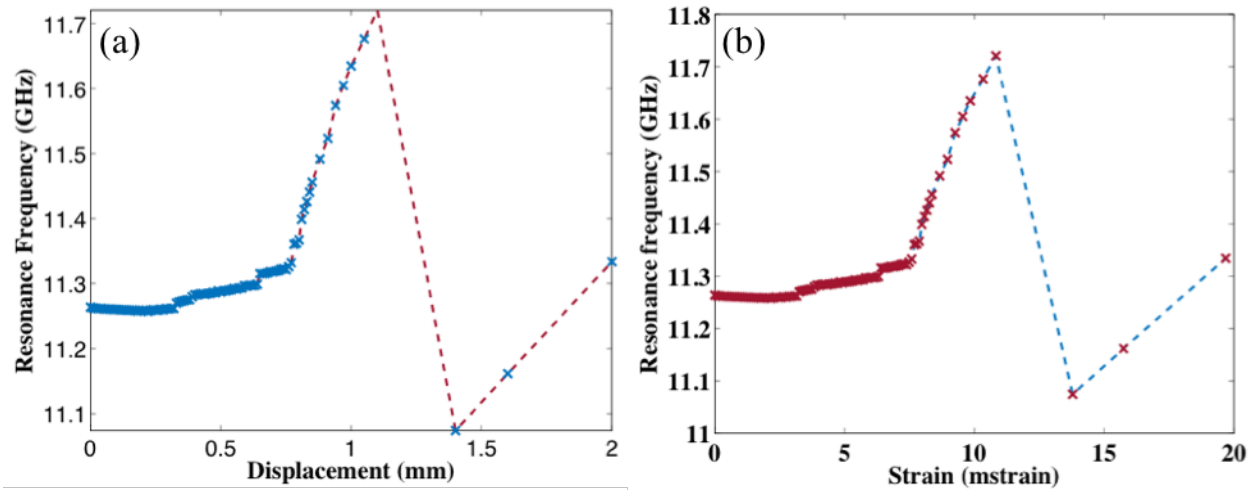


Figure 4.14: Response of the sensor as a function of (a) displacement, (b) calculated strain

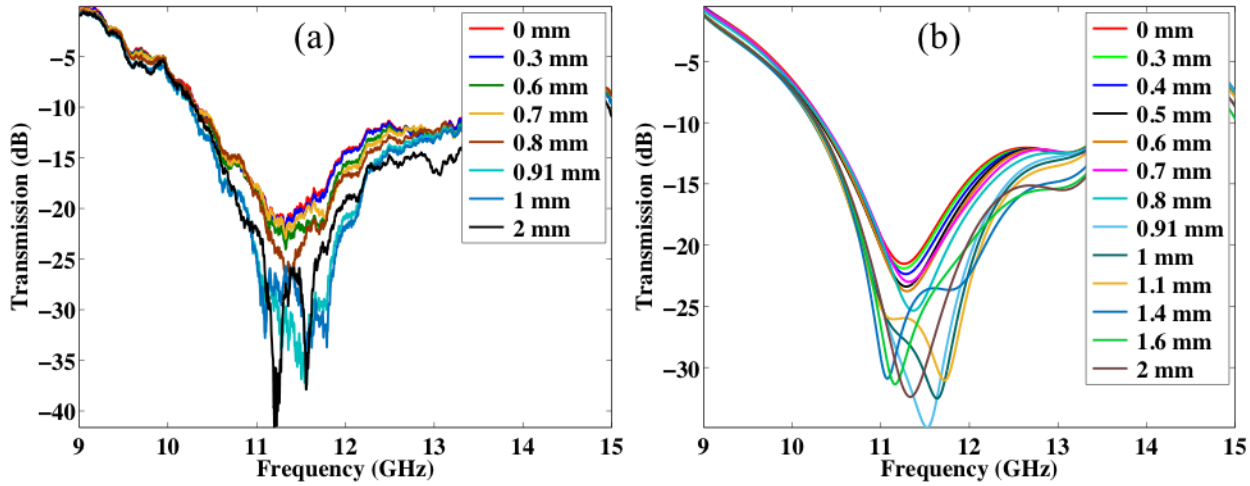


Figure 4.15: The response of the sensor at different displacements (a) raw data (b) time domain gated data

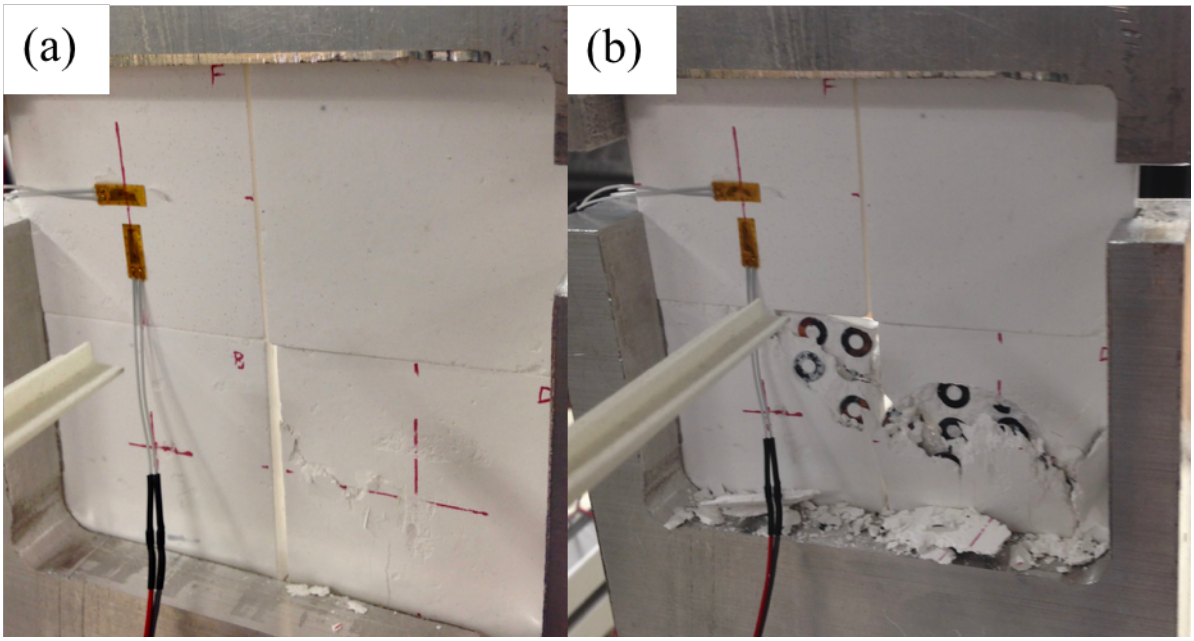


Figure 4.16: Sensor assembly under test (a) crack initiation at the middle of the lower bottom sample (b) samples at the end of the test (broken along the interface between the washers and the powder layers

### 4.5 Conclusion

In this chapter the significance of misalignment in a test setup and the effect of humidity and strain were investigated on the sensor performance. It was found that misalignment of both the transmitting and receiving antenna has impact on the resonance frequency detected by the network analyzer. However, for small misalignment up to 5 degrees the resonance frequency detected should be still reliable after proper calibration and time domain gating as long as there is no change in position of the antennas after the test has started. For misalignment of higher angles, the response could be a combination of reflected and scattered waves that is not truly the response of the sensor.

The sensor response was observed to be affected by the change in humidity in the environment. It was seen that the resonance frequency of the sensor increases as the humidity increases to the point that the material of the sensor has achieved saturation. The author believes that the hygroscopic nature of the material BN, which constitute 70 vol% of the sensor is the

principal reason behind the humidity impact on the sensor and by choosing a different material which is less hygroscopic than BN, the effect can be reduced.

Out of the three factors tested, strain or mechanical deformation of the sensor geometry seems to have the most significant influence on the sensor response. For very small displacements up to 0.3 mm, the sensor response is stable and after that the resonance frequency shifts right gradually until there is a crack initiation and then the response changes rapidly and becomes unreliable. The mechanical strength of the sensor acts as the limitation of this type of ceramic material based sensor and it would not be very suitable for operation in an environment with significant amount of vibration.

# Chapter 5: Feasibility Study of Thermal Energy Harvesting using Lead Free Pyroelectrics

## 5.1 Introduction

The fast increasing demand for electronics that are completely self-powered has triggered an increase in the number of research into energy harvesting materials and devices. With the development of wireless technology sensors [232, 233], electronics [234] can now be placed almost anywhere. However, these wireless components require a power source such as electrochemical batteries [13] or supercapacitors [8, 12]. Both of these devices have a limited storage capacity and are subjected to frequent replacement or charging outside the designated work area. An environmentally friendly energy source to supply power to these devices would be highly convenient, as it would enable continuous operation for longer time without interruption. Numerous investigations have been carried out to obtain potential energy harvesting solutions such as piezoelectric materials [235] and photovoltaics for solar energy [236, 237]. However, the harvested power densities from these natural sources are, in general, low. Thus it is necessary to carry out further investigations to find other materials that have potential to improve the conversion efficiency of energy harvesting devices.

Pyroelectricity has already been proved to be useful in temperature sensing applications [238-240]. However, the output voltage and current from the reported energy harvesters are still on the order of nA [241, 242], making use of these materials difficult for driving commercial electronics. Several approaches were reported using Lead Zirconate Titanate (PZT) as a pyroelectric energy harvesting material. Yang et al. [32] demonstrated a pyroelectric nanogenerator using PZT thin film that drove a LCD display and charged a Li-ion battery. Cuadras et al. [167] reported pyroelectric energy harvesters using screen-printed PZT and charged a 1 μF capacitor to provide power to a sensor node. However, the constant drive for lead free solution to protect the environment necessitates development of new material with comparable properties.

In this chapter, we report LNB as a potential lead free alternative for pyroelectric energy harvesting. A thermoelectric cooler combined with a polarity switching circuit was used to produce an alternative heating and cooling scenario. The current generated as a function of temperature change is recorded for a single sample and stack of samples. The harvesting capability of the material is demonstrated by charging a super-capacitor made with porous carbon-cerium oxide electrodes.

## 5.2 Experimental methodology

### 5.2.1 Pyroelectric wafer

SAW grade, Z-cut LNB wafer (7.62 cm diameter, 0.5 mm thickness) from Precision Micro-Optics LLC was used in the research. The wafer was coated with silver paint (SPI-05002-AB) on both sides to serve as electrodes.

### 5.2.2 Porous Carbon/Cerium oxide nanoparticle (PC-CON) hybrids synthesis

The PC/CON hybrid synthesis is a one-step hydrothermal method. At first 100 mg of porous carbon (ACS Material, LLC) was dispersed in 200 mL of deionized water (DI) water. Then 150 mL of 0.02 M ammonium cerium nitrate $(NH4)_2Ce(NO_3)_6$ was added to the solution and sonicated (Branson Sonifier 450) for 45 minutes. The mixture was then separated by centrifugation. At this stage $Ce(OH)_4$ was formed into the pores and on the surfaces of the porous carbon. Then the product was mixed with 100 mL 5M NaOH solution and transferred into a Teflon lined autoclave. After heating the mixture for 45 hours at 180 °C, the solution was separated by centrifugation and washed with DI water three times. Then the remnant was dried at 70 °C. The product was then heated at 450 °C in Argon for 2 hours [243, 244].

### 5.2.3 Electrode fabrication for supercapacitor

A two-electrode testing setup was prepared using coin cells (CR 2032) as it provides accurate measure for an electrode's performance for electrochemical capacitors [245]. For the fabrication of both PC and PC-CON electrodes, polyvinylidene fluoride (PVDF, MTI corp.,

purity ≥99.5%) was used as binding material. PVDF was dissolved in N-Methyl-2-pyrrolidone (NMP, MTI corp., purity ≥99.5%) at a 1:2.5 weight ratio by heating at 80 °C. Later, 80 wt% active materials and 10 wt% activated carbon were dispersed in 10 wt% PVDF with excess NMP to prepare homogenous slurry using a homogenizer. Then, the slurry was coated on aluminum foil and dried at 100 °C on a hot plate. Finally, a precision disc cutter from MTI Corporation was used to cut anodes with 13 mm diameters, followed by overnight drying in a vacuum oven before the coin cell assembly.

### 5.2.4 Coin cell assembly for supercapacitor

Coin cells (CR 2032) were assembled using PC-CON electrodes inside an argon filled glovebox (Unilab, MBraun). 1 M of Tetraethylammonium Tetrafluoroborate ($TEABF_4$) (Sigma Aldrich) in acetonitrile was prepared inside the glovebox for the electrolyte. Polypropylene membranes (Celgard 2500) were used as separators. Oxygen and moisture levels were kept less than 0.1 ppm inside the glovebox. The schematic of the coin cell assembly is shown in Figure 5.1.

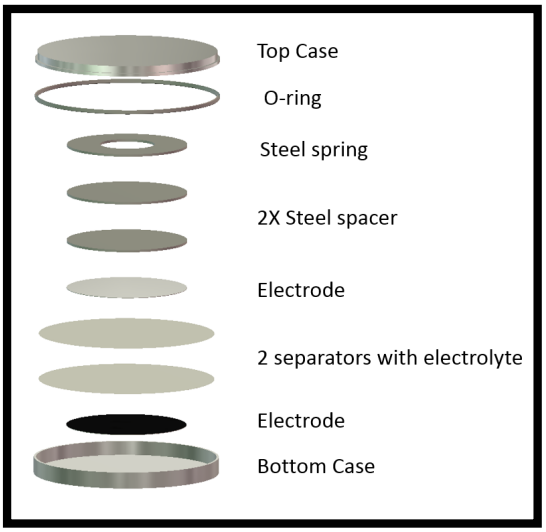


Figure 5.1: Schematic showing exploded view of the coin cell assembly

### 5.3 Material characterization

X-ray Diffraction (XRD) was done using Bruker D8 Discover XRD with Cu Kα radiation to confirm the crystal structure of the LNB wafer. The single sharp peak at 38.98° corresponding to the reflection from the (006) plane [246] on the XRD (Figure 5.2) confirms that the LNB used for this project was a single crystal.

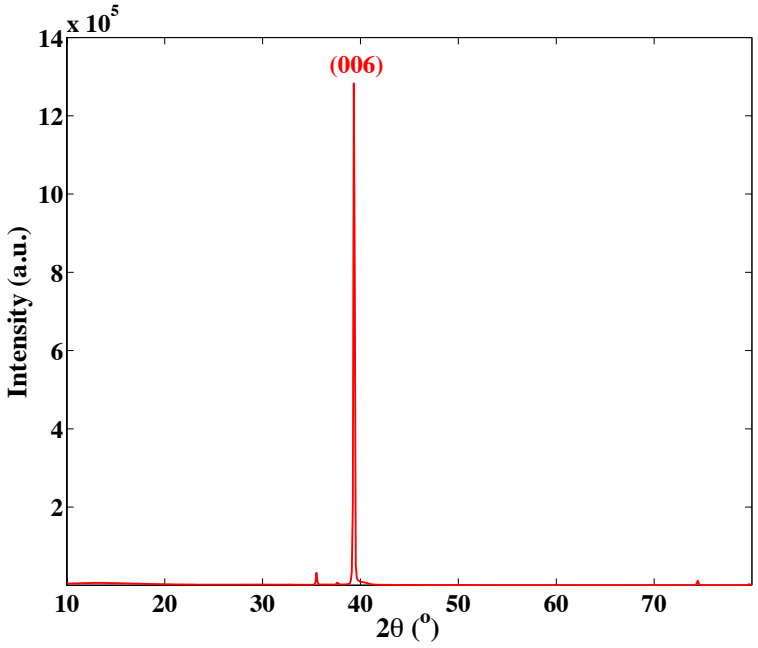


Figure 5.2: XRD of LNB wafer

Scanning Electron Microscopy (SEM) and Transmission Electron Microscopy (TEM) were used to determine the size and morphology of PC-CON hybrids as shown in Figure 5.3. As indicated by the figures, $CeO_2$ particles were formed on the surfaces and nooks of the porous carbon. The nanoparticles had a diameter between 6 to 8 nm. Clear lattice fringes were observed in HRTEM image, which confirms the formation of crystalline particles formed in the hydrothermal reaction. The lattice spacing of 0.31 nm confirms that single crystal $CeO_2$ were synthesized [247]. The capacitance of the capacitor was 0.256 F and 0.224 F at a scan rate of 20 mV/s and 50 mV/s respectively.

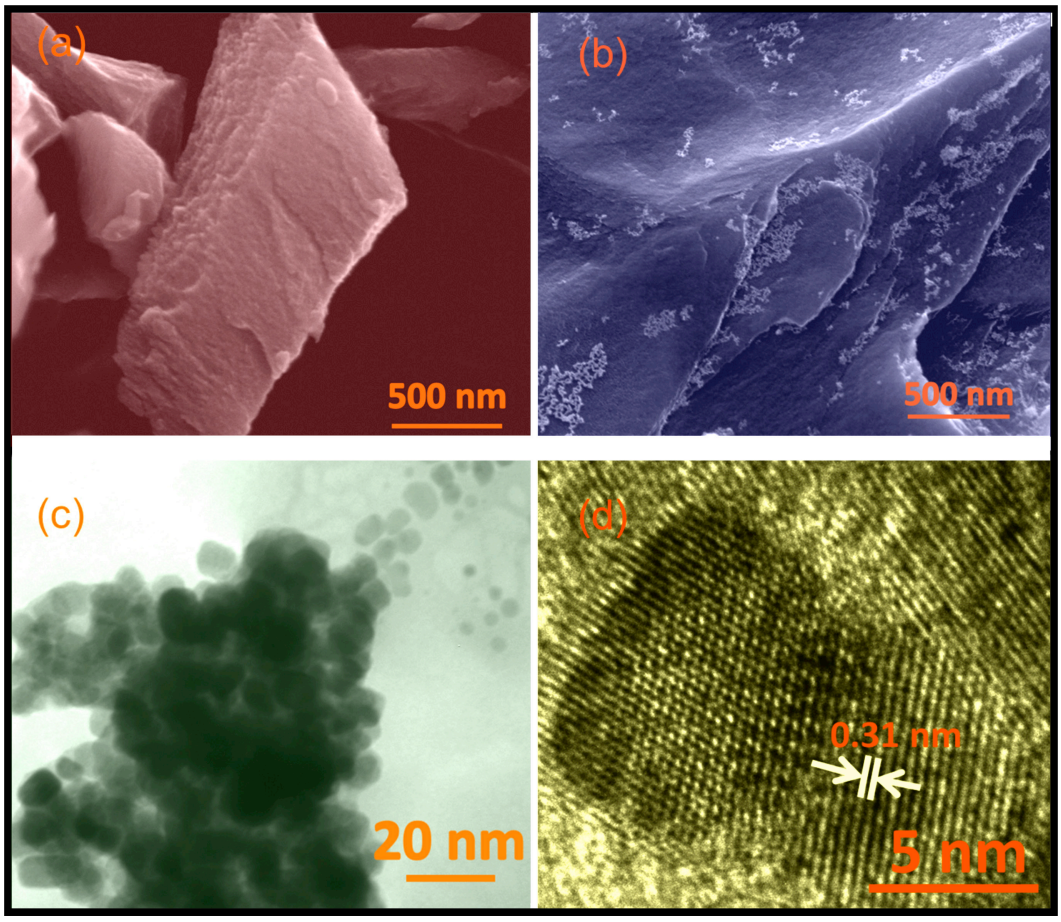


Figure 5.3: (a) SEM image of $CeO_2$ nanoparticles on porous carbon, (b) morphology of porous carbon, (c-d) TEM & HRTEM images of $CeO_2$ nanoparticles

The capacitance, resistance and impedance of the LNB wafer at 1KHz was measured using Hewlett Packard (hp) 4284A precision LCR meter. The material properties are summarized in table 5.1.

**Table 5.1.** Electrical properties of $LiNbO_3$ wafer

| Material | Area ($cm^2$) | Capacitance, $C_P$ (F) | Parallel Resistance, $R_P$ ($\Omega$) | Impedance ($\Omega$) |
|---|---|---|---|---|
| **Lithium Niobate** | 45.6 | $1.65\times10^{-11}$ | $6\times10^{6}$ | $8.2\times10^{6}$ |

The Pyroelectric cells are generally modeled as a current source with a capacitor and a resistor connected in parallel [13] as shown in Figure 5.4.

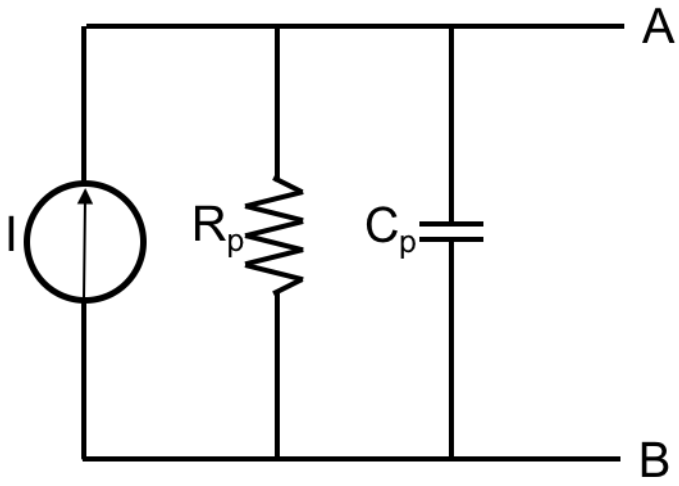


Figure 5.4: Equivalent electrical circuit of the pyroelectric cell

The Equivalent impedance of the circuit,

$$Z_{eq} = R_p \parallel -\frac{j}{\omega C_p} = 6\times10^6 \parallel -\frac{j}{2\pi\times1K\times1.65\times10^{-11}} = 4.33\times10^6 - j2.691\times10^6\ \Omega \qquad (5.1)$$

where, $R_p$ is Parallel Resistance, $C_p$ is Capacitance, $\omega = 2\pi f$ = Angular frequency, and $f$ is the operating frequency, which is 1 KHz for this calculation. If we convert it in a polar co-ordinate system the value of $r$, which is the radial coordinate or radius or magnitude, is $5.09\times10^6$ Ω, which is close to the measured value $8.2\times10^6$ Ω. The equivalent Norton's circuit is given in Figure 5.5.

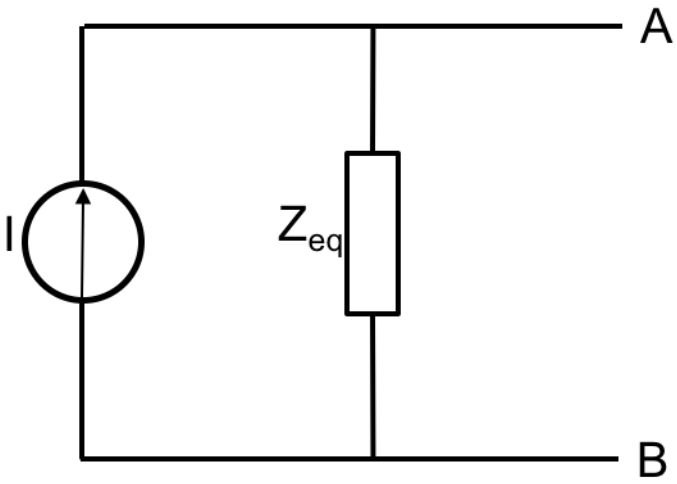


Figure 5.5: Norton equivalent of the pyroelectric sample

**5.4 Experimental setup**

To quantify the energy harvesting capability of LNB, a controlled environment is desired with a controlled alternative heating and cooling cycle. In order to achieve this, the LNB wafer was placed on a thermoelectric cooler (Peltier Inc.). The thermoelectric material creates a temperature difference when a voltage is applied. When a voltage is applied to the thermoelectric cooler, one surface of the thermoelectric block starts heating while other surface cools. If the polarity of the applied voltage is reversed, the effect is reversed and the surface that was heating begins cooling. To achieve an alternating heating and cooling cycle, a DC power supply was connected to the thermoelectric cooler through a polarity reversing circuit with two timers to control the start and stop of the reversing. To quantify the current generated by the LNB wafer, the leads from the sample were connected with a pico-ammeter (Keithley 485) and the output from the pico-ammeter was connected to the data acquisition system. A thermocouple was placed on the top surface of the sample and was connected via an USB interface to a computer to log the data as illustrated in Figure 5.6.

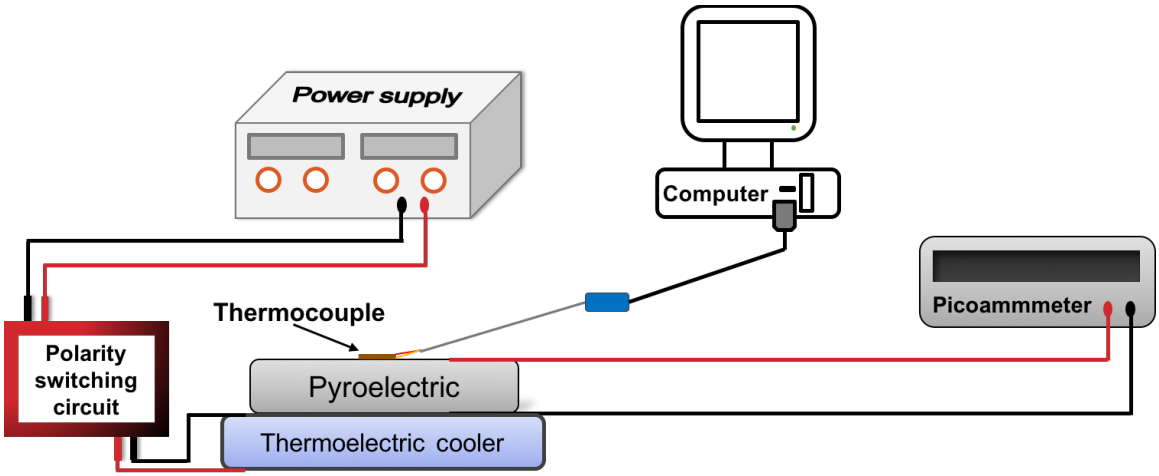


Figure 5.6: Schematic diagram of the setup for pyroelectric current measurement

After quantifying the current, the wafer was connected to the energy harvesting circuit containing a super-capacitor. The super-capacitor was charged from the current generated from the LNB upon heating and cooling. The voltage of the super-capacitor was recorded using a data acquisition system and LabVIEW program. The schematic of the setup is shown in Figure 5.7.

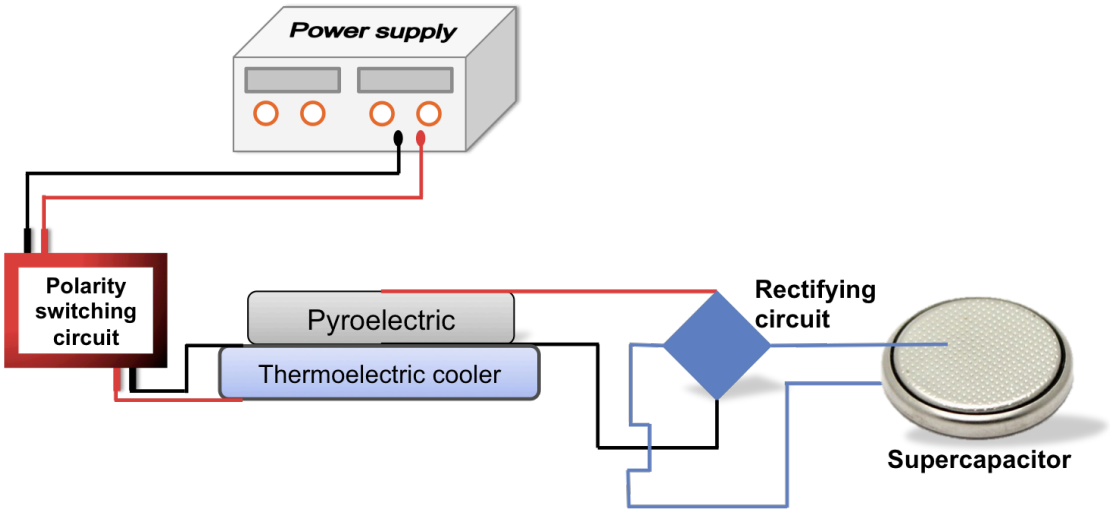


Figure 5.7: Schematic diagram of the pyroelectric energy harvesting setup

The components of the energy harvesting circuit are illustrated in Figure 5.8. The circuit consists of four Schottky rectifying diodes (NTE 573) to form a full wave rectifier circuit to

rectify the alternating current produced from the LNB wafer. A super-capacitor is connected in parallel to the circuit to store the energy utilizing the current through the rectifying circuit. The use of a Schottky diode was aimed to reduce voltage drop in the circuit [248].

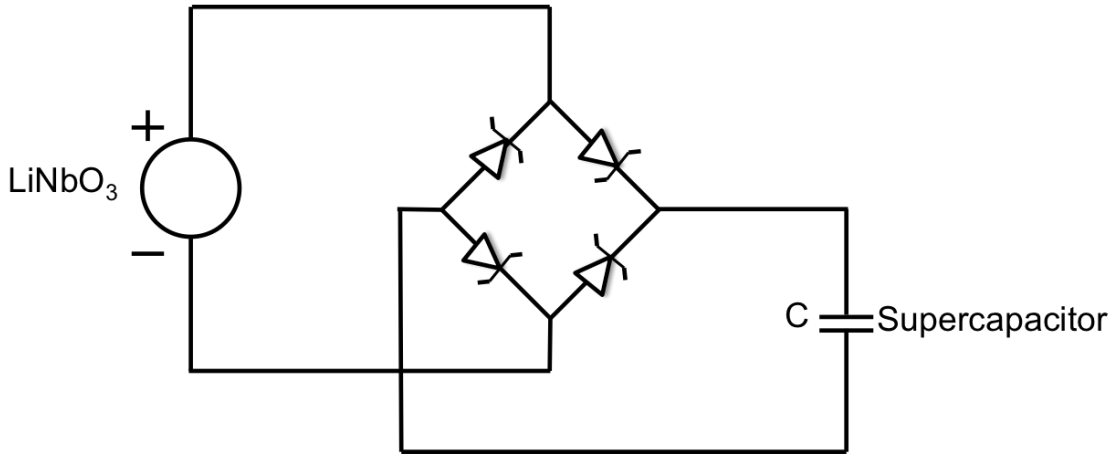


Figure 5.8: Energy harvesting circuit, depicting LNB as a current source, full wave bridge rectifier and a super-capacitor connected in parallel.

**5.5 Results**

Figure 5.9 shows the current generated from a single 3" LNB wafer. The rate of temperature-change with time (dT/dt) that the wafer was subjected to is shown in Figure 5.10. For a peak value of dT/dt at 0.32 °C/s, 380 nA current was generated. The current density observed here for LNB is 8.3 nA/cm$^2$, which is about 20 times lower than the current density of PZT nanogenerator reported in literature [32]. However, the pyroelectric properties of LNB are significantly higher from that of the reported value of other lead free alternatives such as ZnO. The pyroelectric current coefficient *p* of bulk ZnO has been reported to be 0.94 nC/cm$^2$K and for the nanowire it was reported in the range of 1.2~1.5 nC/cm$^2$K [32]. For the LNB wafers tested here, the average pyroelectric coefficient observed was 5-8 nC/cm$^2$K, which is in good agreement with literature [4, 249, 250], which is 4~5 times higher than the reported values for ZnO. For the peak current, the generated open circuit voltage was ~2.6 V, resulting in a peak power of 988 nW.

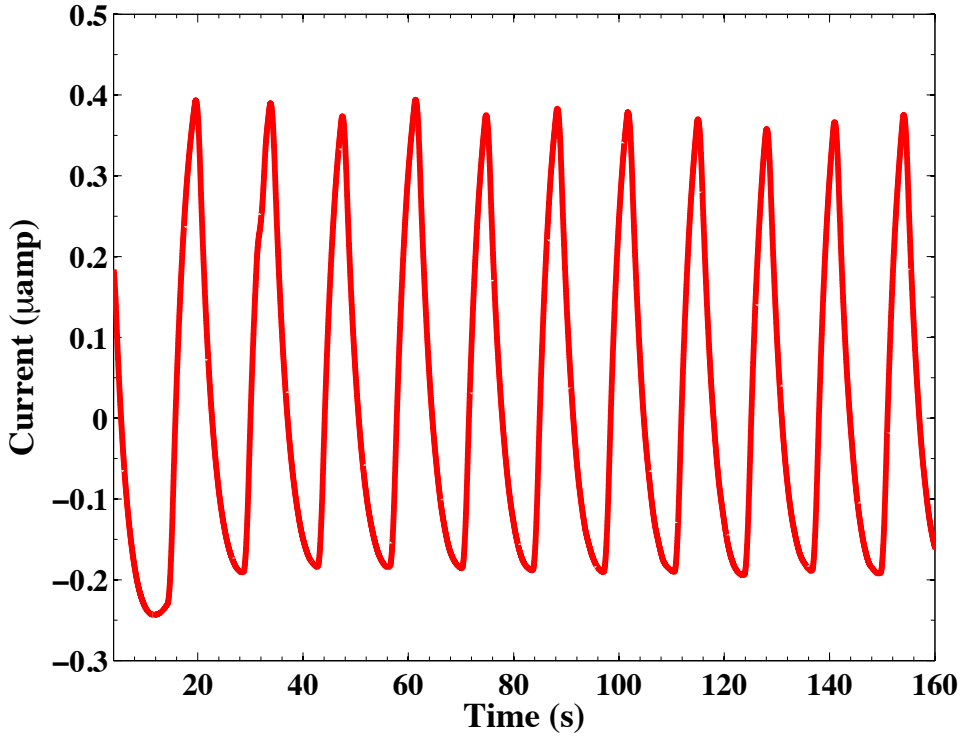


Figure 5.9: Current generated from a LNB wafer

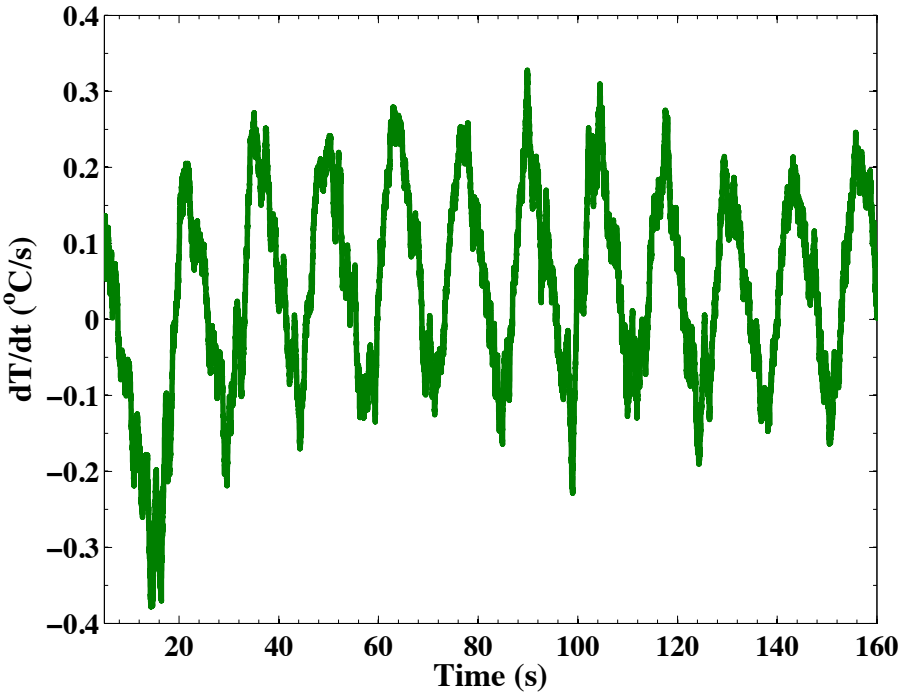


Figure 5.10: Rate of temperature change with time

To quantify the energy harvesting from LNB pyroelectric ceramic, a super-capacitor with the PC-CON electrode was charged and the resulting voltage data vs. time is represented in Figure 5.11. It can be seen that the charging rate is faster at the beginning then slows down and reaches a constant value around 6 mV after 1 hour. The low value of voltage can be attributed to the power drop in rectifying circuit due to the low current generated by the pyroelectric effect.

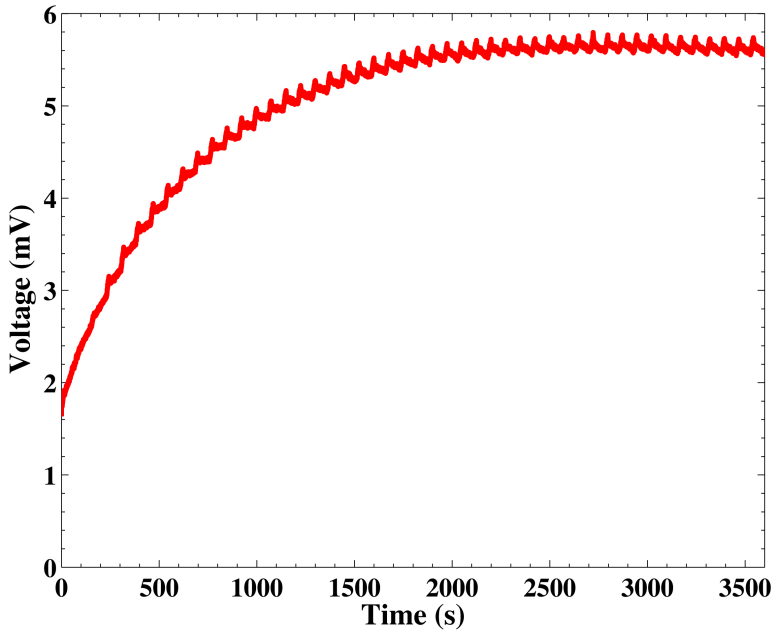


Figure 5.11: PC-CON super-capacitor charging with a single LNB wafer

It was reported in literature that stacking cells in parallel cumulatively adds the current and the voltage generated by the pyroelectric effect [167]. Hence, to further enhance the charging rate, a stacking of three wafers was prepared to increase the generated current and voltage window for charging the super-capacitor. The charging of the super-capacitor was carried out for 2.5 hours and the voltage of the super-capacitor changed from 1 mV to 22 mV during this time period as shown in Figure 5.12. It should be noted here that the super-capacitor did not reach the maximum limited voltage. The super-capacitor could reach higher voltage values if it was charged for a longer period of time. It can be seen from the figure that the charging was faster initially and then slowed down. However, the charge did not reach the stage of saturation. Figure

5.12 (b) shows the charging profile for a short time window. It is important to note that while the increase of the voltage window was observed by stacking the samples, a significant increase in the current generated by the sample was not observed. This phenomenon could be attributed to the fact that in the experimental setup, the temperature change is being driven by conduction heat transfer from the bottom of the sample stacks. This resulted in an overall low average dT/dt due to a higher thermal mass applied to the thermoelectric cooler. The dT/dt and the temperature profile of the experiment are shown in Figure 5.13.

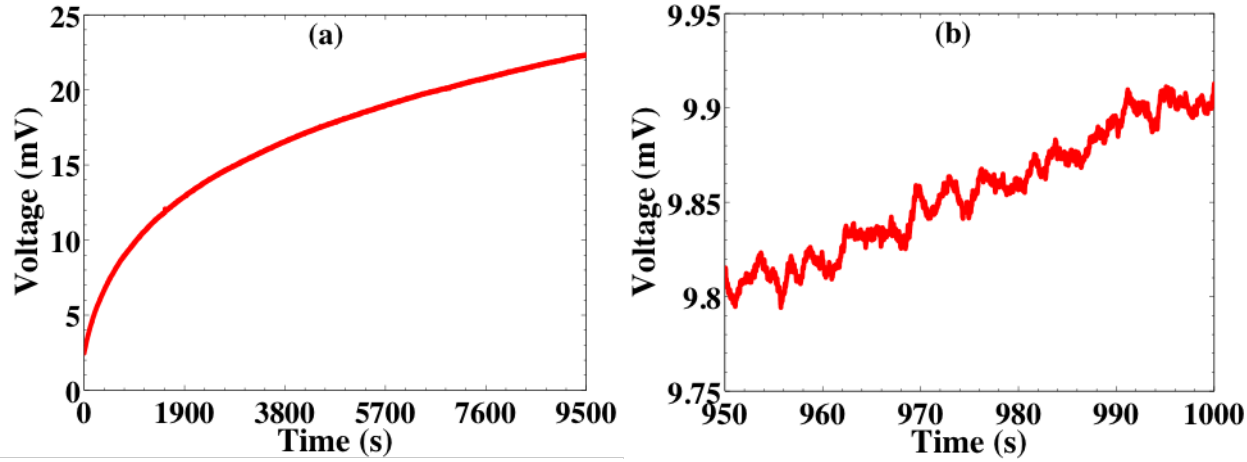


Figure 5.12: (a) Supercapacitor charging for 2.6 hours using three wafers stacked together (b) Charging profile for 50 s

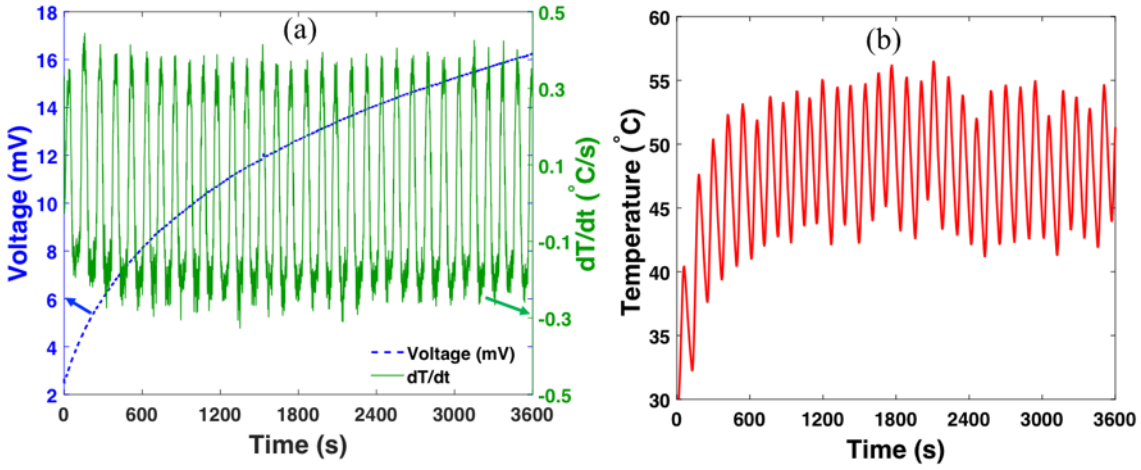


Figure 5.13: (a) Charging of the supercapacitor with dT/dt and (b) temperature profile for the first hour of charging

### 5.5.1 Comparison of PC-CON supercapacitor with a commercial supercapacitor

After it was established that $LiNbO_3$ can be a potential source of energy harvesting and it can charge a newly developed PC-CON supercapacitor, experiments were carried out to compare the energy storage capability of the PC-CON supercapacitor to a commercial supercapacitor of the similar capacitance (0.2F, Eaton M0510-2R5204-R supercapacitor, purchased from Mouser electronics). Figure 5.14 shows the charging profile of the supercapacitor for 1 hour. It can be seen that it was charged about 0.6mV in an hour, which is significantly lower than the PC-CON supercapacitor which gained about 5 mV in less than an hour and had already reached the maximum voltage (Figure 5.11). The charging was continued to find out the maximum voltage of the commercial supercapacitor. As can be seen from Figure 5.15 that after 9 hours of charging the maximum voltage was achieved and the supercapacitor gained about ~4.5 mV by this time. Therefore, it can be perceived that the PC-CON supercapacitor has faster charging capability than the commercial supercapacitor of similar capacitance value.

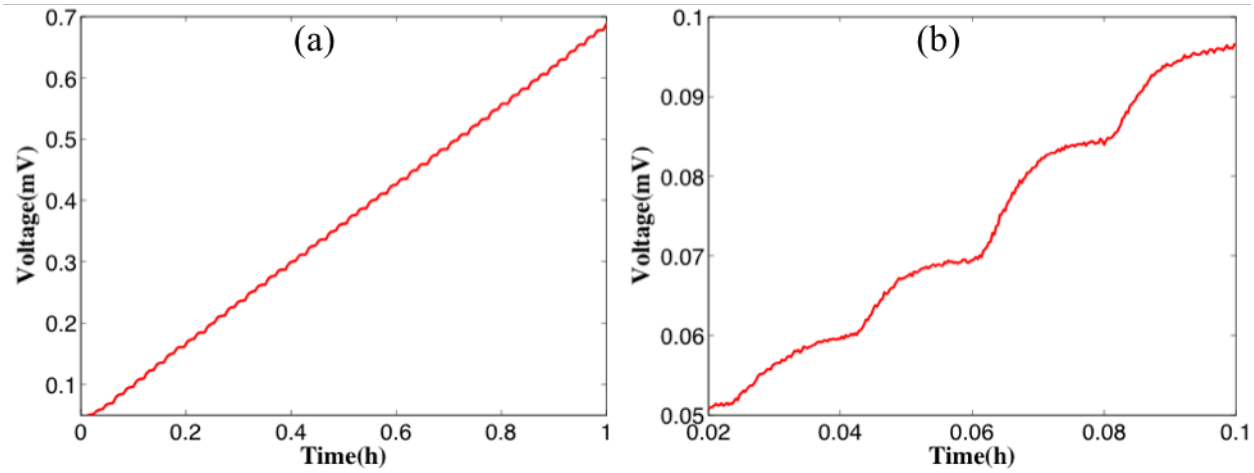


Figure 5.14: Charging of the commercial supercapacitor (a) Chargin profile for 1 hour, (b) Charging profile for first six minutes showing four cycle of heating and cooling

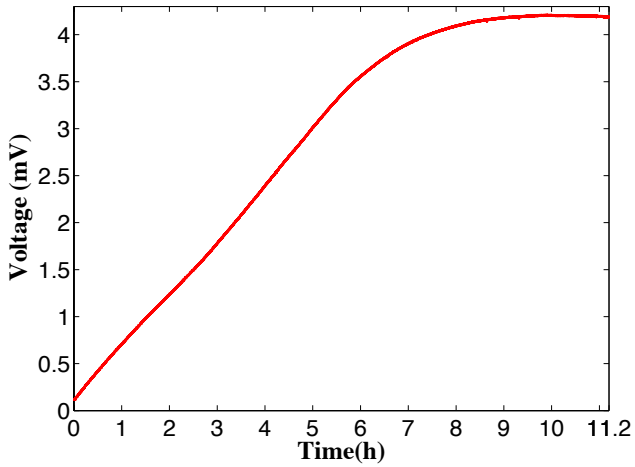


Figure 5.15: Charging profile of the commercial supercapacitor for 11.2 hours

### 5.5.2 Performance comparison of different diodes for energy harvesting application

It his known that Schottky diodes have lower voltage drops than other diodes [248] and hence Schottky diodes (NTE 573) were used for the experiments discussed so far. However, as the current produced by these pyroelectric energy harvester is really small; in the order of nanoampere, the reverse current through the diode could result in a more significant loss than the voltage drop during the forward bias. In this section we compare the performance of an Schottky diode (NTE 573) with HFA15TB60PBF diode (Mouser electronics), which has significantly lower specification for reverse current.

Figure 5.16 shows the voltage through a full-bridge circuit built using NTE 573 and the HFA15TB60PBF diode and it can be seen that although the NTE 573 was expected to have lower voltage drop than the HFA15TB60PBF diode, and which is true for high voltage and current in ampere scale, in the case of nano ampere current generated by the energy harvester the voltage drop is significantly high in NTE 573 and the harvested voltage is very low (maximum 35 mV). On the other hand, HFA15TB60PBF diode harvested voltage with minimal loss and the maximum-recorded voltage was around 6 V.

Figure 5.17 shows the comparison for reverse current flow during the negative cycle through a single diode. The forward current and the reverse current for both diodes are surprisingly close. For NTE 573 diode, the forward current goes to a maximum value of about

250 nA and for the reverse current it goes to about -200 nA for all the cycles. Whereas, for the HFA15TB60PBF diode the maximum forward current also goes about 250 nA, however, the reverse current is slightly over -150nA which would result in less loss during the negative cycle, compared to the NTE 573 diode.

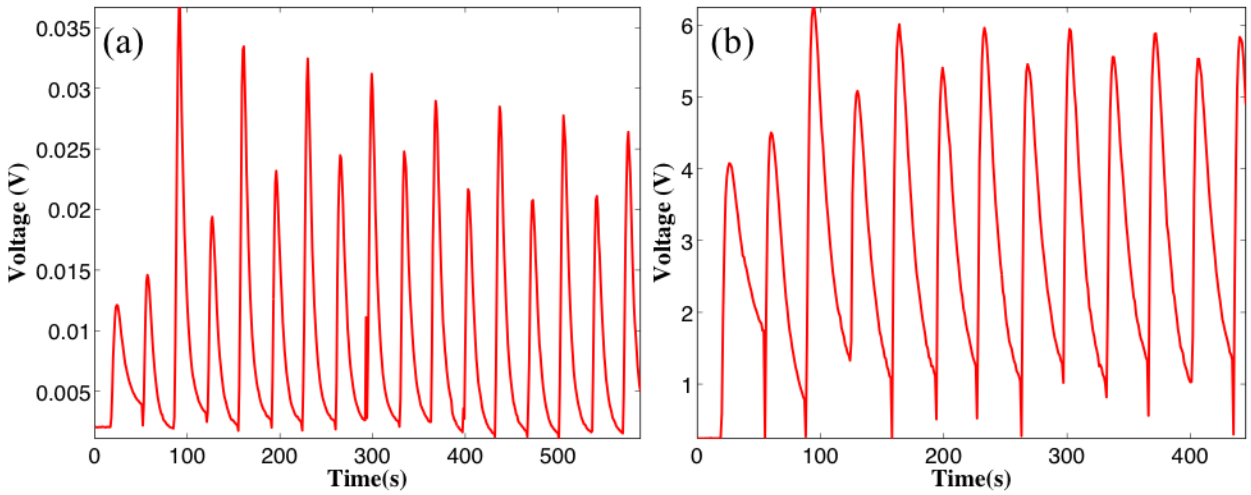


Figure 5.16: Voltage through the full bridge rectifier circuit consisting of (a) NTE 573 and (b) HFA15TB60PBF diode

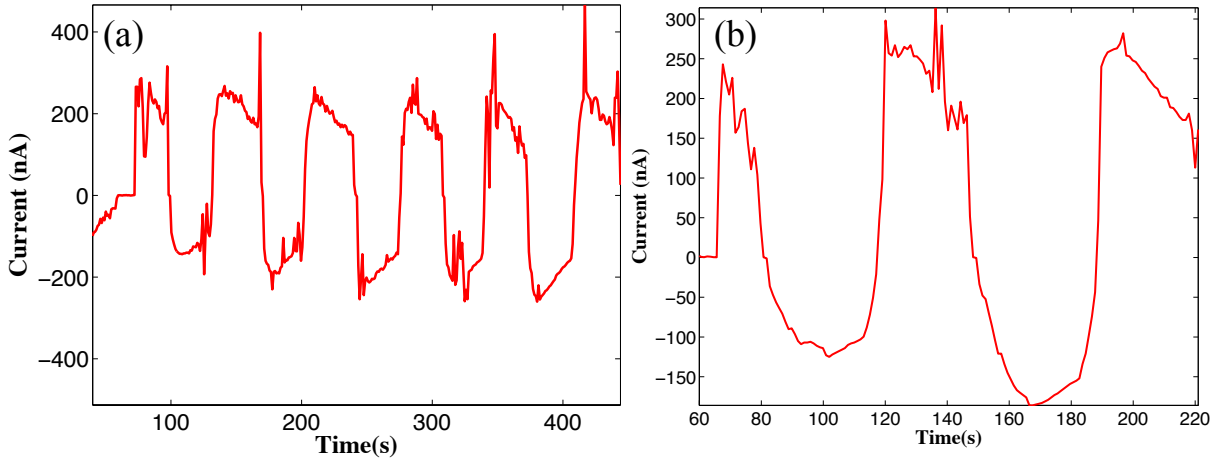


Figure 5.17: Current through a single diode during heating and cooling cycles, (a) NTE-573 and (b) HFA15TB60PBF diode

As it can be seen from the voltage and current comparison that the HFA15TB60PBF diode has significantly less power leakage during the forward and reverse cycle, it is expected

that it would perform significantly better than the NTE 573 while charging any energy storage unit. Figure 5.18 shows the charging profile of the same commercial supercapacitor that was charged using NTE 573 in Figure 5.14 and 5.15. It can be seen that after the first hour of charging using the HFA15TB60PBF diode, the supercapacitor gained abour 6 mV, whereas, for the NTE 573 diode it was about 0.7 mV. Also, after 10 hours of charging with the NTE 573 bridge circuit, the supercapacitor voltage had reached its maximum and it was only 4mV, while, with the HFA15TB60PBF diode bridge circuit, the voltage of the supercapacitor was about 70 mV, which is 10 times higher than the NTE 573 didode circuit.

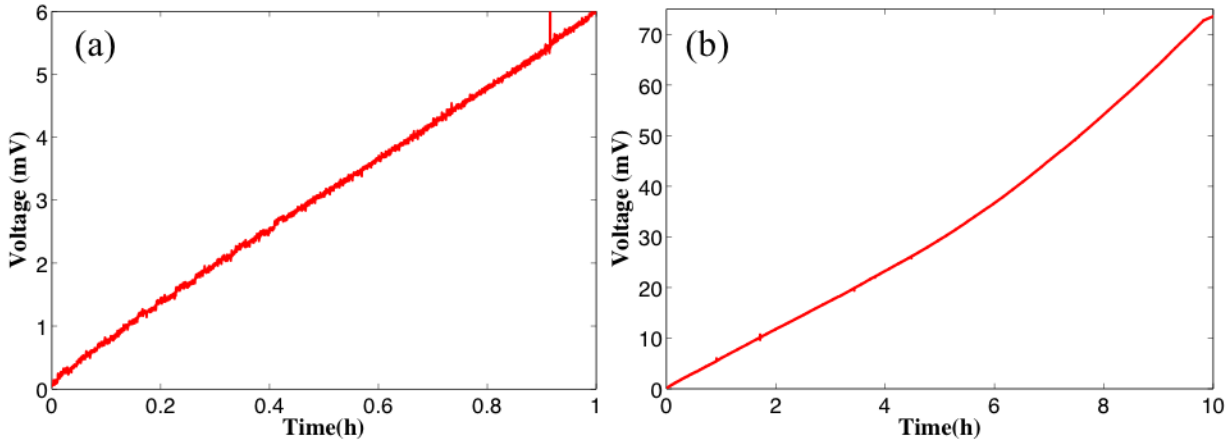


Figure 5.18: Charging of the commercial supercapacitor using HFA15TB60PBF diode (a) Chargin profile for 1 hour (b) Charging profile for 10 hours

**5.6 Conclusion**

A lead free alternative for PZT thermal energy harvesting and storage systems was investigated using $LiNbO_3$ (LNB) as the pyroelectric material. For this study a porous carbon based supercapacitor was used as an energy storage device. The current density of the LNB was found to be around 8 $nA/cm^2$, which is 20 times lower than PZT. However, $LiNbO_3$ proves to be a better alternative than ZnO due to the 4~5 times higher pyroelectric coefficient. It was demonstrated that the current produced by the LNB has the capability of charging a newly developed super-capacitor based on porous carbon – $CeO_2$ hybrid electrode. The charge density of the LNB was found to be 2.63 $mV/(hour \cdot cm^3)$ and the peak energy density generated was

437.72 nW/cm$^3$. Although the generated current is considerably lower for LNB, increasing the surface area or stacking multiple samples in a parallel configuration can help to achieve the desired amount of energy output. The fabricated PC-CON supercapacitor showed faster charging rate than the commercial supercapacitor of similar capacity. An investigation of the performance of two different kind of diode was carried out, it was observed that HFA15TB60PBF diode performs significantly better compared to NTE 573 which is a schottky diode. It can be concluded that the circuit components such as diodes and energy storage units are as important as the energy harvesting material itself and further investigation is required to select more efficient circuit elements and energy storage units in order to obtain the maximum possible output from the pyroelectric materials.

**Acknowledgement**

This research is supported by the U.S. Department of Energy, under award DE-FE0011235, SC-13-389 and the National Science Foundation under NSF-PREM grant No. DMR-1205302. However, any opinions, findings, conclusions, or recommendations expressed herein are those of the authors and do not necessarily reflect the views of the Department of Energy or the National Science Foundation.

# Chapter 6: Conclusion & Recommendation for Future Work

## 6.1 Conclusion

This dissertation utilizes functional materials on the effort towards two important problems of the current energy systems. On the first part of the dissertation a metamaterial based design of a passive and wireless temperature sensor for harsh environment application was investigated to ensure higher efficiency of operation of those systems. The proposed sensor would have a resonance frequency that will change linearly with the change in temperature. On Chapter 2 the feasibility of such a sensor is studied. The CRR structure was chosen for the simplicity of the structure and for ease of fabrication as commercial washers could be used as a cheap source of the CRR structure and high cost fabrication techniques such as lithography could be avoided. Finite element method using Ansys Ansoft HFSS was implemented in order to validate the feasibility of such sensor design. The CRR based design was compared to the other commonly observed split ring resonator based structures. Several factors were also investigated which could potentially influence the sensor resonance, such as the distance between the two CRRs and size of the split in case of the structures that had splits. It was observed the proposed CRR based structure has comparatively much higher resonance frequency than the other structures owing to the lack of split in the structure which creates additional capacitances in the split based structures and decreases the resonance frequency. More importantly, it was found from the simulations that the CRR based design is significantly more sensitive to the change of dielectric constant compared to all the other investigated structures, which made the CRR based design more suitable for a temperature sensor than the other investigated design.

Chapter 3 discussed the finalization of the design based on the preliminary design from chapter 2, fabrication and test of the sensor up to 200 °C. Initially Barium Titanate (BTO) was chosen to use as the dielectric material due to its highly temperature sensitive dielectric constant, however, the high loss tangent value of BTO made it impractical as there would not be any significant resonance response with this loss values. Simulation using HFSS predicted that a loss

value below 0.1 is necessary to obtain a decent resonance response from the sensor. To address this issue BTO was mixed with another high temperature but very low loss material, BN. Bruggeman effective media approach was used to calculate the final properties of the mixed material. It was found that for a composition of 70 vol% Boron Nitride and 30 vol% $BaTiO_3$ the loss tangent of the mixed materials drops below 0.1 and was chosen for the sensor fabrication. An infinite array simulation using floquet ports were carried out where the master and slave boundary conditions makes the sensor unit cell repeated infinitely in x and y directions. Based on the simulation it was seen that a resonance frequency exists in the desired working range of 7-16 GHz. A finite simulation of the dimension of 4 in by 4 in was carried out using PML boundary conditions to find out a more realistic response of the sensor and the result was quite similar to the infinite array simulation. The sample was prepared using a conventional compression of powders at high pressure using a die-punch assembly. The materials used in the fabrication was characterized using SEM and XRD. The dielectric properties of the materials were investigated using waveguides and split cavity resonators. It was found that the measured dielectric constants were lower than the initially estimated values, the infinite array simulation was updated using the measured dielectric properties and was found that the resonance of the sensor would fall between 10 GHz to ~14.5 GHz. Six tests were carried out from room temperature to up to 200 °C. The average resonance frequency at room temperature was 11.93 GHz and it decreased to 11.85 GHz at 200 °C. The maximum standard deviation was 0.012 GHz at 200 °C and the average sensitivity of the sensor in this range was 0.462 MHz/°C. As the resonance response found was different than the simulated responses, further simulations were carried out to understand the effect of the loss tangent and dielectric constant individually on the sensor response in order to match the experimental result. At first a loss tangent simulation was carried out from 0.014, which was the lowest value found in the dielectric properties characterization test to 0.1, having the dielectric constant fixed at 3.9. It was found that the increase in loss tangent not only decreases the intensity of the response, but also increases the resonance frequency as well as broadens the peak increasing the bandwidth. The loss value of 0.05426 generated the resonance

signal with a bandwidth of 1.24, which was the closest to the average experimental bandwidth of 1.23. On the next parametric simulation, the loss tangent was kept fixed at the above mentioned value and the dielectric constant was varied from 2.12 to 4.31, which was then further tuned in between 3.28 and 3.4 and the dielectric constant value that gives out the resonance frequency of 11.93 GHz was found to be 3.36. Based on the simulation it was found that the dielectric constant varies from 3.36 to 3.4 with the change in temperature from 23 to 200 °C.

The limitations of the sensor were investigated on chapter 4. Three factors were chosen for the investigation. First, the importance of a perfectly aligned test setup was investigated by measuring the sensor response at different angles of misalignment between the transmitting and receiving antennas. It was found that misalignment of both the transmitting and receiving antenna has impact on the resonance frequency detected by the network analyzer. However, for small misalignment up to 5 degrees the resonance frequency detected should be still reliable after proper calibration and time domain gating as long as there is no change in position of the antennas after the test has started. For misalignment of higher angles, the response could be a combination of reflected and scattered waves that is not truly the response of the sensor. The second factor that was investigated was the effect of humidity. It was seen that the resonance frequency of the sensor increases as the humidity increases to the point that the material of the sensor has achieved saturation. The author believes that the hygroscopic nature of the material BN, which constitute 70 vol% of the sensor is the principal reason behind the humidity impact on the sensor and by choosing a different material which is less hygroscopic than BN, the effect can be reduced. Out of the three factors tested, strain or mechanical deformation of the sensor geometry seems to have the most significant influence on the sensor response. For very small displacements up to 0.3 mm, the sensor response is stable and after that the resonance frequency shifts right gradually until there is a crack initiation at 0.65 mm and then the response changes rapidly and becomes unreliable. The mechanical strength of the sensor acts as the limitation of this type of ceramic material based sensor and it would not be very suitable for operation in an environment with significant amount of vibration.

On the second part of the dissertation a lead free alternative of PZT is reported for pyroelectric energy harvesting. $LiNbO_3$ (LNB) was the proposed material which has lower pyroelectric coefficient, however, the significantly higher curie temperature compared to PZT makes it appealing for high temperature operations of the energy conversion systems. A SAW grade, z-cut LNB wafer was chosen for the feasibility study. The sample was characterized using XRD to confirm that it was a single crystal. The electrical properties of the LNB wafer was measured at 1 Khz using a hp 4284A precision LCR meter and corresponding Norton equivalent circuit was reported. The current generated from a single LNB wafer was found to be about 0.4 μA for a dT/dt of 03 °C/s. A newly developed supercapacitor based on Porous carbon-$CeO_2$ nanoparticle based electrode was charged using the LNB wafer. It was found that the current generated from a single LNB wafer can charge the supercapacitor up to about 6 mV within an hour and gets saturated at that level. The supercapacitor was charged again with a stacke of three LNB wafers connected in parallel and was found that the supercapacitor reached over 20 mVs in 2.6 hours and was still not saturated, which proved that the energy harvesting capability can be increased by connecting more cells in parallel. The performance of PC-CON supercapcitor was compared with a commercial supercapacitor of similar capacitance and it was found that the PC-CON supercapacitor has faster charging rate than the commercial supercapacitor. The importance of using proper rectification circuit or componenets was investigated by comparing the Schottky diode (NTE 573) that was used for the initial experiments with another diode with a rated lower reverse current property and faster switching capability (HFA15TB60PBF). It was found that choosing the right diode can be extremely important in obtaining the highest efficiency in the energy harvesting process. The HFA15TB60PBF diode showed a comparatively lower reverse current leakage and significantly higher voltage after rectification from same experimental setup compared to the NTE 573 diode. When charging the same supercapacitor with the HFA15TB60PBF diode, the gained voltage of the supercapacitor was 10 times higher than that achieved by the NTE 573 diode.

In conclusion, this dissertation has developed two functional materials for applicaiton the energy conversion systems, the first one is a passive and wireless temperature sensor based on the concept of metamaterial. The response of the sensor as a function of temperature was demonstrated, detailed material characterization was performed at room temperature and HFSS based simulation was developed to predict the performance of the sensor. The effect of loss tangent and relative permittivity on the sensor response was investigated. The effect of misalignment in the test setup, change in humidity in the environment and mechanical load on the sensor was also investigated. The second part of the dissertation investigated a new material $LiNbO_3$ as a lead free alternative of PZT for pyroelectric energy harvesting. The feasibility of the material as a pyroelectric energy harvester was demonstrated as well as importance of choosing the proper circuit elements such as diodes and capacitor was also investigated. It was found that the reverse current leakage through diodes could be a significant limitation on the amount of energy harvested.

### 6.2 Recommendations for Future Work

This dissertation has performed the fundamental research to develop a passive, wireless temperature sensor for harsh environment application and investigated a lead free material for pyroelectricity based energy harvesting. As the dissertation demonstrated the sensing capability of the temperature sensor up to 200 °C, further investigation at higher temperatures is recommended to find out the full potential of the sensor. The sensor design was based on Closed Ring Resonator structure due to the simplicity compared to the split ring resonator, however, other simple structures such as rectangular thin metal plates or a combination of CRR with the rectangular metal plates could improve the sensor response by decreasing the bandwidth of the resonance peak and yet maintaining the simplicity of the design. Although the simulation predicts the sensor response within a small range, the lack of sufficient information about the dielectric properties of the materials at high temperature and high frequency makes it extremely difficult to have a good initial guess. It would be highly beneficial if material characterization at

high temperatures can also be carried out at the initial stage to achieve a better prediction of the sensor response. A metal with higher melting point such as Titanium or Platinum can be chosen to operate at higher temperature. As machining of such material is costly and very difficult, additive manufacturing of metal alloys such as Ti-6Al-4V can be a good alternative. The use of BN in the design has decreased the loss value of the combined materials to the desired level, however, it came with some costs. The sensor is highly influenced by the change in humidity in the environment and the mechanical strength of such a binary system tends to be lower than a single material system, which might cause it to fail under high load. Search for a new material with low loss and less hygroscopic behavior than BN is highly recommended.

On the feasibility study of $LiNbO_3$ as an alternative source for pyroelectric energy harvesting it was demonstrated that the choice of circuit elements and energy storage devices play a very important role in obtaining the maximum output from the source. It is recommended that other diodes as well as energy storage units such as capacitors and supercapacitors of different capacitance are investigated to understand which are more suitable for harvesting this very low energy sources. The energy harvesting was demonstrated in temperatures close to room temperature, it would be very interesting to see the performance of the material at higher temperatures as it has a higher curie temperature than most of the pyroelectric source and the pyroelectric coefficient also varies significantly at higher temperatures.

# References


1. Kuznetsov, V. and P. Edwards, *Functional materials for sustainable energy technologies: Four case studies*. ChemSusChem, 2010. **3**(1): p. 44-58.
2. Solomon, S., *Climate change 2007-the physical science basis: Working group I contribution to the fourth assessment report of the IPCC*. Vol. 4. 2007: Cambridge University Press.
3. King, D.A., *Climate change science: adapt, mitigate, or ignore?* Science(Washington), 2004. **303**(5655): p. 176-177.
4. Sarker, M.R.H., et al., *Temperature measurements using a lithium niobate (LiNbO 3) pyroelectric ceramic*. Measurement, 2015. **75**: p. 104-110.
5. Karim, H., et al., *Concept and model of a metamaterial-based passive wireless temperature sensor for harsh environment applications*. Sensors Journal, IEEE, 2015. **15**(3): p. 1445-1452.
6. Karim, H., et al., *Feasibility study of thermal energy harvesting using lead free pyroelectrics*. Smart Materials and Structures, 2016. **25**(5): p. 055022.
7. Ottman, G.K., H.F. Hofmann, and G.A. Lesieutre, *Optimized piezoelectric energy harvesting circuit using step-down converter in discontinuous conduction mode*. Power Electronics, IEEE Transactions on, 2003. **18**(2): p. 696-703.
8. Shuvo, M.A.I., et al., *Microwave exfoliated graphene oxide/TiO2 nanowire hybrid for high performance lithium ion battery*. Journal of Applied Physics, 2015. **118**(12): p. 125102.
9. Rajib, M., et al., *Enhanced Energy Storage of Dielectric Nanocomposites at Elevated Temperatures*. International Journal of Applied Ceramic Technology, 2016. **13**(1): p. 125-132.
10. Karim, H., et al. *Porous carbon/CeO2 composites for Li-ion battery application*. in *SPIE Smart Structures and Materials+ Nondestructive Evaluation and Health Monitoring*. 2015. International Society for Optics and Photonics.
11. Rajib, M., et al., *Temperature influence on dielectric energy storage of nanocomposites*. Ceramics International, 2015. **41**(1): p. 1807-1813.
12. Shuvo, M.A.I., et al., *Nanowire modified carbon fibers for enhanced electrical energy storage*. Journal of Applied Physics, 2013. **114**(10): p. 104306.
13. Shuvo, M.A.I., et al., *Investigation of modified graphene for energy storage applications*. ACS applied materials & interfaces, 2013. **5**(16): p. 7881-7885.
14. Chao, X., J.B. Jeffries, and R.K. Hanson, *Real-time, in situ, continuous monitoring of CO in a pulverized-coal-fired power plant with a 2.3 μm laser absorption sensor*. Applied Physics B, 2013. **110**(3): p. 359-365.
15. Kaiser, S., M. Schild, and C. Schulz, *Thermal stratification in an internal combustion engine due to wall heat transfer measured by laser-induced fluorescence*. Proceedings of the Combustion Institute, 2013. **34**(2): p. 2911-2919.

16. Ueda, T., R. Nozaki, and A. Hosokawa, *Temperature measurement of cutting edge in drilling-effect of oil mist*. CIRP Annals-Manufacturing Technology, 2007. **56**(1): p. 93-96.

17. Bezergianni, S. and A. Dimitriadis, *Temperature effect on co-hydroprocessing of heavy gas oil–waste cooking oil mixtures for hybrid diesel production*. Fuel, 2013. **103**: p. 579-584.

18. Opasjumruskit, K., et al., *Self-powered wireless temperature sensors exploit RFID technology*. Pervasive computing, IEEE, 2006. **5**(1): p. 54-61.

19. Seidel, W., et al., *Phase transition thermometers with high temperature resolution for calorimetric particle detectors employing dielectric absorbers*. Physics Letters B, 1990. **236**(4): p. 483-487.

20. Zhang, Z., K. Grattan, and A. Palmer, *Fiber optic temperature sensor based on the cross referencing between blackbody radiation and fluorescence lifetime*. Review of scientific Instruments, 1992. **63**(5): p. 3177-3181.

21. Canning, J., K. Sommer, and M. Englund, *Fibre gratings for high temperature sensor applications*. Measurement Science and Technology, 2001. **12**(7): p. 824.

22. Scholl, G., et al., *SAW-based radio sensor systems for short-range applications*. Microwave Magazine, IEEE, 2003. **4**(4): p. 68-76.

23. Yang, J., *A silicon carbide wireless temperature sensing system for high temperature applications*. Sensors, 2013. **13**(2): p. 1884-1901.

24. Huang, P., et al., *The evolution of MAC protocols in wireless sensor networks: A survey*. Communications Surveys & Tutorials, IEEE, 2013. **15**(1): p. 101-120.

25. Tyagi, S. and N. Kumar, *A systematic review on clustering and routing techniques based upon LEACH protocol for wireless sensor networks*. Journal of Network and Computer Applications, 2013. **36**(2): p. 623-645.

26. Jeong, S., et al., *A fully-integrated 71 nW CMOS temperature sensor for low power wireless sensor nodes*. Solid-State Circuits, IEEE Journal of, 2014. **49**(8): p. 1682-1693.

27. Jabbar, H., Y.S. Song, and T.T. Jeong, *RF energy harvesting system and circuits for charging of mobile devices*. Consumer Electronics, IEEE Transactions on, 2010. **56**(1): p. 247-253.

28. Tadesse, Y., S. Zhang, and S. Priya, *Multimodal energy harvesting system: piezoelectric and electromagnetic*. Journal of Intelligent Material Systems and Structures, 2009. **20**(5): p. 625-632.

29. Raghunathan, V., et al. *Design considerations for solar energy harvesting wireless embedded systems*. in *Proceedings of the 4th international symposium on Information processing in sensor networks*. 2005. IEEE Press.

30. Ploss, B., et al., *Pyroelectric activity of ferroelectric PT/PVDF-TRFE*. Dielectrics and Electrical Insulation, IEEE Transactions on, 2000. **7**(4): p. 517-522.

31. Hilczer, B., et al., *Dielectric relaxation in ferroelectric PZT–PVDF nanocomposites*. Journal of Non-Crystalline Solids, 2002. **305**(1): p. 167-173.

32. Yang, Y., et al., *Pyroelectric nanogenerators for harvesting thermoelectric energy*. Nano letters, 2012. **12**(6): p. 2833-2838.

33. Bergman, J., et al., *CURIE TEMPERATURE, BIREFRINGENCE, AND PHASE-MATCHING TEMPERATURE VARIATIONS IN LiNbO3 AS A FUNCTION OF MELT STOICHIOMETRY*. Applied Physics Letters, 1968. **12**(3): p. 92-94.

34. Alù, A., A. Salandrino, and N. Engheta, *Negative effective permeability and left-handed materials at optical frequencies*. Optics express, 2006. **14**(4): p. 1557-1567.

35. Karami Horestani, A., *Metamaterial-inspired structures and their applications in microwave, millimeter-wave and terahertz planar circuits*. 2014.

36. Hardy, W. and L. Whitehead, *Split-ring resonator for use in magnetic resonance from 200–2000 MHz*. Review of Scientific Instruments, 1981. **52**(2): p. 213-216.

37. Bonache, J., et al., *Novel microstrip bandpass filters based on complementary split-ring resonators*. Microwave Theory and Techniques, IEEE Transactions on, 2006. **54**(1): p. 265-271.

38. Linden, S., et al., *Magnetic response of metamaterials at 100 terahertz*. Science, 2004. **306**(5700): p. 1351-1353.

39. Gil, M., et al., *Broadband resonant-type metamaterial transmission lines*. Microwave and Wireless Components Letters, IEEE, 2007. **17**(2): p. 97-99.

40. Jarauta, E., et al., *Novel microstrip backward coupler with metamaterial cells for fully planar fabrication techniques*. Microwave and optical technology letters, 2006. **48**(6): p. 1205-1209.

41. Paredes, F., et al., *Recent advances in multiband printed antennas based on metamaterial loading*. Advances in OptoElectronics, 2012. **2012**.

42. García-García, J., et al., *Microwave filters with improved stopband based on sub-wavelength resonators*. Microwave Theory and Techniques, IEEE Transactions on, 2005. **53**(6): p. 1997-2006.

43. Melik, R., et al., *Flexible metamaterials for wireless strain sensing*. Applied Physics Letters, 2009. **95**(18): p. 181105.

44. Ishimaru, A., S. Jaruwatanadilok, and Y. Kuga, *Generalized surface plasmon resonance sensors using metamaterials and negative index materials*. Progress In Electromagnetics Research, 2005. **51**: p. 139-152.

45. Naqui, J., M. Durán-Sindreu, and F. Martín, *Novel sensors based on the symmetry properties of split ring resonators (SRRs)*. Sensors, 2011. **11**(8): p. 7545-7553.

46. Naqui, J., M. Durán-Sindreu, and F. Martín, *Alignment and position sensors based on split ring resonators*. Sensors, 2012. **12**(9): p. 11790-11797.

47. Schueler, M., et al., *Metamaterial inspired microwave sensors*. Microwave Magazine, IEEE, 2012. **13**(2): p. 57-68.

48. Smith, D., J. Pendry, and M. Wiltshire, *Metamaterials and negative refractive index*. Science, 2004. **305**(5685): p. 788-792.

49. Veselago, V.G., *THE ELECTRODYNAMICS OF SUBSTANCES WITH SIMULTANEOUSLY NEGATIVE VALUES OF IMG align= ABSMIDDLE alt= œµ eps/IMG AND Œº*. Physics-Uspekhi, 1968. **10**(4): p. 509-514.

50. Katsarakis, N., et al., *Electric coupling to the magnetic resonance of split ring resonators*. Applied physics letters, 2004. **84**(15): p. 2943-2945.

51. Katsarakis, N., et al., *Magnetic response of split-ring resonators in the far-infrared frequency regime*. Optics Letters, 2005. **30**(11): p. 1348-1350.

52. Ekmekci, E., R. Averitt, and G. Turhan-Sayan. *Effects of Substrate Parameters on the Resonance Frequency of Double-sided SRR Structures under Two Different Excitations*. in *Symposium Proceedings of the Progress in Electromagnetic Research*. 2010.

53. Ekmekci, E., *Design, fabrication and characterization of novel metamaterials in microwave and terahertz regions: multi-band, frequency-tunable and miniaturized structures*, in *Electrical and Electronics Engineering*. 2010, Middle East Technical University.

54. Pendry, J.B., et al., *Magnetism from conductors and enhanced nonlinear phenomena*. Microwave Theory and Techniques, IEEE Transactions on, 1999. **47**(11): p. 2075-2084.

55. Shakoor, A., *Design Fabrication and Characterization of Split Ring Resonators in the Near Infrared Region*.

56. Aydin, K., et al., *Investigation of magnetic resonances for different split-ring resonator parameters and designs*. New journal of physics, 2005. **7**(1): p. 168.

57. Zhang, S., J. Xiao, and Y. Li, *Novel microstrip band-stop filters based on complementary split ring resonators*. Microwave Journal, 2006. **49**(11): p. 100.

58. Chen, H.-T., et al., *Active terahertz metamaterial devices*. Nature, 2006. **444**(7119): p. 597-600.

59. Chen, H.-T., et al., *A metamaterial solid-state terahertz phase modulator*. Nature photonics, 2009. **3**(3): p. 148-151.

60. Grimberg, R., *Electromagnetic metamaterials*. Materials Science and Engineering: B, 2013.

61. Freire, M.J., R. Marques, and L. Jelinek, *Experimental demonstration of a Œº=,àí 1 metamaterial lens for magnetic resonance imaging*. Applied physics letters, 2008. **93**: p. 231108.

62. Pendry, J.B., *Negative refraction makes a perfect lens*. Physical review letters, 2000. **85**(18): p. 3966.

63. Wood, B., *Metamaterials and invisibility*. Comptes Rendus Physique, 2009. **10**(5): p. 379-390.

64. Pendry, J.B., D. Schurig, and D.R. Smith, *Controlling electromagnetic fields*. Science, 2006. **312**(5781): p. 1780-1782.

65. Schurig, D., et al., *Metamaterial electromagnetic cloak at microwave frequencies*. Science, 2006. **314**(5801): p. 977-980.

66. Chen, H. and C. Chan, *Acoustic cloaking in three dimensions using acoustic metamaterials*. Applied physics letters, 2007. **91**(18): p. 183518-183518-3.

67. Lai, Y., et al., *Hybrid elastic solids*. Nature materials, 2011. **10**(8): p. 620-624.

68. Torres-Silva, H. and D.T. Cabezas, *Chiral Seismic Attenuation with Acoustic Metamaterials*. Journal of Electromagnetics Analysis and Applications, 2013. **5**(1): p. 10-15.

69. Chen, T., S. Li, and H. Sun, *Metamaterials application in sensing*. Sensors, 2012. **12**(3): p. 2742-2765.

70. Lee, H.-J. and J.-G. Yook, *Biosensing using split-ring resonators at microwave regime*. Applied physics letters, 2008. **92**(25): p. 254103-254103-3.

71. Tao, H., et al., *Metamaterials on paper as a sensing platform*. Advanced Materials, 2011. **23**(28): p. 3197-3201.

72. Kabashin, A., et al., *Plasmonic nanorod metamaterials for biosensing*. Nature materials, 2009. **8**(11): p. 867-871.

73. Yoshida, H., et al., *Terahertz sensing method for protein detection using a thin metallic mesh*. Applied physics letters, 2007. **91**(25): p. 253901-253901-3.

74. Melik, R., et al., *Flexible metamaterials for wireless strain sensing*. Applied physics letters, 2009. **95**(18): p. 181105-181105-3.

75. Ekmekci, E. and G. Turhan-Sayan. *Metamaterial sensor applications based on broadside-coupled SRR and V-Shaped resonator structures*. in *Antennas and Propagation (APSURSI), 2011 IEEE International Symposium on*. 2011. IEEE.

76. Kadic, M., et al., *Metamaterials beyond electromagnetism*. Reports on progress in physics. Physical Society (Great Britain), 2013. **76**(12): p. 126501-126501.

77. Engheta, N. *Metamaterials with negative permittivity and permeability: background, salient features, and new trends*. in *Microwave Symposium Digest, 2003 IEEE MTT-S International*. 2003. IEEE.

78. Bose, J.C., *On the rotation of plane of polarisation of electric waves by a twisted structure*. Proceedings of the Royal Society of London, 1898. **63**(389-400): p. 146-152.

79. Lindman, K.F., *√úber eine durch ein isotropes System von spiralf√∂rmigen Resonatoren erzeugte Rotationspolarisation der elektromagnetischen Wellen*. Annalen der Physik, 1920. **368**(23): p. 621-644.

80. Kock, W.E., *Metallic delay lenses*. Bell Syst. Tech. J., 1948. **27**: p. 58-82.

81. Veselago, V., *PROPERTIES OF MATERIALS HAVING SIMULTANEOUSLY NEGATIVE VALUES OF THE DIELECTRIC (¬£) AND THE MAGNETIC (ju) SUSCEPTIBILITIES*. Soviet Physics-Solid State, 1967. **8**(12).

82. Pendry, J., et al., *Extremely low frequency plasmons in metallic mesostructures*. Physical review letters, 1996. **76**(25): p. 4773.

83. Smith, D.R., et al., *Composite medium with simultaneously negative permeability and permittivity*. Physical review letters, 2000. **84**(18): p. 4184.

84. Shelby, R.A., D.R. Smith, and S. Schultz, *Experimental verification of a negative index of refraction*. Science, 2001. **292**(5514): p. 77-79.

85. Grzegorczyk, T. and J. Kong, *Review of left-handed metamaterials: Evolution from theoretical and numerical studies to potential applications*. Journal of Electromagnetic Waves and Applications, 2006. **20**(14): p. 2053-2064.

86. O,Äôbrien, S. and J. Pendry, *Magnetic activity at infrared frequencies in structured metallic photonic crystals*. Journal of Physics: Condensed Matter, 2002. **14**(25): p. 6383.

87. Grzegorczyk, T.M., et al., *Properties of left-handed metamaterials: transmission, backward phase, negative refraction, and focusing*. Microwave Theory and Techniques, IEEE Transactions on, 2005. **53**(9): p. 2956-2967.

88. Marques, R., F. Medina, and R. Rafii-El-Idrissi, *Role of bianisotropy in negative permeability and left-handed metamaterials*. Physical Review B, 2002. **65**(14): p. 144440.

89. Saadoun, M.M. and N. Engheta, *A reciprocal phase shifter using novel pseudochiral or Œ© medium*. Microwave and Optical Technology Letters, 1992. **5**(4): p. 184-188.

90. Huangfu, J., et al., *Experimental confirmation of negative refractive index of a metamaterial composed of Œ©-like metallic patterns*. Applied physics letters, 2004. **84**(9): p. 1537-1539.

91. Chen, H., et al., *Negative refraction of a combined double S-shaped metamaterial*. Applied physics letters, 2005. **86**(15): p. 151909-151909-3.

92. Chen, H., et al., *Magnetic properties of S-shaped split-ring resonators*. Progress In Electromagnetics Research, 2005. **51**: p. 231-247.

93. Gay-Balmaz, P. and O.J. Martin, *Efficient isotropic magnetic resonators*. Applied physics letters, 2002. **81**(5): p. 939-941.

94. Yao, H.-Y., et al., *Macroscopic performance analysis of metamaterials synthesized from micrsocopic 2-D isotropic cross split-ring resonator array*. Progress In Electromagnetics Research, 2005. **51**: p. 197-217.

95. Wongkasem, N., A. Akyurtlu, and K.A. Marx, *Group theory based design of isotropic negative refractive index metamaterials*. Progress In Electromagnetics Research, 2006. **63**: p. 295-310.

96. Vendik, I. and O. Vendik, *Metamaterials and their application in microwaves: A review*. Technical Physics, 2013. **58**(1): p. 1-24.

97. Vendik, O. and M. Gashinova, *Proceedings of the 34th European Microwave Conference, Amsterdam, The Netherlands, 2004*. 2004.

98. Chen, H., et al., *Equivalent circuit model for left-handed metamaterials*. Journal of applied physics, 2006. **100**(2): p. 024915-024915-6.

99. Moss, C., T. Grzegorczyk, and Y. Zhang, *Numerical studies of left handed metamaterials*. Progress In Electromagnetics Research, 2002. **35**: p. 315-334.

100. Lindell, I.V., et al., *Electromagnetic waves in chiral and bi-isotropic media*. 1994.

101. Wang, B., et al., *Chiral metamaterials: simulations and experiments*. Journal of Optics A: Pure and Applied Optics, 2009. **11**(11): p. 114003.

102. Barron, L.D., *Molecular light scattering and optical activity*. 2004: Cambridge University Press.

103. Tretyakov, S., et al., *Waves and energy in chiral nihility*. Journal of Electromagnetic Waves and Applications, 2003. **17**(5): p. 695-706.

104. Pendry, J., *A chiral route to negative refraction*. Science, 2004. **306**(5700): p. 1353-1355.

105. Marques, R., L. Jelinek, and F. Mesa, *Negative refraction from balanced quasi‚Äêplanar chiral inclusions*. Microwave and Optical Technology Letters, 2007. **49**(10): p. 2606-2609.

106. Baena, J., L. Jelinek, and R. Marqu√©s, *Towards a systematic design of isotropic bulk magnetic metamaterials using the cubic point groups of symmetry*. Physical Review B, 2007. **76**(24): p. 245115.

107. Jelinek, L., et al., *Periodic arrangements of chiral scatterers providing negative refractive index bi-isotropic media*. Physical Review B, 2008. **77**(20): p. 205110.

108. Frank, B., et al., *Large-Area 3D Chiral Plasmonic Structures*. ACS nano, 2013. **7**(7): p. 6321-6329.

109. Tang, Y., *Chirality of Light and Its Interaction with Chiral Matter*. 2013.

110. Han, C., H.M. Leung, and W.Y. Tam, *Chiral metamaterials by shadowing vapor deposition*. Journal of Optics, 2013. **15**(7): p. 072101.

111. Papakostas, A., et al., *Optical manifestations of planar chirality*. Physical review letters, 2003. **90**(10): p. 107404.

112. Rogacheva, A., et al., *Giant gyrotropy due to electromagnetic-field coupling in a bilayered chiral structure*. Physical review letters, 2006. **97**(17): p. 177401.

113. Zhang, S., et al., *Negative refractive index in chiral metamaterials*. Physical review letters, 2009. **102**(2): p. 023901.

114. Murugkar, S., et al. *Planar chiral metamaterials for biosensing applications*. in *SPIE BiOS*. 2013. International Society for Optics and Photonics.

115. Novitsky, A.V., V.M. Galynsky, and S.V. Zhukovsky, *Asymmetric transmission in planar chiral split-ring metamaterials: Microscopic Lorentz-theory approach*. Physical Review B, 2012. **86**(7): p. 075138.

116. Mahmoud, S.F. and A.J. Viitanen, *Surface wave character on a slab of metamaterial with negative permittivity and permeability*. Progress In Electromagnetics Research, 2005. **51**: p. 127-137.

117. Enoch, S., et al., *A metamaterial for directive emission*. Physical review letters, 2002. **89**(21): p. 213902.

118. Hamid, A.-K., *Axially slotted antenna on a circular or elliptic cylinder coated with metamaterials*. Progress In Electromagnetics Research, 2005. **51**: p. 329-341.

119. Engheta, N., *An idea for thin subwavelength cavity resonators using metamaterials with negative permittivity and permeability*. Antennas and Wireless Propagation Letters, IEEE, 2002. **1**(1): p. 10-13.

120. Shi, Y. and C.-H. Liang, *Analysis of the left-handed metamaterials using multi-domain pseudospectral time-domain algorithm*. Progress In Electromagnetics Research, 2005. **51**: p. 153-165.

121. Shooshtari, A. and A.R. Sebak, *Electromagnetic scattering by parallel metamaterial cylinders*. Progress In Electromagnetics Research, 2006. **57**: p. 165-177.

122. Yang, F., et al., *DC electric invisibility cloak*. Physical review letters, 2012. **109**(5): p. 053902.

123. Fan, C., Y. Gao, and J. Huang, *Shaped graded materials with an apparent negative thermal conductivity*. Applied physics letters, 2008. **92**(25): p. 251907-251907-3.

124. Li, J., Y. Gao, and J. Huang, *A bifunctional cloak using transformation media*. Journal of applied physics, 2010. **108**(7): p. 074504-074504-5.

125. Chen, T., C.-N. Weng, and J.-S. Chen, *Cloak for curvilinearly anisotropic media in conduction*. Applied physics letters, 2008. **93**(11): p. 114103-114103-3.

126. Guenneau, S., C. Amra, and D. Veynante, *Transformation thermodynamics: cloaking and concentrating heat flux*. Optics Express, 2012. **20**(7): p. 8207-8218.

127. Schittny, R., et al., *Experiments on transformation thermodynamics: Molding the flow of heat*. Physical review letters, 2013. **110**(19): p. 195901.

128. Liang, Z. and J. Li, *Extreme acoustic metamaterial by coiling up space*. Physical review letters, 2012. **108**(11): p. 114301.

129. Frenzel, T., et al., *Three-dimensional labyrinthine acoustic metamaterials*. Applied physics letters, 2013. **103**(6): p. 061907-061907-4.

130. Liu, Z., et al., *Locally resonant sonic materials*. Science, 2000. **289**(5485): p. 1734-1736.

131. Schaedler, T., et al., *Ultralight metallic microlattices*. Science, 2011. **334**(6058): p. 962-965.

132. Buckmann, T., et al., *Tailored 3D Mechanical Metamaterials Made by Dip,ÄêIn Direct,ÄêLaser,ÄêWriting Optical Lithography*. Advanced Materials, 2012. **24**(20): p. 2710-2714.

133. Schimetta, G., et al. *Wireless pressure and temperature measurement using a SAW hybrid sensor*. in *Ultrasonics Symposium, 2000 IEEE*. 2000. IEEE.

134. Ballandras, S., et al. *Wireless temperature sensor using SAW resonators for immersed and biological applications*. in *Ultrasonics Symposium, 2002. Proceedings. 2002 IEEE*. 2002. IEEE.

135. Hornsteiner, J., E. Born, and E. Riha, *Langasite for high temperature surface acoustic wave applications*. physica status solidi (a), 1997. **163**(1): p. R3-R4.

136. Hornsteiner, J., et al. *Surface acoustic wave sensors for high-temperature applications*. in *Frequency Control Symposium, 1998. Proceedings of the 1998 IEEE International*. 1998. IEEE.

137. Bulst, W.-E., G. Fischerauer, and L. Reindl, *State of the art in wireless sensing with surface acoustic waves*. Industrial Electronics, IEEE Transactions on, 2001. **48**(2): p. 265-271.

138. Reindl, L., et al. *Wireless measurement of temperature using surface acoustic waves sensors*. in *Frequency control symposium and PDA exhibition jointly with the 17th European frequency and time forum, 2003. Proceedings of the 2003 IEEE international*. 2003. IEEE.

139. Wang, Y., et al., *A passive wireless temperature sensor for harsh environment applications*. Sensors, 2008. **8**(12): p. 7982-7995.

140. Ong, K.G., et al., *Design and application of a wireless, passive, resonant-circuit environmental monitoring sensor*. Sensors and Actuators A: Physical, 2001. **93**(1): p. 33-43.

141. Kocer, F., P.M. Walsh, and M.P. Flynn. *An RF powered, wireless temperature sensor in quarter micron CMOS*. in *Circuits and Systems, 2004. ISCAS'04. Proceedings of the 2004 International Symposium on*. 2004. IEEE.

142. Souri, K., Y. Chae, and K. Makinwa. *A CMOS temperature sensor with a voltage-calibrated inaccuracy of¬±0.15¬∞ C (3œÉ) from,àí 55 to 125¬∞ C*. in *Solid-State Circuits Conference Digest of Technical Papers (ISSCC), 2012 IEEE International*. 2012. IEEE.

143. Cheng, H., S. Ebadi, and X. Gong, *A Low-Profile Wireless Passive Temperature Sensor Using Resonator/Antenna Integration Up to 1000< formula formulatype=*. Antennas and Wireless Propagation Letters, IEEE, 2012. **11**: p. 369-372.

144. Thai, T.T., et al. *A novel passive wireless ultrasensitive RF temperature transducer for remote sensing*. in *Microwave Symposium Digest (MTT), 2010 IEEE MTT-S International*. 2010. IEEE.

145. Ekmekci, E. and G. Turhan-Sayan, *Multi-functional metamaterial sensor based on a broad-side coupled SRR topology with a multi-layer substrate*. Applied Physics A, 2013. **110**(1): p. 189-197.

146. Khaligh, A., P. Zeng, and C. Zheng, *Kinetic energy harvesting using piezoelectric and electromagnetic technologies—state of the art*. Industrial Electronics, IEEE Transactions on, 2010. **57**(3): p. 850-860.

147. Lin, Y.-F., et al., *Piezoelectric nanogenerator using CdS nanowires*. Applied Physics Letters, 2008. **92**(2): p. 022105.

148. Cha, S.N., et al., *Sound-Driven Piezoelectric Nanowire-Based Nanogenerators*. Advanced materials, 2010. **22**(42): p. 4726-4730.

149. Kao, P.-H., et al., *Fabrication and characterization of CMOS-MEMS thermoelectric micro generators*. Sensors, 2010. **10**(2): p. 1315-1325.

150. Glatz, W., et al., *-Based Flexible Micro Thermoelectric Generator With Optimized Design*. Microelectromechanical Systems, Journal of, 2009. **18**(3): p. 763-772.

151. Stordeur, M. and I. Stark. *Low power thermoelectric generator-self-sufficient energy supply for micro systems*. in *Thermoelectrics, 1997. Proceedings ICT'97. XVI International Conference on*. 1997. IEEE.

152. Karim, H., et al. *Pyro-electric energy harvesting with a high Curie temperature material LiNbO3*. in *SPIE Smart Structures and Materials+ Nondestructive Evaluation and Health Monitoring*. 2016. International Society for Optics and Photonics.

153. Yang, Y., et al., *Flexible Pyroelectric Nanogenerators using a Composite Structure of Lead-Free KNbO3 Nanowires*. Advanced Materials, 2012. **24**(39): p. 5357-5362.

154. Shoaee, S., et al., *Acoustic enhancement of polymer/ZnO nanorod photovoltaic device performance*. Advanced Materials, 2014. **26**(2): p. 263-268.

155. Salvatierra, R.V., et al., *ITO-Free and Flexible Organic Photovoltaic Device Based on High Transparent and Conductive Polyaniline/Carbon Nanotube Thin Films*. Advanced Functional Materials, 2013. **23**(12): p. 1490-1499.

156. Gierczak, M., P. Markowski, and A. Dziedzic. *Design, fabrication and characterization of LTCC-based electromagnetic microgenerators*. in *IOP Conference Series: Materials Science and Engineering*. 2016. IOP Publishing.

157. Dayal, R. and L. Parsa, *Modified electromagnetic microgenerator design for improved performance of low-voltage energy-harvesting systems*. Power Electronics, IET, 2013. **6**(9): p. 1751-1758.

158. Sebald, G., D. Guyomar, and A. Agbossou, *On thermoelectric and pyroelectric energy harvesting*. Smart Materials and Structures, 2009. **18**(12): p. 125006.

159. Batra, A.K., M.D. Aggarwal, and S. Press, *Pyroelectric Materials: Infrared Detectors, Particle Accelerators and Energy Harvesters*. 2013: SPIE Press.

160. Gautschi, D.-I.E.G., *Piezoelectric sensors*. 2002: Springer.

161. Lal, R. and A. Batra, *Growth and properties of triglycine sulfate (TGS) crystals: review*. Ferroelectrics, 1993. **142**(1): p. 51-82.

162. Lang, S.B., *Pyroelectricity: from ancient curiosity to modern imaging tool*. Physics Today, 2005. **58**(8): p. 31-36.

163. Vasileska, D. and S.M. Goodnick, *Nano-Electronic Devices: Semiclassical and Quantum Transport Modeling*. 2011: Springer Science & Business Media.

164. Lingam, D., et al., *Nano/microscale pyroelectric energy harvesting: challenges and opportunities*. International Journal of Smart and Nano Materials, 2013. **4**(4): p. 229-245.

165. Ye, C.p., T. Tamagawa, and D. Polla, *Experimental studies on primary and secondary pyroelectric effects in Pb (ZrxTi1− x) O3, PbTiO3, and ZnO thin films*. Journal of applied physics, 1991. **70**(10): p. 5538-5543.

166. Lee, M., R. Guo, and A.S. Bhalla, *Pyroelectric sensors*. Journal of Electroceramics, 1998. **2**(4): p. 229-242.

167. Cuadras, A., M. Gasulla, and V. Ferrari, *Thermal energy harvesting through pyroelectricity*. Sensors and Actuators A: Physical, 2010. **158**(1): p. 132-139.

168. Zheng, X.-C., et al., *Thermo-electrical energy conversions in Bi 0.5 Na 0.5 TiO 3–BaTiO 3 thin films prepared by sol–gel method*. Thin Solid Films, 2012. **522**: p. 125-128.

169. Huang, K., et al., *Significant polarization variation near room temperature of Ba 0.65 Sr 0.35 TiO 3 thin films for pyroelectric energy harvesting*. Sensors and Actuators B: Chemical, 2012. **169**: p. 208-212.

170. Morozovska, A., et al., *Pyroelectric response of ferroelectric nanowires: Size effect and electric energy harvesting*. Journal of Applied Physics, 2010. **108**(4): p. 042009.

171. Bowen, C., et al., *Pyroelectric materials and devices for energy harvesting applications*. Energy & Environmental Science, 2014. **7**(12): p. 3836-3856.

172. Bernal, R.A., et al., *Effect of growth orientation and diameter on the elasticity of GaN nanowires. A combined in situ TEM and atomistic modeling investigation*. Nano letters, 2010. **11**(2): p. 548-555.

173. Wang, Z.L., *Splendid one-dimensional nanostructures of zinc oxide: a new nanomaterial family for nanotechnology*. Acs Nano, 2008. **2**(10): p. 1987-1992.

174. Minary-Jolandan, M., et al., *Individual GaN nanowires exhibit strong piezoelectricity in 3D*. Nano letters, 2012. **12**(2): p. 970-976.

175. Minary-Jolandan, M., R.A. Bernal, and H.D. Espinosa, *Strong piezoelectricity in individual GaN nanowires*. MRS Communications, 2011. **1**(01): p. 45-48.

176. Persano, L., et al., *High performance piezoelectric devices based on aligned arrays of nanofibers of poly (vinylidenefluoride-co-trifluoroethylene)*. Nature communications, 2013. **4**: p. 1633.

177. Subbiah, T., et al., *Electrospinning of nanofibers*. Journal of Applied Polymer Science, 2005. **96**(2): p. 557-569.

178. He, F., et al., *Preparation and characterization of porous poly (vinylidene fluoride-trifluoroethylene) copolymer membranes via electrospinning and further hot pressing*. Polymer Testing, 2011. **30**(4): p. 436-441.

179. Kułek, J., C. Pawlaczyk, and E. Markiewicz, *Influence of poling and ageing on high-frequency dielectric and piezoelectric response of PVDF-type polymer foils*. Journal of electrostatics, 2002. **56**(2): p. 135-141.

180. Yang, Y., et al., *Single micro/nanowire pyroelectric nanogenerators as self-powered temperature sensors*. ACS nano, 2012. **6**(9): p. 8456-8461.

181. Hsiao, C.-C., A.-S. Siao, and J.-C. Ciou, *Improvement of pyroelectric cells for thermal energy harvesting*. Sensors, 2012. **12**(1): p. 534-548.

182. Hsiao, C.-C., et al., *Temperature field analysis for PZT pyroelectric cells for thermal energy harvesting*. Sensors, 2011. **11**(11): p. 10458-10473.

183. Hsiao, C.-C. and A.-S. Siao, *Improving pyroelectric energy harvesting using a sandblast etching technique*. Sensors, 2013. **13**(9): p. 12113-12131.

184. Wei, C., et al., *Partial-electroded ZnO pyroelectric sensors for responsivity improvement*. Sensors and Actuators A: Physical, 2006. **128**(1): p. 18-24.

185. Yang, Y., et al., *Flexible hybrid energy cell for simultaneously harvesting thermal, mechanical, and solar energies*. ACS nano, 2012. **7**(1): p. 785-790.

186. Lee, J.H., et al., *Highly stretchable piezoelectric-pyroelectric hybrid nanogenerator*. Advanced Materials, 2014. **26**(5): p. 765-769.

187. Erturun, U., et al. *Energy scavenging combining piezoelectric and pyroelectric effects*. in *ASME 2010 Conference on Smart Materials, Adaptive Structures and Intelligent Systems*. 2010. American Society of Mechanical Engineers.

188. Hunter, S.R. and P.G. Datskos, *MEMS based pyroelectric thermal energy harvester*. 2013, Google Patents.

189. Mostafa, S., et al. *A Finite Element Model of Self-Resonating Bimorph Microcantilever for Fast Temperature Cycling in A Pyroelectric Energy Harvester*. in *MRS Proceedings*. 2011. Cambridge Univ Press.

190. Cha, G. and Y.S. Ju, *Pyroelectric energy harvesting using liquid-based switchable thermal interfaces*. Sensors and Actuators A: Physical, 2013. **189**: p. 100-107.

191. Huesgen, T., et al., *Detailed study of a micro heat engine for thermal energy harvesting*. Journal of micromechanics and microengineering, 2010. **20**(10): p. 104004.

192. Ravindran, S., et al. *A self-sustaining pyroelectric energy harvester utilizing spatial thermal gradients*. in *Solid-State Sensors, Actuators and Microsystems Conference (TRANSDUCERS), 2011 16th International*. 2011. IEEE.

193. *Pyroelectric generator*. 1966, Google Patents.

194. Carlioz, L., J. Delamare, and S. Basrour. *Temperature threshold tuning of a thermal harvesting switch*. in *Solid-State Sensors, Actuators and Microsystems Conference, 2009. TRANSDUCERS 2009. International*. 2009. IEEE.

195. Kotipalli, V., et al., *Light and thermal energy cell based on carbon nanotube films*. Applied Physics Letters, 2010. **97**(12): p. 124102.

196. Zhang, Q., et al., *Solar micro-energy harvesting with pyroelectric effect and wind flow*. Sensors and Actuators A: Physical, 2011. **168**(2): p. 335-342.

197. Krishnan, S.H., et al., *Pyroelectric-based solar and wind energy harvesting system*. Sustainable Energy, IEEE Transactions on, 2014. **5**(1): p. 73-81.

198. Battista, L., et al., *Graphene and carbon black nano-composite polymer absorbers for a pyro-electric solar energy harvesting device based on LiNbO 3 crystals*. Applied Energy, 2014. **136**: p. 357-362.

199. Bhattacharjee, S., et al., *High-performance single and polycrystal-based pyroelectric smart materials for energy harvesting from pavements*. Transportation Research Record: Journal of the Transportation Research Board, 2011(2252): p. 75-82.

200. Guyomar, D., et al., *Toward energy harvesting using active materials and conversion improvement by nonlinear processing*. Ultrasonics, Ferroelectrics, and Frequency Control, IEEE Transactions on, 2005. **52**(4): p. 584-595.

201. Guyomar, D., et al., *Toward heat energy harvesting using pyroelectric material*. Journal of intelligent material systems and structures, 2008.

202. Goetz, J., *Sensors That Can Take the Heat, Part 1: Opening the High-Temperature Toolbox*. Sensors, 2000. **17**(6): p. 20-39.

203. Gregory, O.J. and T. You, *Ceramic temperature sensors for harsh environments*. Sensors Journal, IEEE, 2005. **5**(5): p. 833-838.

204. Lutz, S., et al., *Remote temperature-measurement instrumentation for a heated rotating turbine disk*. 1988, EG and G Energy Measurements, Inc., Goleta, CA (USA); Los Alamos National Lab., NM (USA); Oak Ridge Gaseous Diffusion Plant, TN (USA); Delco Electronics Corp., Goleta, CA (USA).

205. Taniguchi, T., et al. *Temperature Measurement of High Speed Rotating Turbine Blades Using a Pyrometer*. 2006. ASME.

206. Wasa, K., et al., *Highly-reliable temperature sensor using rf-sputtered SiC thin film*. Review of Scientific Instruments, 1979. **50**(9): p. 1084-1088.

207. Zappe, S., et al. *High temperature 10 bar pressure sensor based on 3C-SiC/SOI for turbine control applications*. in *Materials Science Forum*. 2001. Trans Tech Publ.

208. Scott, S. and D. Peroulis. *A capacitively-loaded MEMS slot element for wireless temperature sensing of up to 300 C*. in *Microwave Symposium Digest, 2009. MTT'09. IEEE MTT-S International*. 2009. IEEE.

209. Cai, W., et al., *Optical cloaking with metamaterials*. Nature photonics, 2007. **1**(4): p. 224-227.

210. Schurig, D., et al., *Metamaterial electromagnetic cloak at microwave frequencies*. Science, 2006. **314**(5801): p. 977-980.

211. Lee, S.H., et al., *Reversed Doppler effect in double negative metamaterials*. Physical Review B, 2010. **81**(24): p. 241102.

212. Arbabi, A., et al. *A terahertz plasmonic metamaterial structure for near-field sensing applications*. in *Infrared, Millimeter and Terahertz Waves, 2008. IRMMW-THz 2008. 33rd International Conference on*. 2008. IEEE.

213. Melik, R., et al., *Nested metamaterials for wireless strain sensing*. Selected Topics in Quantum Electronics, IEEE Journal of, 2010. **16**(2): p. 450-458.

214. He, X., et al., *Thin-film sensor based tip-shaped split ring resonator metamaterial for microwave application*. Microsystem technologies, 2010. **16**(10): p. 1735-1739.

215. Xia, Y. and L. Wang. *A wireless sensor using left-handed metamaterials*. in *Wireless Communications, Networking and Mobile Computing, 2008. WiCOM'08. 4th International Conference on*. 2008. IEEE.

216. Gu, J., et al., *A close-ring pair terahertz metamaterial resonating at normal incidence*. Opt. Express, 2009. **17**(22): p. 20307-20312.

217. Wu, M., et al. *A compact equivalent circuit model for the SRR structure in metamaterials*. in *Microwave Conference Proceedings, 2005. APMC 2005. Asia-Pacific Conference Proceedings*. 2005. IEEE.

218. Zhu, J., et al., *Optimal design of miniaturized thin-film helical resonators*. Applied physics letters, 2008. **93**(23): p. 234105-234105-3.

219. Lanfredi, S. and A. Rodrigues, *Impedance spectroscopy study of the electrical conductivity and dielectric constant of polycrystalline LiNbO3*. Journal of applied physics, 1999. **86**(4): p. 2215-2219.

220. Ekmekci, E. and G. Turhan-Sayan, *Comparative investigation of resonance characteristics and electrical size of the double-sided SRR, BC-SRR and conventional SRR type metamaterials for varying substrate parameters*. Progress In Electromagnetics Research B, 2009. **12**: p. 35-62.

221. Alici, K.B., et al., *Miniaturized negative permeability materials*. Applied physics letters, 2007. **91**(7): p. 071121-071121-3.

222. Kinoshita, K. and A. Yamaji, *Grain-size effects on dielectric properties in barium titanate ceramics*. Journal of Applied Physics, 1976. **47**(1): p. 371-373.

223. Pant, H.C., et al., *Study of the dielectric properties of barium titanate–polymer composites*. Acta materialia, 2006. **54**(12): p. 3163-3169.

224. Varadan, V.V., et al., *Free-space, broadband measurements of high-temperature, complex dielectric properties at microwave frequencies*. Instrumentation and Measurement, IEEE Transactions on, 1991. **40**(5): p. 842-846.

225. Sheen, J., et al., *Microwave measurements of dielectric constants by exponential and logarithmic mixture equations*. Progress In Electromagnetics Research, 2010. **100**: p. 13-26.

226. Sheen, J., et al., *Study of dielectric constants of binary composites at microwave frequency by mixture laws derived from three basic particle shapes*. European Polymer Journal, 2009. **45**(4): p. 1316-1321.

227. Niklasson, G.A., C. Granqvist, and O. Hunderi, *Effective medium models for the optical properties of inhomogeneous materials*. Applied Optics, 1981. **20**(1): p. 26-30.

228. Garnett, J.M., *205A, 237 (1906)*. Philos. Trans. R. Soc. London.

229. Bruggeman, D., *Dielectric constant and conductivity of mixtures of isotropic materials*. Ann Phys (Leipzig), 1935. **24**: p. 636-679.

230. Karim, H., *Development of'lick and stick'passive wireless temperature sensor for harsh environment*. 2013: THE UNIVERSITY OF TEXAS AT EL PASO.

231. Kaatze, U., *Complex permittivity of water as a function of frequency and temperature*. Journal of Chemical and Engineering Data, 1989. **34**(4): p. 371-374.

232. Karim, H., et al., *Concept and Model of a Metamaterial-Based Passive Wireless Temperature Sensor for Harsh Environment Applications*. Sensors Journal, IEEE, 2015. **15**(3): p. 1445-1452.

233. Kohvakka, M., M. Hännikäinen, and T.D. Hämäläinen. *Ultra low energy wireless temperature sensor network implementation*. in *Personal, Indoor and Mobile Radio Communications, 2005. PIMRC 2005. IEEE 16th International Symposium on*. 2005. IEEE.

234. Paradiso, J. and T. Starner, *Energy scavenging for mobile and wireless electronics*. Pervasive Computing, IEEE, 2005. **4**(1): p. 18-27.

235. Kim, H.S., J.-H. Kim, and J. Kim, *A review of piezoelectric energy harvesting based on vibration*. International Journal of precision engineering and manufacturing, 2011. **12**(6): p. 1129-1141.

236. Grätzel, M., *Solar energy conversion by dye-sensitized photovoltaic cells*. Inorganic chemistry, 2005. **44**(20): p. 6841-6851.

237. Chen, H.-Y., et al., *Polymer solar cells with enhanced open-circuit voltage and efficiency*. Nature Photonics, 2009. **3**(11): p. 649-653.

238. Buchanan, R.C. and J. Huang, *Pyroelectric and sensor properties of ferroelectric thin films for energy conversion*. Journal of the European Ceramic Society, 1999. **19**(6): p. 1467-1471.

239. Capineri, L., et al., *Comparisons between PZT and PVDF thick films technologies in the design of low-cost pyroelectric sensors*. Review of scientific instruments, 2004. **75**(11): p. 4906-4910.

240. Ferrari, V., et al. *Array of PZT pyroelectric thick-film sensors for contactless measurement of XY position*. in *Sensors, 2002. Proceedings of IEEE*. 2002. IEEE.

241. Bykhovski, A., et al., *Pyroelectricity in gallium nitride thin films*. Applied physics letters, 1996. **69**(21): p. 3254-3256.

242. Cooper, J., *A Fast Response Total-Radiation Detector*. 1962.

243. Padmanathan, N. and S. Selladurai, *Shape controlled synthesis of CeO2 nanostructures for high performance supercapacitor electrodes*. RSC Adv., 2014. **4**(13): p. 6527-6534.

244. Li, C., et al., *Controllable preparation and properties of composite materials based on ceria nanoparticles and carbon nanotubes*. Journal of Solid State Chemistry, 2008. **181**(10): p. 2620-2625.

245. Jian, L., et al., *Review of electrochemical capacitors based on carbon nanotubes and graphene*. Graphene, 2012. **2012**.

246. Bartasyte, A., et al., *Identification of LiNbO3, LiNb3O8 and Li3NbO4 phases in thin films synthesized with different deposition techniques by means of XRD and Raman spectroscopy*. Journal of Physics: Condensed Matter, 2013. **25**(20): p. 205901.

247. Srivastava, M., et al., *Characterizations of in situ grown ceria nanoparticles on reduced graphene oxide as a catalyst for the electrooxidation of hydrazine*. Journal of Materials Chemistry A, 2013. **1**(34): p. 9792-9801.

248. Harb, A., *Energy harvesting: State-of-the-art*. Renewable Energy, 2011. **36**(10): p. 2641-2654.

249. Bartholomäus, T., et al., *Pyroelectric coefficients of LiNbO3 crystals of different compositions*. physica status solidi (a), 1994. **142**(1): p. K55-K57.

250. Savage, A., *Pyroelectricity and spontaneous polarization in LiNbO3*. Journal of Applied Physics, 1966. **37**(8): p. 3071-3072.

# Curriculum Vita

Hasanul Karim was born on 1st February 1989 in Noakhali, Bangladesh. He is the second child of Mr. Ali Karim and Mrs. Mosammat Begum Noorjahan. Mr. Karim completed Bachelor of Science in Mechanical Engineering in April 2010 from Khulna University of Engineering & Technology. After completion of Bachelor degree, he joined the High Commission of Canada, Bangladesh and served as a facilities assistant. In August 2012 Mr. Karim joined the University of Texas at El Paso for his Master of Science degree in Mechanical Engineering. He graduated in December 2013 and continued towards his Ph.D. in mechanical engineering. During his doctoral study, he had 10 journal papers and 7 conference papers.

Contact Information:hkarim@miners.utep.edu

This thesis/dissertation was typed by Hasanul Karim.